Spectroscopic and Enzymatic Investigations into the Organometallic Incorporation of Methyl and Carbonyl Substrates by Acetyl-Coenzyme A Synthase from *Moorella thermoaceticum*

by

Seth Alexander Wiley

A dissertation submitted in partial fulfillment
of the requirements for the degree of
Doctor of Philosophy
(Chemical Biology)
in the University of Michigan
2020

Dissertation Committee

Professor Stephen W. Ragsdale, Chair
Professor Nicolai Lehnert
Professor Bruce Palfey
Professor Janet Smith

Seth A. Wiley

wileys@umich.edu

ORCID iD: 0000-0002-2447-5153

For those who have come before,

Bill B. Wiley, Ph.D.
(1923–2013)

Acknowledgements

The past five years have had an incalculably positive impact on my life and is first and foremost thanks to the incredibly supportive and independent environment present in the Ragsdale lab. I have found a true mentor in Prof. Stephen Ragsdale, who has encouraged and supported me throughout my graduate tenure. Prof. Ragsdale has promoted my investigative independence, furnishing me with his experienced perspective. Prof. Ragsdale served as my mentor, but the professional, intelligent, and conscious culture cultivated in his laboratory has molded me into a confident and independent researcher. The expertise and professionalism at the core of the Ragsdale lab were the major reasons for my decision to join, and it has been a privilege to learn from and work alongside those in the lab.

I would like to thank those in the past and present Ragsdale lab, Dr. Angela Fleischhacker, Dr. Mehmet Can, Dr. Anjali Patwardhan, Dr. Eric Carter, Dr. Johanna Mock, and Marco Hornung for the excellent and guidance I have received over my graduate career. I personally thank Dr. Katie Rush, my colleague, friend, climbing partner, D&D party member, political pundit, and mentor – you have added a myriad reasons to come in to work every day. I am incredibly fortunate to have had the chance to learn from Dr. Anindita Sarkar, Dr. Rodney Burton, Dr. Kaiyuan "Ken" Zheng. Liu "Judy/Lexi" Liu, I have been incredibly lucky to have had you as a benchmate – your insight in science, medical knowledge, cooking, baking, and most importantly, fashion, has seriously improved my day-to-day life. My friend Chris Ohmer – I wish we had more time to spend in lab together, although I am sure it might have been too much for the rest of the lab to handle. Claire Griffith, I am happy to hear somebody will be taking over for the ACS project, I know you will find it interesting. I thank the Ragsdale lab technician Dan Esckilsen for keeping everything running smoothly, I hope you are ready to take over the upkeep on the lab EPR! I would like to acknowledge Stephen Gonzalez, an REU visiting undergraduate, for his excellent scientific contributions in understanding ACS not included in this work.

As the nature of science is collaborative, I want to acknowledge and thank the collaborators whose contributions have significantly informed this work. I thank the off-campus collaborators

Dr. Ritimukta Sarangi at Stanford Synchrotron Radiation Lightsource (SSRL) of the Stanford Linear Accelerator Center (SLAC) National Accelerator Laboratory (Menlo Park, CA), Dr. Chris D. James and Prof. Brian Hoffman at Northwestern Univeristy (Evanston, IL), Dr. Jin Xiong and Prof. Yisong "Alex" Guo at Carnegie Mellon University (Pittsburgh, PA), and Alexander Mueller, Robert Nogle, Dr. Seán Simpson, and Dr. Michael Köpke at Lanzatech (Skokie, IL). I also thank our on-campus collaborators Dr. Peter A. Eckert and Prof. Kevin Kubarych here at the University of Michigan in Ann Arbor.

I would like to acknowledge the innumerable Michigan faculty that have positively impacted my graduate career. First and foremost, I want to acknowledge my dissertation committee, Prof. Janet Smith, Prof. Bruce Palfey, and Prof. Nicolai Lehnert for their constructive comments – I have learned immensely from your crucial feedback and expertise. I would personally like to thank the Program in Chemical Biology program chairs Prof. Anna Mapp and Prof. Zhaohui Xu for leading such an amazing graduate program that puts students above all. I want to thank Traci Swan, Laura Howe, and Dr. Adam Iliff for the amazing job they do as administrative staff and the wonderful guidance they offer, even if it is only a short fifteen-minute chat.

In addition to the aforementioned, I have had significant peer support in the Program in Chemical Biology, and from others on the University of Michigan campus. I want to acknowledge those who helped co-found and lead the graduate-student science policy group Engaging Scientists in Policy and Advocacy (ESPA) – Sara Wong, Charles Lu, Tejas Navaratna, and William Dean, along with our faculty sponsor, Dr. James "Jimmy" Brancho. I want to acknowledge the contributions of Dan Kremer, Pradeep Gunasekaran, and Jamie Do in co-founding the Graduate Assistance in Areas of National Need (GAANN) funded public outreach group Publications to the Public in 2017, as well as Monika Franco for her strong leadership in taking over after my leave – We had many late nights before our science presentations to public audiences at Cultivate.

Lastly, I want to acknowledge the friends and family who have supported me along the way. To my partner Madeline, who has always supported me throughout this endeavor, and had to put up with me in the final stretch – I *know* I could not have done this without your emotional, intellectual, and organizational support. You have always been in my corner from the very beginning. To my family – my mother and father who have provided the strong foundation I have used to build upon, my siblings who have always tested my scientific knowledge, and my

grandparents who have perpetually encouraged me. Finally, to my friends Dan Kremer, Dr. John “Jack” Crellin, Dr. James Annand, and Adrian Landreth – Ann Arbor has been amazingly fun with you all these past five years.

Table of Contents

List of Tables

List of Figures

List of Abbreviations

$^{13}CH_3I$ – ^{13}C-methyl iodide

$^{13}CD_3I$ – doubly-labeled MeI

2D-IR – two-dimensional infrared

[1-^{14}C]-acetyl-CoA – radiolabeled acetyl-CoA at the carbonyl moeity

[2-^{14}C]-acetyl-CoA – radiolabeled acetyl-CoA at the methyl moeity

$[Fe_4S_4]$ – four-iron, four-sulfur cluster

A-cluster – ACS metalloenzymatic active site

ACS – acetyl-coenzyme A synthase

Ala – alanine

A_{ox} – oxidized A-cluster

A_{red} – reduced A-cluster

A.U. – arbitrary units

C – carbon

C509 – cysteine 509

C528 – cysteine 528

C597 – cysteine 597

$CaCO_3$ – calcium carbonate

Cbi – cobinamide

Cbl – cobalamin

CD_3I – deuterated methyl iodide

Co – cobalt

CO – carbon monoxide

CO_2 – carbon dioxide

CODH – carbon monoxide dehydrogenase

CODH/ACS – carbon monoxide dehydrogenase/acetyl-coenzyme A synthase tetrameric complex

CoA – coenzyme A

CFeSP – corrinoid iron-sulfur protein

Cryo-EM – cryo-electron microscopy

Cu – copper

Cys – cysteine

DTT – dithiothreitol

e^- – single electron; one reducing equivalent

ENDOR – electron nuclear double resonance

EPR – electron paramagnetic resonance

F229 – phenylalanine 229

F229A – alanine substitution at F229

F229W – tryptophan substitution at F229

F512 – phenylalanine 512

Fd-II – ferredoxin

FDH – formate dehydrogenase

Fe – iron

FTIR – fourier transform infrared spectroscopy

G – gauss

G145 – glycine 145

H_2 – hydrogen gas

hv - light

I146 – isoleucine 146

ICP-OES – inductively coupled plasma optical emission spectroscopy

IR – infrared

K - kelvin

kDa – kilodalton

LC/MS/MS – linear chromatography mass spectrometry mass spectrometry

M-CO – generalized metal-carbonyl

Me – methyl

Me-ACS – methylated ACS

MeCbi – methyl-cobinamide

MeCbl – methyl-cobalamin

Me-CFeSP – methylated corrinoid iron-sulfur protein

MeI – methyl iodide

MeTr – methyl transferase

M_p – generalized proximal metal in A-cluster

MS – mass spectrometry

mV – millivolt

mW – milliwatts

NA – natural abundance

Ni – nickel

Ni-C – nickel-carbon bond

Ni-CO – nickel-carbonyl

Ni_d – distal nickel

NiFeC – nickel-iron-carbonyl signal observed by EPR

Ni_p – proximal nickel

Ni_p-Me – methylated proximal nickel

Phe – phenylalanine

RFQ – rapid freeze quench

SDS-PAGE – sodium dodecyl sulfate polyacrylamide gel electrophoresis

TEV – tobacco etch virus

THF – tetrahydrofolate; H_4-folate

Ti – titanium

Trp – tryptophan

V – volt

V149 – valine 149

WLP – Wood-Ljundahl pathway

WT – wildtype

XAS – x-ray absorption spectroscopy

Xe – xenon

Zn – zinc

Abstract

The Wood-Ljungdahl pathway of acetogenesis is an ancient metabolic pathway found in both bacteria and archaea that allows for the reversible reduction and fixation of CO_2 into bioavailable carbon. Within this pathway, two nickel- and iron-containing enzymes, carbon monoxide dehydrogenase (CODH) and acetyl-CoA synthase (ACS), form a tight enzymatic complex and are responsible for the direct fixation of CO_2 into acetyl-CoA. CODH reduces CO_2 to CO, tunnels the CO through an interprotein channel to the ACS dinickel iron-sulfur cluster active site known as the A-cluster, where the CO is condensed with a methyl group donated by partner protein CFeSP forming an acetyl group transferred to CoA to form acetyl-CoA. The ACS mechanism is random, binding either the CO or methyl substrate first to an A-cluster nickel ion, and once both substrates (CO and methyl) are bound, a carbonyl insertion or alkyl migration occurs yielding a hypothetical nickel-acetyl before forming the C-S bond in acetyl-CoA. Crystallographic studies of CODH/ACS under high xenon gas pressure have revealed a hydrophobic CO alcove at the end of the CO channel near the A-cluster, with spectroscopic evidence supporting the alcove's crucial role in CO binding. This dissertation was aimed at characterizing the properties of the methylated ACS, and the role of the hydrophobic alcove near the A-cluster.

Previous EPR and infrared spectroscopy experiments have provided evidence for an organometallic Ni-CO bond in the carbonylated state of ACS, but less is known about the methylated state of ACS. Chapter 2 describes the spectroscopic and kinetic characterization of the methylated state of ACS, showing methyl transfer occurs by an S_N2 nucleophilic displacement mechanism implying formation of a methyl-Ni(III) product, however, no paramagnetic A-cluster is present after methylation. EPR, ENDOR, and Mössbauer experiments with isotopically labeled ACS and methyl-cobinamide support the diamagnetic state of the methylated A-cluster, suggesting a transient paramagnetic methyl-Ni(III) product is in rapid equilibrium with a diamagnetic methyl-Ni(II) species. Chapter 3 describes studies of the carbonylated state of ACS, revealing the requirement for the alcove in CO binding. These studies strongly indicate the second coordination sphere residue F229, located in the CO alcove near the A-cluster, is necessary for forming the NiFeC EPR signal, the signature of the Ni(I)-CO intermediate in ACS. In the F229A substitution,

the ACS NiFeC is severely altered, shifting the characteristic *g*-values from 2.08, 2.07, and 2.03 in the wildtype to 2.06, 2.04, and 2.02 in F229A with significantly diminished EPR intensity, yielding ~20% of the overall signal seen in the wildtype. Not only does the F229A substitution affect EPR, *in vivo* experiments corroborate the requirement for a complete alcove in fixing CO_2 by the Wood-Ljungdahl pathway.

The studies described in this work suggest a rapid redistribution of delocalized electrons within the A-cluster after methylation leading to the rapid decay of a paramagnetic methylated A-cluster. This work also highlights the importance of second coordination sphere effects provided by the alcove in facilitating CO-binding at the A-cluster. These conclusions significantly improve the understanding of the A-cluster structure and function in ACS and provide critical insight into the organometallic mechanism of anaerobic carbon fixation. Altogether, understanding the complex bioinorganic chemistry accomplished by ACS provides integral details in facilitating the reversible reaction of anaerobic carbon fixation, offering the enticing possibility of renewable carbon-based fuel by improving the efficiency of this alternative pathway.

Chapter 1
Introduction to Reductive CO and CO_2 Fixation in Acetogens using the Wood-Ljungdahl Pathway

1.1 Global Carbon Cycle & Anaerobic CO_2 Fixation by the Wood-Ljungdahl Pathway

One of the largest threats facing humanity in the coming century is the increasing global concentration of carbon dioxide in the atmosphere, affecting wide-reaching aspects such as rising sea levels, ocean acidification, and more severe weather[1,2]. There is a need to understand the mechanism of CO_2 fixation and how it can be applied to produce small-chain industrial chemicals in cost-effective and environmentally-friendly ways. Due to the intense energy requirement in activating CO_2, there are very few industrial processes that utilize CO_2 as a starting material for biofuel production, EcoCement, and $CaCO_3$. While there are industrial uses for small carbon compounds, such as CO and methanol in the Monsanto process[3], turning to nature offers the potential of engineering greener and more renewable pathways to directly convert CO_2 into useful chemical products. In efforts to produce greener and more renewable methods to reduce atmospheric CO_2 levels and produce useful biofuels and chemicals, some companies have used plants, algae, and both aerobic and anaerobic microbes. One such company, Lanzatech (Skokie, IL) has been using its own proprietary strains of anaerobic microbes to recycle industrial waste gases from petroleum refining and biomass-generated syngas (CO, H_2, and CO_2) to for production of fuel and other chemical feedstocks for industrial use[4].

A number of diverse pathways are used by organisms to fix and metabolize carbon, and of these pathways, the reductive acetyl-coenzyme A pathway, also known as the Wood-Ljungdahl Pathway (WLP) of acetogenesis, is of particular interest due to the utility in producing simple, small chain organic chemicals and in addressing rising atmospheric carbon dioxide levels. The WLP is bidirectional, capable of reductive acetogenesis for autotrophic carbon incorporation and energy storage, as well as oxidative acetolysis for generating carbon for the cell as well as ATP[5]. The WLP is an ancient pathway phylogenetically dispersed in strictly anaerobic acetogenic bacteria and methanogenic archaea, such as *Moorella thermoaceticum*, *Carboxydothermus*

hydrogenoformans, and *Methanosarcina acetovorans*, which have evolved to live in ancient anaerobic environments and had been estimated to be responsible for 10 billion tons of acetate produced in the US in 1994[5-7]. This pathway was present in the last universal common ancestor of all living organisms and has been proposed to have fueled the origin of life[6,8]. While distinct in their own right, both methanogenic and acetogenic microbes share incredible similarity in their usage of the WLP, both using their own versions of the pathway in order to reduce and incorporate CO_2 into acetyl-coenzyme A (CoA) and their own particular metabolites to suit their needs[5,9].

1.2 Enzymes Within the Wood-Ljungdahl Pathway of Acetogenesis

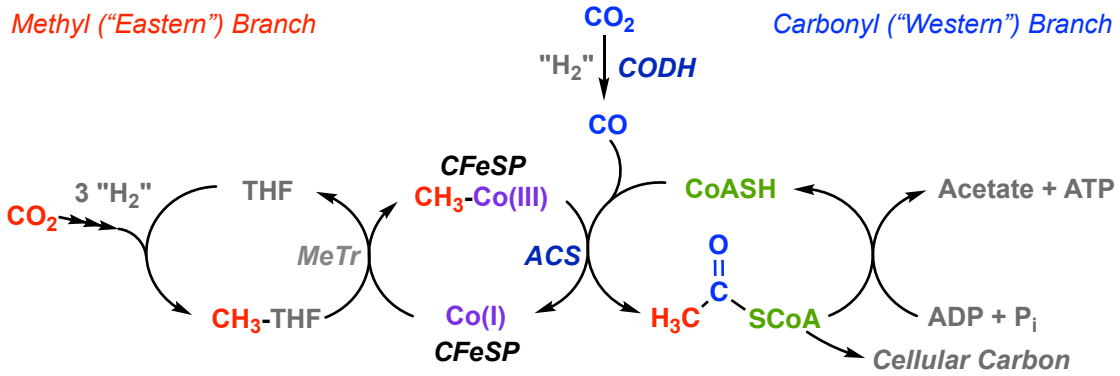

Figure 1.1 ACS – Where East meets West in the Wood-Ljungdahl Pathway of acetogenesis. CO_2 enters the pathway at two points, the Eastern (Methyl) branch showing the conversion of CO_2 to methyl in red, and the Western (Carbonyl) branch where CO_2 is reduced to CO and incorporated to acetyl-CoA at the ACS active site. Adapted from Can, 2014[10].

The enzymes within the WLP were fully identified from 1980 to 1985 by Harland Wood and Lars Ljungdahl and perform a number of anaerobic and inorganic chemical reactions using unique metalloenzymatic chemistry[5]. Figure 1 shows the key WLP enzymes responsible for conversion of and fixation of CO_2 into cellular carbon. The methyl branch begins with formate dehydrogenase (FDH), converting CO_2 into formyl-tetrahydrofolate, where it is successively reduced to methyl-tetrahydrofolate by formyl-tetrahydrofolate synthase and methylene-tetrahydrofolate dehydrogenase/cyclohydrolase, and is ultimately transferred from methyl-tetrahydrofolate to the Corrinoid Iron-Sulfur Protein (CFeSP) by methyltransferase (MeTr), producing methyl-CFeSP[10,11].

Of the carbonyl branch enzymes within the WLP, the reduction and incorporation of carbon dioxide into acetyl-CoA is carried out by the linchpin enzyme pair carbon monoxide dehydrogenase/acetyl-CoA synthase (CODH/ACS) and is the point at which the two branches meet, with the methyl-group donated by methyl-CFeSP. The tight CODH/ACS complex is a 310 kDa, $\alpha_2\beta_2$ heterotetrameric enzyme pair with both CODH β subunits centralized and flanked by the ACS α subunits[12-14]. CODH/ACS contains 4 unique iron-sulfur clusters throughout the complex, one of which is shared and two of which are nickel-containing metal clusters: the C-cluster in CODH and the A-cluster in ACS (Figure 1.2)[12,15,16]. The CODH/ACS complex first catalyzes the -558 mV reduction of CO_2 to CO at the CODH C-cluster, transports the CO roughly 70 Å through the 130 Å long interprotein CO channel, where the CO is condensed to an acetyl group at the ACS A-cluster with the methyl cation donated from CFeSP, and ultimately transferred to CoA to form the acetyl-CoA product where it can be used as needed within the cell[10,14,17-19]. Genomic profiling of the WLP has shown CODH and ACS are respectively encoded in the *acsA* and *acsB* genes in bacteria as part of a gene cluster that encodes all enzymes (CODH, ACS, MeTr, CFeSP) in the carbonyl branch of the WLP[5,6,11].

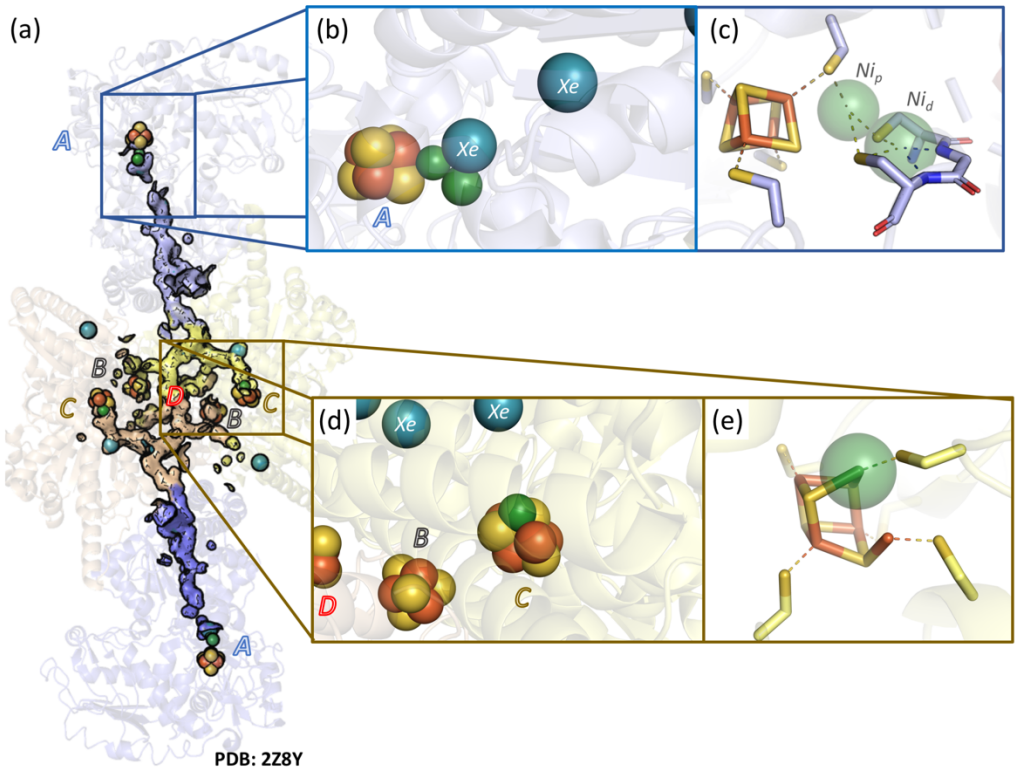

Figure 1.2 The CO Channel and nickel-containing A- and C-clusters in CODH/ACS. (a) High pressure Xe crystal structure of CODH/ACS, showing the 130 Å-long CO channel spanning the heterotetrameric complex. A-, B-, C-, and D- clusters are labeled at their respective locations. CO_2 is reduced at the CODH C-cluster, moves 70 Å to the ACS A-cluster where it is condensed into acetyl-CoA. (b) The ACS A-cluster in relation to the Xe-filled CO channel. (c) Stick representation of the A-cluster architecture, with Ni_p and Ni_d. (d) CODH C-cluster in relation to Xe-filled CO channel. (e) Stick representation of the C-cluster architecture. CODH in yellow/orange, and ACS in blue/light blue. PDB: 2Z8Y.

1.3 The CO Channel Spanning CODH/ACS

Biochemical evidence for the 130 Å hydrophobic CO-shuttling channel spanning the CODH and ACS active sites was observed as early as 1999 when labeled CO_2 was shown to be incorporated into acetyl-CoA and with no reduction in label incorporation when the solution contained unlabeled CO or CO-sponging myoglobin[19,20]. Considering the lack of CO influence on formation of acetyl-CoA, the role of the CO channel has been hypothesized to prevent the required substrate CO from leaking out into the cell during conversion of CO_2 into cellular carbon[19]. Crystallographic data confirmed this CO channel is 70 Å and connects the active site C-cluster in CODH to the A cluster in ACS[12-14,21]. Blocking this CO channel prevents proper funneling of CO from the A-cluster to the C-cluster, leaving the complex unable to oxidize CO to CO_2, and indicates

CO is funneled strictly through this channel[18]. Additional crystallographic studies with ACS crystallized under high-pressure xenon mimicking a CO-filled ACS showed xenon atoms throughout the ~130 Å channel, and unexpectedly showed a xenon atom cradled in close proximity to the A-cluster, within a structure proposed to act as a CO alcove proximal to the A-cluster[14].

1.4 ACS as the Linchpin Enzyme in Acetyl Group Condensation

Some of the earliest studies of the CODH/ACS complex did not recognize ACS as a separate enzyme, understandably referring to the heterotetrameric complex solely as CODH, and the two enzymes were not fully labeled as separate until the early 1990s[22,23]. Once ACS was separated from CODH, the function of ACS itself could begin to be understood in its own right as an important catalyst in carbon fixation.

1.4.1 Architecture & Composition of the A-cluster

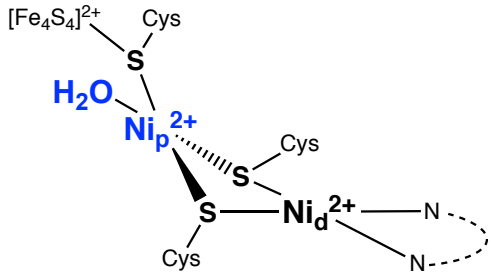

Figure 1.3 ACS A-cluster architecture. Two nickel nuclei occupy metal sites in the proximal (Ni_p) and distal (Ni_d) sites near the [Fe_4S_4] cluster.

The unique ACS A-cluster was determined in complementation with crystallographic data roughly ten to fifteen years ago to contain an [Fe_4S_4]-Ni_p-Ni_d architecture (Figure 1.3)[13,14]. Both mononuclear nickels labeled by their proximity to the [Fe_4S_4] cluster and in which the proximal nickel (Ni_p) is coordinated by 3 cysteine thiolates in a μ^2-bridging fashion, whereas the distal nickel (Ni_d), is coordinated by two μ^2-bridging cysteine thiolates and two glycine amide backbone nitrogen ligands (Figure 1.4)[24].

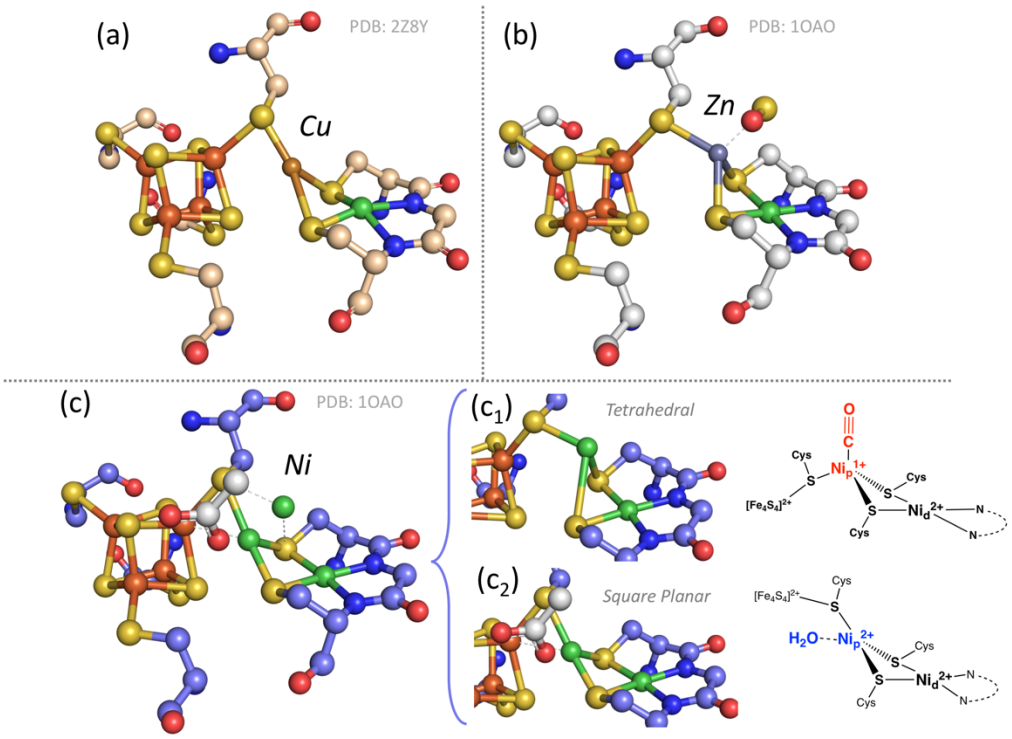

Figure 1.4 Various divalent metals observed occupying the proximal metal site in the ACS A-cluster. While nickel is considered occupy the distal site, (a) copper, (b) zinc, and (c) nickel have all been observed in the proximal metal (M_p) site. (c) Nickel was found to be the pertinent A-cluster M_p and is observed in both tetrahedral (c_1) and square planar (c_2) geometries. Relevant geometry is shown by schematic representations in (c_1) and (c_2).

The Ni_p is labile, easy to reconstitute, and replaceable with other divalent metals, and throughout the 2000s, a lot of ACS discussion was focused on the true metal composition at the A-cluster active site[25-27]. Crystallographic studies showed various divalent transition metals, such as copper, nickel, and zinc, occupying the proximal metal-binding site (M_p) (Figure 1.4), with the square-planar distal metal site near-ubiquitously occupied by a redox-inert (e.g., only 2+) square planar nickel, now referred to as Ni_d[13,14,28]. While zinc can be found as the central catalytic metal in various enzymes throughout biology, it is not able to participate in the redox chemistry necessary for M_p due to its fully occupied d-orbitals and the impact zinc on ACS activity has identified it to be an inactive contaminant metal[16,29-32]. Both copper and nickel were considered at one time to have potential to engage in catalysis at M_p and was a point of contention in elucidating the proper A-cluster composition, before the A-cluster was proven to correlate activity to nickel loading, and was ultimately deemed to have nickel in both the proximal (Ni_p) and distal sites (Ni_d)[15,30,33].

Structural data suggests the ability of Ni_p to access multiple redox states and both square planar and tetrahedral geometries as the primary catalytic metal, in contrast to the Ni_d[13,34]

1.4.2 The ACS Mechanism of Acetyl-CoA Production

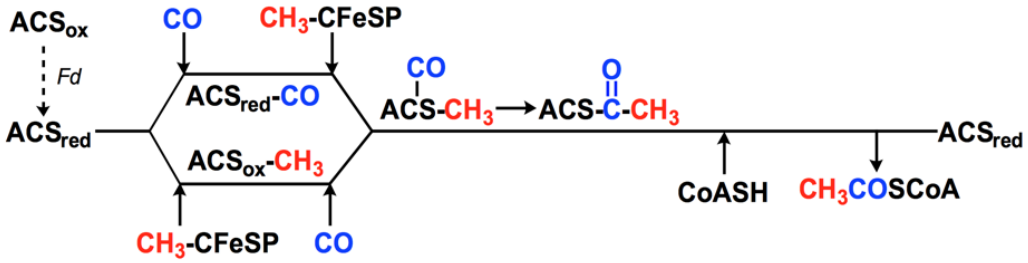

Figure 1.5 Random Mechanism of ACS. CO is provided by CODH through the CO channel in Figure 1.2, (a). Methyl group is donated by partner Corrinoid Iron-Sulfur Protein (CFeSP). Substrates rearrange at nickel site proximal to [Fe_4S_4] to form an acetyl group, which is transferred to CoA, forming acetyl-CoA. Adapted from Can, 2017[34].

The ACS mechanism (Figure 1.5) is random, where once ACS is reduced by an external redox mediator, such as the native ferredoxin (Fd-II), either of the CO or methyl substrates can bind first to the Ni_p in the A-cluster[35,36]. After the first substrate binds, the second substrate is hypothesized to bind to the A-cluster, where the CO and methyl group are condensed into the acetyl group on the Ni_p. ACS then facilitates a carbon-sulfur bond formation by acetyl group transfer to coenzyme A (CoA), where acetyl-CoA leaves and the catalytic cycle can be restarted. The reversibility of the mechanism allows for ACS to both produce and consume acetyl-CoA for energy within the organism and thus ACS must be able to both condense and fragment the acetyl group[4,5,37]. This mechanistic reversibility was biochemically proven by demonstrating the radiolabeled carbonyl group of acetyl-CoA ([1-^{14}C]-acetyl-CoA) undergoes exchange with unlabeled CO, present in the assay solution, revealed by loss of the radiolabeled acetyl-CoA accompanied by recovery of the label in CO[38].

While CO-binding to the A-cluster occurs through an intramolecular CO channel, ACS must open and close to accommodate methylation by its partner, CFeSP[39-41]. Crystallographic data from the CODH/ACS complex has indicated a static CODH and a conformationally flexible ACS that accesses both an open and a closed conformation[13]. The conformational changes in ACS are believed to allow for CFeSP to directly access and transfer the methyl group to the Ni_p of the A-

cluster, while simultaneously ceasing CO channel access to the Ni_p[13]. More recently, ACS has been shown through CODH/ACS Cryo-EM experiments to open and close to a much greater extent, opening significantly further than previous x-ray data had suggested (Cohen *et al.*, in revision)[12-14].

1.5 Insights into the ACS Mechanism

Significant insight has been obtained about ACS by numerous spectroscopic and kinetic techniques, including electron paramagnetic resonance (EPR), Mössbauer, electron nuclear double resonance (ENDOR), infrared (IR), inductively-coupled plasma optical emission spectroscopy (ICP-OES), UV-Visible, and X-ray absorption spectroscopy (XAS), as well as transient and steady-state kinetic assays mentioned below and described in a review[10].

1.5.1 The Reduced ACS (A_{red}) State

The reduced state of ACS is a necessary step in all subsequent chemistry, whether in binding substrates or facilitating the reverse reaction[36]. The CODH/ACS complex is not only capable of autoreduction in the presence of CO, where A-cluster reduction is coupled to CO oxidation by CODH, but ACS is also capable of being reduced by its native external redox activator ferredoxin-II (Fd-II)[25,36,42-44]. EPR data has consistently indicated an EPR-silent state for the as-isolated $[Fe_4S_4]$(II)-Ni_p(II)-Ni_d(II) A-cluster in ACS, and reduction provides no EPR-active Ni_p(I), even with low-potential electron donors, such as titanium(III) citrate, sodium dithionite, or Fd-II[36,45] (Figure 1.6). In 2006, Mössbauer and EPR evidence indicated an $[Fe_4S_4]$(I) signal in the presence of low-potential reductants, but with more recent XAS experiments between as-isolated and reduced ACS, the Mössbauer and EPR results likely reflect the inactive, Ni_p-absent enzyme[34,46].

The state of the reduced A-cluster appears to be a paramagnetic Ni(I) state; however, this assignment is complicated because the addition of reductants alone is not sufficient to trap an EPR-active A-cluster[34]. Generation of this reduced state apparently requires chemical coupling to the respective CO and methyl substrates to observe redox changes relative to the oxidized A-cluster. We interpret these results to indicate that the A-cluster is poised for electrochemically-coupled substrate binding, an effectively "unreduced" $[Fe_4S_4]$(II)-Ni_p(II)-Ni_d(II), until contact with the carbonyl or methyl substrates[34] to generate a methyl-Ni(III) or a Ni(I)-CO intermediate. Other

proposed scenarios for the "reduced" A-cluster are a $Ni_p(0)$ state upon reduction, or an antiferromagnetic delocalized-electron coupled system, where ACS has a 2-electron reduced A-cluster $[Fe_4S_4](I)$-$Ni_p(I)$-$Ni_d(II)$ and thusly remain EPR-silent[28,34,46]. One existing hypothesis is the reduced state may be in equilibrium between a transient reduced species and a more stable EPR-silent oxidized state and could explain the lack of any observed paramagnetic signal for the reduced A-cluster without substrate present.

1.5.2 State of the CO-Bound ACS

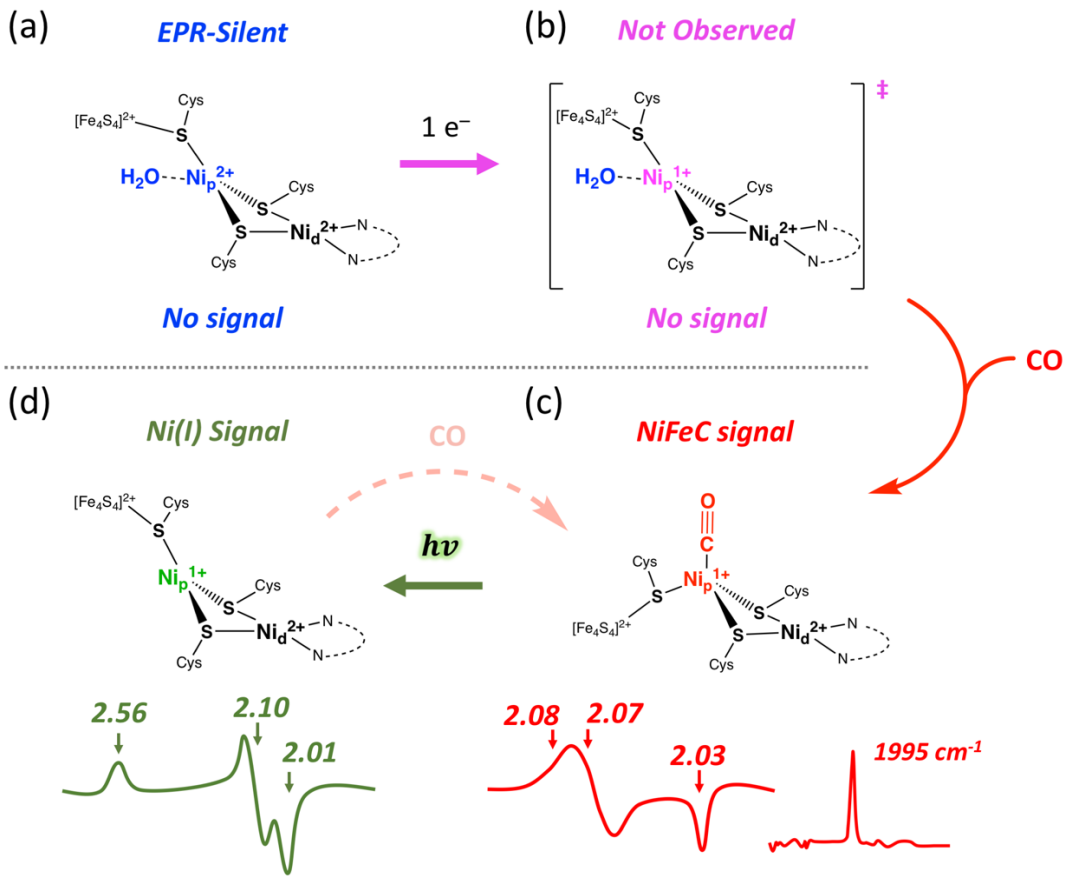

Figure 1.6 Characteristic FTIR and EPR signals associated with ACS A-cluster Carbonylation. Beginning clockwise from (a), the resting state of ACS is spectroscopically silent and (b) remains silent even when reduced by low potential reductants. (c) Once the reduced ACS is exposed to CO, it forms characteristic IR and EPR signals indicative of a Ni-CO bond seen around 1995 cm^{-1} in FTIR (*Bottom Right*), and at *g*-values of 2.08, 2.07, and 2.03 in EPR (*Bottom Middle*). Photolysis of (c) produces the very distinct and short-lived (d) Ni(I) EPR signal with *g*-values of 2.56, 2.10, and 2.01 (*Bottom Left*). The Ni(I) signal is only seen for minutes at temperatures below 40K, rapidly recombining with CO to reproduce (c).

Early EPR investigations on the CODH/ACS complex revealed a nearly axial rhombic spectrum with *g*-values of 2.08, 2.07, and 2.03 (Figure 1.6) shown to be the low-spin $S = 1/2$, CO-exposed ACS A-cluster, established as the NiFeC signal through isotopic dependence on ^{61}Ni ($I = 3/2$), ^{57}Fe ($I = 1/2$), and ^{13}CO ($I = 1/2$)[22,47-51]. This NiFeC signal correlated with the activity and metal content of ACS and is routinely used as an activity marker in the protein in assessing the catalytic activity ACS when quantified with a 1 mM Cu(II) perchlorate standard[26,52].

Fourier Transform Infrared (FTIR) experiments have also indicated the existence of a CO-bound A-cluster with the emergence of a terminal M-CO bond at a CO stretching frequency of 1995 cm^{-1} for the carbonylated ACS[53,54]. Stopped Flow-Fourier Transform Infrared (SF-FTIR) experiments revealed rapid formation of the characteristic M-CO at 1995 cm^{-1}, binding CO to saturation at 1995 cm^{-1} within 3 seconds, with NiFeC validation by rapid freeze-quench (RFQ) EPR[55]. Using the NiFeC EPR signal as a marker, RFQ-EPR experiments have indicated Ni-CO is a productive intermediate within the ACS mechanism, showing the NiFeC signal disappearing within 10 seconds upon methylation by Me-CFesP[55,56]. The FTIR results along with crystallographic, EPR, and Mössbauer data suggest the CO-bound A-cluster is composed of a terminally CO-bound Ni_p and is unlikely to bind directly to the $[Fe_4S_4]$ or Ni_d[14,55-57].

CO has been identified as a productive and catalytically-relevant intermediate within the ACS mechanism[55]. Seravalli in 2007 showed that there is no preferential order for methyl or carbonyl substrate binding through pulse-chase studies for the CODH/ACS complex and that CoA is the last to bind to ACS[35,56]. For the monofunctional ACS, CO was trapped into acetyl-CoA with slightly less fidelity (60-70% isotopic retention) than with the methyl-CFeSP substrate (~100% isotopic retention) during the pulse-chase experiments[35].

The CO-bound A-cluster has certainly proven to be a productive intermediate in the ACS mechanism, but CO titration studies have indicated slight inhibition in concentrations of CO above 100 μM[55,56,58,59]. The inhibition seen at higher CO concentrations has been hypothesized to stem from an A-cluster with two COs bound rather than one, but infrared experiments have yet to observe two distinct COs bound to the A-cluster[55,56,58]. On the other hand, recent ENDOR experiments indicate the presence of two CO molecules bound to the active NiFeC species[60].

More recent CO-binding studies have focused on the direct structural effects the substrates have on the A-cluster. Exposing the CO-bound A-cluster to intense light causes photolysis of the Ni-CO bond, yielding a clean Ni(I) EPR signal without coupling to the $[Fe_4S_4]$ cluster, strongly

indicating CO binds exclusively to the labile Ni_p (Figure 1.6)[45]. Recent XAS experiments revealed geometric and environmental changes to the A-cluster upon CO exposure, revealing a pre-edge shift from a square-planar to a tetrahedral geometry corresponding to only one of the two nickel atoms[34]. The pre-edge changes associated with the Ni K-edge are hypothesized to reflect only the Ni_p, as previous crystallographic evidence indicates the labile Ni_p has significantly more geometric flexibility to accommodate the shifts seen in XAS[13,21,34].

1.5.3 State of the Methylated ACS

The other substrate critical to acetyl-CoA production by ACS is the methyl group donated by its partner protein, CFeSP[5,10]. The methylation reaction between ACS and CFeSP is hypothesized to be a 2-electron nucleophilic methyl transfer, where the reduced A-cluster in ACS accepts a methyl cation from CFeSP (Figure 1.7), simultaneously oxidizing the A-cluster and reducing the CFeSP by 2 electrons[58,61]. The methylation of ACS is indirectly observable via UV-Visible spectroscopy, following the decrease in methyl-Co(III)FeSP to Co(I)FeSP, and requires a low-potential reductant to proceed, suggesting a "reduced" ACS is necessary for an S_N2 nucleophilic methyl transfer between metallocenters[58,61].

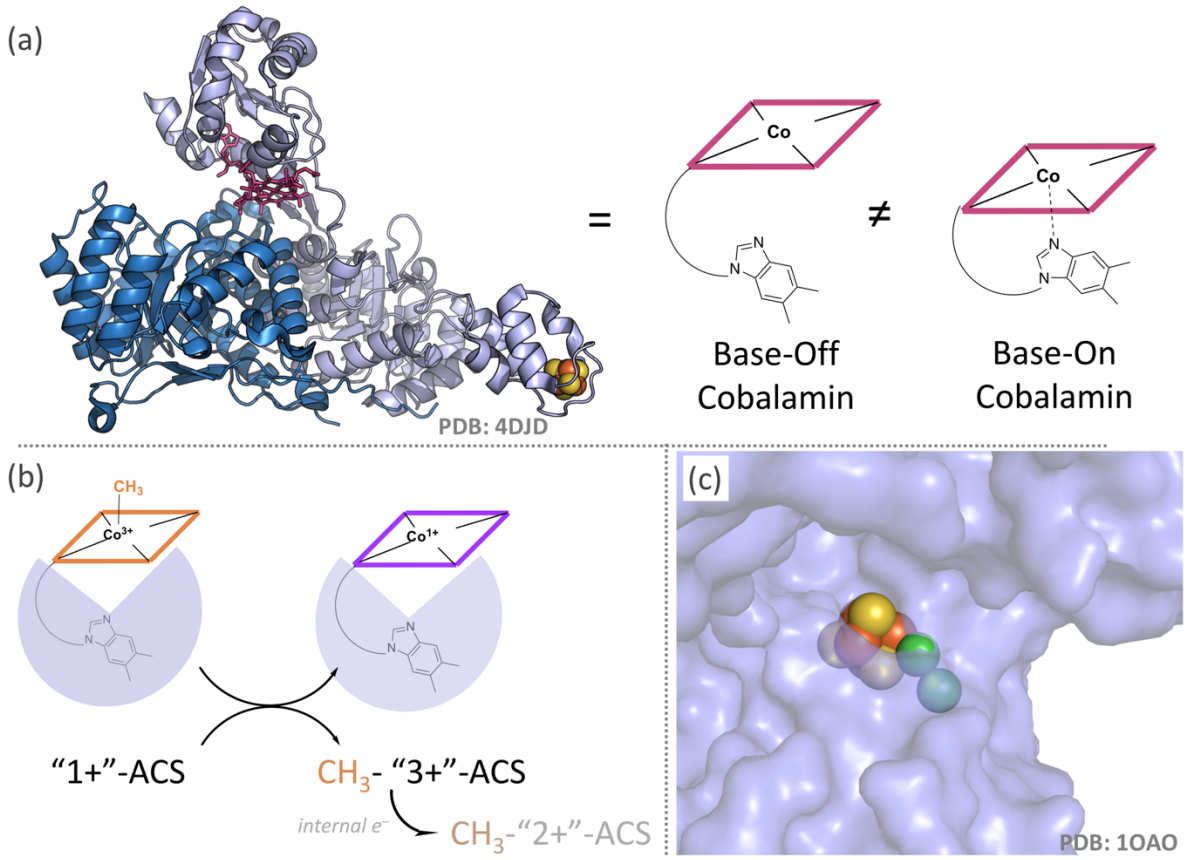

Figure 1.7 Corrinoid Iron Sulfur Protein (CFeSP) as the ACS methyl donor. (a) CFeSP's cobalamin cofactor binds in a base-off fashion. (b) Methylation between CFeSP and ACS is nucleophilic, oxidizing ACS and reducing CFeSP's cobalamin cofactor by 2 e^-. (c) Model depicting the open state of ACS, primed for methylation of the A-cluster.

ACS is also able to methylate with other corrinoid methyl donors such as methyl-cobalamin and methyl-cobinamide, albeit at considerably lower rates[62]. CFeSP binds its cobalamin cofactor in a "base-off" fashion where the axial dimethylbenzimidazole ring is not bound to the corrin ring, lacking an axial coordinating residue[39,62] (Figure 1.7; (a)). Due to the lack of an axial coordinating ligand, cobinamide has the ability to act as a slower methyl donor for CFeSP[62]. Steady-state production of acetyl-CoA by ACS with the aforementioned methyl donors CFeSP, cobalamin, and cobinamide has shown that ACS is most rapidly methylated by CFeSP at 20,000 $M^{-1}s^{-1}$, followed by cobinamide at 200 $M^{-1}s^{-1}$, and lastly by cobalamin at 0.12 $M^{-1}s^{-1}$[62]. The methylation equilibrium between ACS and CFeSP is $K_{eq} \sim 2.3$, implying the nucleophilicity of a $Ni_p(I)$ is greater than Co(I)-FeSP and suggests the intermediate role of a methyl-nickel is very likely to exist during the methyl-transfer reaction[28,58].

The state of the methylated A-cluster has been more spectroscopically elusive than the carbonylated A-cluster, with no direct evidence showing the putative methyl-nickel bond or associated changes observed to date. As proteins consist heavily of C-H bonds and the 300-500 cm^{-1} region has overlapping infrared bands, infrared spectroscopy provides no adequate resolution for such small changes in methylation in contrast to those seen for a M-CO[63]. EPR spectroscopy has also provided no insight into the methylated CODH/ACS, as no hypothesized EPR-active Ni(III) has been observed for the methylated A-cluster[51,56,64]. Mössbauer data for the methylated and acetylated ACS has shown the $[Fe_4S_4]$ cluster appears identical to that in the as-isolated A-cluster, remaining in the $[Fe_4S_4]$(II) state, implying that the $[Fe_4S_4]$ cluster does not change upon methylation[46]. With no evidence of an EPR-active A-cluster after methylation by CFeSP and crystallographic evidence showing the conformationally flexible open- and closed-states of ACS, the A-cluster is hypothesized to bind a methyl-Ni_p(II) in a square planar geometry, with the A-cluster becoming solvent exposed upon opening (Figure 1.7; (c)).

1.6 The True ACS Mechanism – A Controversial Debate

There has been great debate about the exact nature of the ACS mechanism ever since the observation of the NiFeC, and how this signal is associated to the formation of acetyl-CoA[10,28]. Two distinct hypotheses have arisen to explain the observed spectroscopic phenomena of the ACS mechanism, and while similar, the two hypotheses differ on the redox state of Ni_p in the A-cluster (Figure 1.8)[10,28]. The hypothesis put forward by Ragsdale favoring a reduced "Ni_p(I)" and catalytically competent Ni_p(I)-CO is referred to as the paramagnetic mechanism, whereas the hypothesis asserted by Lindahl favoring an EPR-silent Ni_p(0) reduced A-cluster is referred to as the diamagnetic mechanism[10,28]. Both of the two potential mechanisms have numerous similarities; a redox-inactive Ni_d(II), the nucleophilic S_N2 reaction after A-cluster activation, and both account for the observation of the EPR-active Ni_p(I)-CO NiFeC signal[10,28].

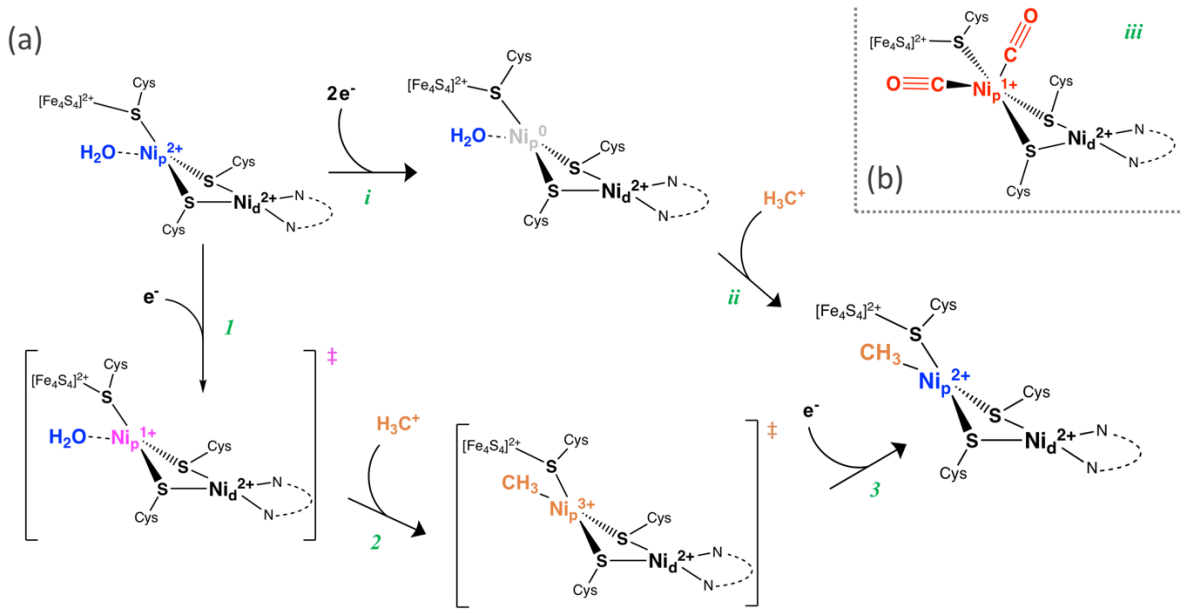

Figure 1.8 Diamagnetic and paramagnetic ACS mechanisms. (a) The main differences between the diamagnetic (*i-iii*) and paramagnetic (*1-3*) mechanisms, with both beginning at the resting state (*top left*). The diamagnetic mechanism (*top*) begins with a (*i*) 2 electron reduction of the resting state to Ni(0). The Ni(0) state then undergoes a (III) nucleophilic methylation by CFeSP to produce the diamagnetic methyl-Ni(III) state. (b) In the diamagnetic mechanism, the NiFeC is proposed to be a non-catalytic inhibited state consisting 2 bound COs. The paramagnetic mechanism (*bottom*) begins with a (*1*) single electron reduction which is able to undergo (*2*) nucleophilic methylation by CFeSP. The highly oxidizing methyl-Ni(III) is (*3*) reduced by an electron from an unknown source to produce the diamagnetic methyl-Ni(III) state.

The diamagnetic mechanism offers an explanation for the EPR-silence observed with both the "reduced" and methylated A-cluster[28]. The initial 2-electron reduction of Ni_p(II) to Ni_p(0), and subsequent methylation of Ni_p(0) to Ni_p(II) offers an explanation why no EPR signals are associated with changes in the ACS A-cluster[65,66]. Under the diamagnetic mechanism hypothesis, the Ni_p(I)-CO is an unproductive, inhibited state of ACS[58]. Many inorganic model complexes support the potential of a diamagnetic Ni_p(0) A-cluster and are able to methylate, carbonylate, and acetylate[10,67,68]. While explaining the EPR silence of ACS, some evidence is incongruent with the diamagnetic mechanism. According to the diamagnetic mechanism, a two-electron reduction is necessary for ACS and requires very low-potential reductants unlikely found *in-vivo*, especially surrounding the electropositive $[Fe_4S_4]$(II) and Ni_d(II), with the Ni(I)-CO is already at -550 mV, a 2-electron reduction would likely be well below -1 V[10,36]. Additionally, no Ni_p(I) or $[Fe_4S_4]$(I)

intermediate has been seen in replete A-clusters during reduction, indicating the functional reduced ACS is electron-delocalized and EPR-silent[34,45].

The paramagnetic mechanism, on the other hand, is strongly supported by the catalytic competence of the Ni_p(I)-CO species, where the rate of decay in Ni-CO signal overlapped closely with methylation and acetyl-CoA production (~ 1 s^{-1}) observed via IR and EPR[55,56], and photolysis of the Ni-CO produced a previously unseen, clean Ni(I) EPR spectrum[36]. XAS evidence for the paramagnetic mechanism was observed when dithionite-treated "reduced" ACS appeared no different for both Ni and Fe than the as-isolated ACS, indicating reducing ACS did not produce any Ni(0) or $[Fe_4S_4]$(I)[34]. Once "reduced", methylation of ACS in the paramagnetic mechanism is expected to produce a highly oxidizing methyl-Ni_p(III), although in the presence of any excess reductant or other reduced species (dithionite, Ti(III) citrate, Co(I), etc.) the methyl-Ni_p(III) could rapidly be reduced to the EPR-silent methyl-Ni_p(II), with precedence seen in the cofactor F_{430} methyl-Ni(III)/Ni(II) midpoint potential in Methyl-CoM Reductase is much more positive than 0 mV[69,70]. Inorganic models also provide as much supporting evidence for the paramagnetic mechanism as the diamagnetic mechanism, as well as artificial metalloenzymatic models, where a nickel-containing azurin scaffold is competent in forming both the Ni(I)-CO and Ni(III)-Me seen in the paramagnetic mechanism[71,72]. The paramagnetic mechanism is not without its problems, of which most glaringly is the lack of EPR evidence for the methyl-Ni_p(III) and the lack of an EPR-active reduced A-cluster[34,56,58].

For the rest of this work, we refer to the paramagnetic mechanism as the favored model. We select this model based on 4 of the previously mentioned key arguments: Unlikely 2-electron reduction of a Ni(II) versus 1-electron reduction; no XAS evidence for a Ni_p(0); observation of a single metal-carbonyl species in the FTIR with a profile that matches that for formation of the Ni(I)-CO; dependence on low-potential reductants for substrate binding; and the kinetic competence of the formation and decay of Ni(I)-CO, these rates matching the rate of acetyl-CoA production.

1.7 Hypotheses of the ACS Mechanism and Dissertation Scope

1.7.1 State of Methylated ACS – A Search for Ni_p-Me

Previous literature has shown stable methylation of ACS, its CO-dependent conversion to a stable acetyl-intermediate, and stoichiometric conversion to acetyl-CoA[62]. However, trapping the proposed methyl-Ni_p intermediate but has yet to be seen, and no methylation is seen in unreduced ACS or ACS without nickel treatment[31,44,46,58]. Previous Mössbauer data indicated the A-cluster was 70% in an $[Fe_4S_4]$(I) state, but this now can be attributed to an $[Fe_4S_4]$ decoupled from the A-cluster in a nickel-deplete ACS, where a NiFeC signal of ~ 25% would represent the corresponding 25% active and Ni-replete A-cluster[46]. More recently, XAS provided no evidence for any reduced Ni_p(0) state or the substantially reduced $[Fe_4S_4]$ seen previously, leading to the belief that the truly reduced ACS state is EPR-silent[34].

Considering the EPR-silence of the reductant-exposed A-cluster, the methyl-Ni_p(III) may manifest in a similar manner, reduced rapidly by any excess reductant in solution, appearing EPR-silent, and masking any discrete electronic changes at the A-cluster[10,45,65,66]. With experimental evidence suggesting the complicated and delocalized nature of the A-cluster in the ACS mechanism for both reduction and carbonylation, we are interested in learning about the redox state of the Ni_p and $[Fe_4S_4]$ after A-cluster methylation in the monofunctional ACS[34,47].

We hypothesize that once methylated, the A-cluster changes from the EPR-silent $[Fe_4S_4]$(II)-Ni_p(II)-Ni_d(II) state to one of two unstable EPR-active states, either $[Fe_4S_4]$(III)-Ni_p(II)(Me)-Ni_d(II) or $[Fe_4S_4]$(II)-Ni_p(III)(Me)-Ni_d(II) that quickly decays to the more stable diamagnetic $[Fe_4S_4]$(II)-Ni_p(II)(Me)-Ni_d(II). We also hypothesize that, as with the as-isolated diamagnetic protein, the active Ni(III)-methyl intermediate is recruited by reaction with CO to generate the acetyl-Ni species. This acetyl-Ni species is likely also subject to a similar Ni(III)/(II) equilibrium, where reaction with CoA returns an acetyl-Ni(III) to the starting state for reaction with either CO to generate Ni(I)-CO or with another methyl group to regenerate the methyl-Ni species. In this work, we examine the state of the methylated A-cluster primarily through isotopic EPR studies, with XAS, ENDOR, and Mössbauer confirmation to probe the involvement of the $[Fe_4S_4]$ and Ni_p after methylation, using methyl-cobinamide substituted for the methyl-CFeSP to reduce background $[Fe_4S_4]$ cluster signal[62].

1.7.2 A Hydrophobic CO Alcove Near the ACS A-Cluster

Crystallographic evidence for the hydrophobic CO channel has been around for nearly two decades, but the first spectroscopic evidence for the putative hydrophobic A-cluster alcove was seen in 2010, when Bender, et al. published the first work to show a $Ni_p(I)$ EPR-active ACS without CO bound to the reduced A-cluster, observed through photolysis of the Ni-CO bond at very low temperatures[14,45]. The photolysis of the Ni-CO bond was confirmed by absence of a characteristic IR signal of 1995 cm^{-1} by FTIR, where the rates of photolysis and rebinding were measured. Through the time dependent IR changes, the energy of rebinding for CO the ACS A-cluster after photolysis was calculated to be ~1 kJ/mol, implying the alcove plays an integral role in maintaining CO near the nickel active site.

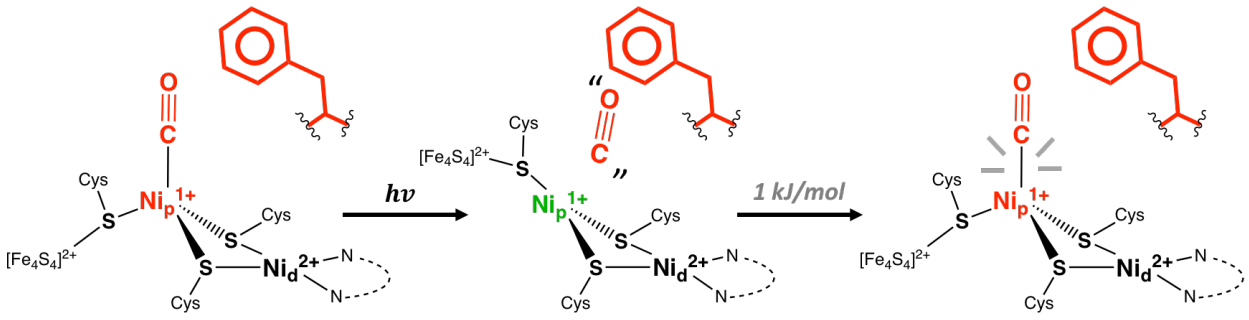

Figure 1.9 Schematic representation of the low-temperature CO photolysis experiment. The photolysis experiment from 2010 shows the hypothesized F229 residue thought to play a critical role in maintaining a low barrier to rebinding of CO in ACS[45]. The carbonylated ACS (*left*) is illuminated with white light at low temperatures to photolyze the Ni-CO bond (*middle*) and reannealed at 40K for short increments of time to re-establish the Ni-CO (*right*). The energy barrier to rebinding based on temperature and rate constants was found to be ~1 kJ/mol, indicating a mechanism to maintain CO nearby.

In conjunction with the structural evidence seen in high-pressure xenon X-ray crystal model, we provide evidence here that the alcove has been proposed to be a critical component in maintaining CO near the A-cluster, facilitating the low barrier to CO rebinding (Figures 1.9 and 1.10). One residue thought to play a particularly critical role in the function of this CO alcove is phenylalanine 229 (F229), which forms a significant portion of one of the alcove walls. In the high-pressure xenon crystallographic model, the F229 residue appears to be cradling the xenon closely to the Ni_p in the A-cluster and may improve the affinity of the Ni-CO bond, lowering the K_d.

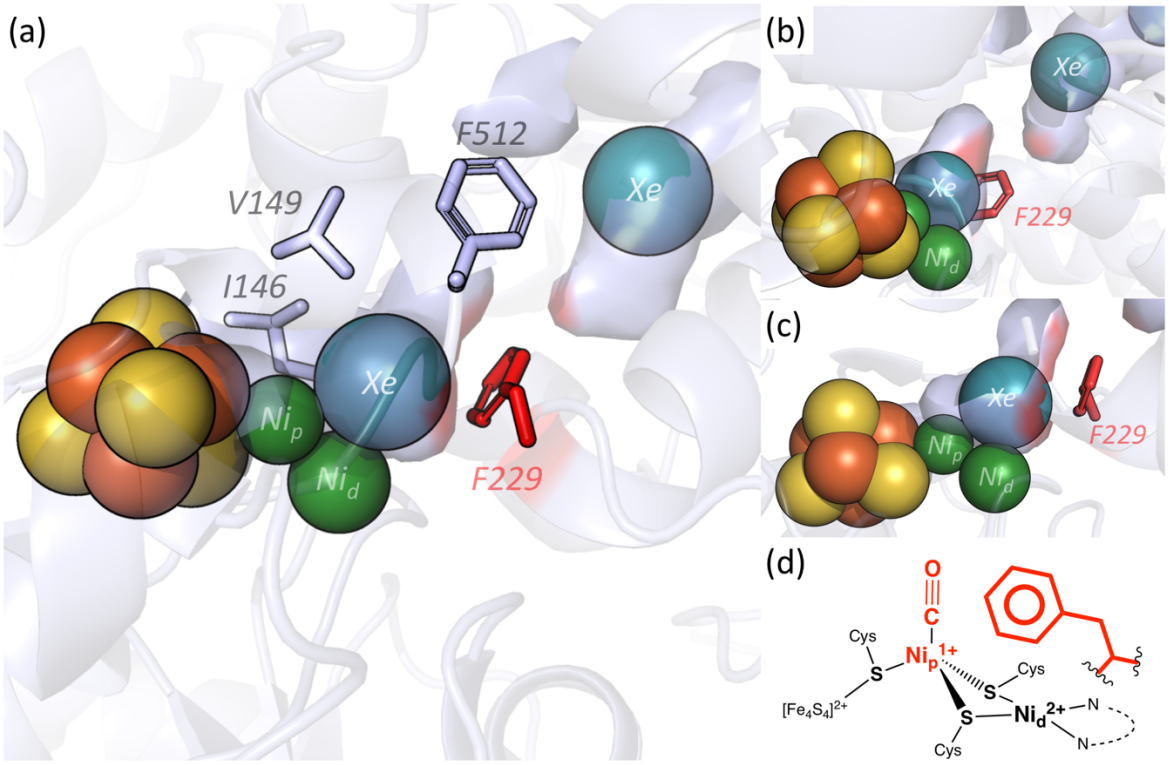

Figure 1.10 A hydrophobic alcove at the end of the CO channel near the ACS A-cluster. (a) The residues composing the hydrophobic alcove near the A-cluster, with F229 (red) forming a large portion of the alcove's surface. Another key alcove residue, G145, is located behind the A-cluster. (b) and (c) Different perspectives of residue F229 in relation to the CO channel. (d) Schematic representation of F229 in relation to the A-cluster. Iron (burnt orange), Nickel (forest green), and Xenon (teal) represented in spheres. Residues (blue, red) represented in sticks. PDB 2Z8Y.

In this work, we ask what purpose the alcove plays in binding the CO substrate at the ACS A-cluster, and how the lack of the alcove affects this ability. In order to determine the significance of this alcove we created two ACS alcove variants: one alanine variant (F229A) that is lacking the F229 residue, and a tryptophan variant (F229W) that is expected to have a similar function to native ACS (wildtype; WT). These variants were compared amongst themselves, and their differences are reported within this work.

1.8 References for Chapter 1

(1) Rabiu, K. O.; Han, L.; Bhusan Das, D.; Abraham, M. A. In *Encyclopedia of Sustainable Technologies*; Elsevier: Oxford, 2017.

(2) Metz, B.; Davidson, O.; de Coninck, H.; Loos, M.; Meyer, L. IPCC special report on carbon dioxide capture and storage. **2005**.
(3) Le Berre, C.; Serp, P.; Kalck, P.; Torrence, G. P. Acetic Acid. *Ullmann's Encyclopedia of Industrial Chemistry* **2014**, 1.
(4) Liew, F.; Martin, M. E.; Tappel, R. C.; Heijstra, B. D.; Mihalcea, C.; Köpke, M. Gas Fermentation—A Flexible Platform for Commercial Scale Production of Low-Carbon-Fuels and Chemicals from Waste and Renewable Feedstocks. *Frontiers in Microbiology* **2016,** *7*, 694.
(5) Ragsdale, S. W.; Pierce, E. Acetogenesis and the Wood-Ljungdahl pathway of CO(2) fixation. *Biochimica et Biophysica Acta* **2008,** *1784* (12), 25.
(6) Adam, P. S.; Borrel, G.; Gribaldo, S. Evolutionary history of carbon monoxide dehydrogenase/acetyl-CoA synthase, one of the oldest enzymatic complexes. *Proceedings of the National Academy of Sciences* **2018,** *115* (6), E1166.
(7) Martin, W. Hydrogen, metals, bifurcating electrons, and proton gradients: The early evolution of biological energy conservation. *FEBS letters* **2012,** *586*, 485.
(8) Borrel, G.; Adam, P. S.; Gribaldo, S. Methanogenesis and the Wood–Ljungdahl Pathway: An Ancient, Versatile, and Fragile Association. *Genome Biology and Evolution* **2016,** *8* (6), 1706.
(9) Martin, W. F. and Müller, M.. The hydrogen hypothesis for the first eukaryote. Nature, 392: 37-41, 10.1038/32096. *Nature* **1998,** *392*, 37.
(10) Can, M.; Armstrong, F. A.; Ragsdale, S. W. Structure, Function, and Mechanism of the Nickel Metalloenzymes, CO Dehydrogenase, and Acetyl-CoA Synthase. *Chemical Reviews* **2014,** *114* (8), 25.
(11) Zhuang, W.-Q.; Yi, S.; Bill, M.; Brisson, V. L.; Feng, X.; Men, Y.; Conrad, M. E.; Tang, Y. J.; Alvarez-Cohen, L. Incomplete Wood–Ljungdahl pathway facilitates one-carbon metabolism in organohalide-respiring *Dehalococcoides mccartyi*. *Proceedings of the National Academy of Sciences* **2014,** *111* (17), 6419.
(12) Doukov, T. I.; Iverson, T. M.; Seravalli, J.; Ragsdale, S. W.; Drennan, C. L. A Ni-Fe-Cu Center in a Bifunctional Carbon Monoxide Dehydrogenase/ Acetyl-CoA Synthase. *Science* **2002,** *298* (5593), 567.
(13) Darnault, C.; Volbeda, A.; Kim, E. J.; Legrand, P.; Vernède, X.; Lindahl, P. A.; Fontecilla-Camps, J. C. Ni-Zn-[Fe4-S4] and Ni-Ni-[Fe4-S4] clusters in closed and open α subunits of acetyl-CoA synthase/carbon monoxide dehydrogenase. *Nature Structural Biology* **2003,** *10*, 271.
(14) Doukov, T. I.; Blasiak, L. C.; Seravalli, J.; Ragsdale, S. W.; Drennan, C. L. Xenon in and at the End of the Tunnel of Bifunctional Carbon Monoxide Dehydrogenase/Acetyl-CoA Synthase. *Biochemistry* **2008,** *47* (11), 9.
(15) Seravalli, J.; Xiao, Y.; Gu, W.; Cramer, S. P.; Antholine, W. E.; Krymov, V.; Gerfen, G. J.; Ragsdale, S. W. Evidence That NiNi Acetyl-CoA Synthase Is Active and That the CuNi Enzyme Is Not. *Biochemistry* **2004,** *43* (13), 11.
(16) Seravalli, J.; Gu, W.; Tam, A.; Strauss, E.; Begley, T. P.; Cramer, S. P.; Ragsdale, S. W. Functional copper at the acetyl-CoA synthase active site. *Proceedings of the National Academy of Sciences* **2003,** *100* (7), 5.
(17) Liew, F.; Henstra, A. M.; Winzer, K.; Köpke, M.; Simpson, S. D.; Minton, N. P. Insights into CO_2 Fixation Pathway of *Clostridium autoethanogenum* by Targeted Mutagenesis. *mBio* **2016,** *7* (3), e00427.
(18) Tan, X.; Volbeda, A.; Fontecilla-Camps, J. C.; Lindahl, P. A. Function of the tunnel in acetylcoenzyme A synthase/carbon monoxide dehydrogenase *Journal of Biological Inorganic Chemistry* **2006,** *11*, 7.
(19) Seravalli, J.; Ragsdale, S. W. Channeling of Carbon Monoxide during Anaerobic Carbon Dioxide Fixation. *Biochemistry* **2000,** *39* (6), 1274.
(20) Maynard, E. L.; Lindahl, P. A. Evidence of a Molecular Tunnel Connecting the Active Sites for CO_2 Reduction and Acetyl-CoA Synthesis in Acetyl-CoA Synthase from C*lostridium thermoaceticum*. *Journal of the American Chemical Society* **1999,** *121* (39), 2.
(21) Volbeda, A.; Fontecilla-Camps, J. C. Crystallographic evidence for a CO/CO_2 tunnel gating mechanism in the bifunctional carbon monoxide dehydrogenase/acetyl coenzyme A synthase from *Moorella thermoacetica*. *JBIC Journal of Biological Inorganic Chemistry* **2004,** *9* (5), 525.
(22) Ragsdale, S. W.; Kumar, M. Nickel-Containing Carbon Monoxide Dehydrogenase/Acetyl-CoA Synthase. *Chemical Reviews* **1996,** *96* (7), 25.
(23) Ramer, S. E.; Raybuck, S. A.; Orme-Johnson, W. H.; Walsh, C. T. Kinetic characterization of the [3'-32P] coenzyme A/acetyl coenzyme A exchange catalyzed by a three-subunit form of the carbon monoxide dehydrogenase/acetyl-CoA synthase from *Clostridium thermoaceticum*. *Biochemistry* **1989,** *28* (11), 4675.
(24) Lindahl, P. Nickel-carbon bonds in acetyl-coenzyme a synthases/carbon monoxide dehydrogenases. *Metal ions in life sciences* **2009,** *6*, 133.

(25) Shin, W.; Lindahl, P. A. Discovery of a labile nickel ion required for CO/acetyl-CoA exchange activity in the NiFe complex of carbon monoxide dehydrogenase from *Clostridium thermoaceticum*. *Journal of the American Chemical Society* **1992,** *114* (24), 9718.
(26) Burton, R.; Can, M.; Esckilsen, D.; Wiley, S.; Ragsdale, S. W.; Armstrong, F. In *Methods in Enzymology*; Academic Press, 2018; Vol. 613.
(27) Russell, W. K.; Stålhandske, C. M. V.; Xia, J.; Scott, R. A.; Lindahl, P. A. Spectroscopic, Redox, and Structural Characterization of the Ni-Labile and Nonlabile Forms of the Acetyl-CoA Synthase Active Site of Carbon Monoxide Dehydrogenase. *Journal of the American Chemical Society* **1998,** *120* (30), 7502.
(28) Lindahl, P. A. Acetyl-coenzyme A synthase: the case for a Ni_p0-based mechanism of catalysis. *Journal of Biological Inorganic Chemistry* **2004,** *9*, 8.
(29) Maret, W. The redox biology of redox-inert zinc ions. *Free Radical Biology and Medicine* **2019,** *134*, 311.
(30) Bramlett, M. R.; Tan, X.; Lindahl, P. A. Inactivation of Acetyl-CoA Synthase/Carbon Monoxide Dehydrogenase by Copper. *Journal of the American Chemical Society* **2003,** *125* (31), 9316.
(31) Tan, X.; Bramlett, M. R.; Lindahl, P. A. Effect of Zn on Acetyl Coenzyme A Synthase: Evidence for a Conformational Change in the α Subunit during Catalysis. *Journal of the American Chemical Society* **2004,** *126* (19), 5954.
(32) McCall, K. A.; Huang, C.-c.; Fierke, C. A. Function and Mechanism of Zinc Metalloenzymes. *The Journal of Nutrition* **2000,** *130* (5), 1437S.
(33) Svetlitchnyi, V.; Dobbek, H.; Meyer-Klaucke, W.; Meins, T.; Thiele, B.; Römer, P.; Huber, R.; Meyer, O. A functional Ni-Ni-[4Fe-4S] cluster in the monomeric acetyl-CoA synthase from *Carboxydothermus hydrogenoformans*. *Proceedings of the National Academy of Sciences of the United States of America* **2004,** *101* (2), 446.
(34) Can, M.; Giles, L. J.; Ragsdale, S. W.; Sarangi, R. X-ray Absorption Spectroscopy Reveals an Organometallic Ni–C Bond in the CO-Treated Form of Acetyl-CoA Synthase. *Biochemistry* **2017,** *56* (9), 12.
(35) Seravalli, J.; Ragsdale, S. W. Pulse-Chase Studies of the Synthesis of Acetyl-CoA by CarbonMonoxide Dehydrogenase/Acetyl-CoA Synthase: Evidence for a Random Mechanism of Methyl and Carbonyl Addition. *Journal of Biological Chemistry* **2007,** *283* (13), 10.
(36) Bender, G.; Ragsdale, S. W. Evidence That Ferredoxin Interfaces with an Internal Redox Shuttle in Acetyl-CoA Synthase during Reductive Activation and Catalysis. *Biochemistry* **2011,** *50* (2), 276.
(37) Rabus, R.; Venceslau, S. S.; Wöhlbrand, L.; Voordouw, G.; Wall, J. D.; Pereira, I. A. C.; Poole, R. K. In *Advances in Microbial Physiology*; Academic Press, 2015; Vol. 66.
(38) Raybuck, S. A.; Bastian, N. R.; Orme-Johnson, W. H.; Walsh, C. T. Kinetic characterization of the carbon monoxide-acetyl-CoA (carbonyl group) exchange activity of the acetyl-CoA synthesizing carbon monoxide dehydrogenase from *Clostridium thermoaceticum*. *Biochemistry* **1988,** *27* (20), 4.
(39) Svetlitchnaia, T.; Svetlitchnyi, V.; Meyer, O.; Dobbek, H. Structural insights into methyltransfer reactions of a corrinoid iron–sulfur protein involved in acetyl-CoA synthesis. *Proceedings of the National Academy of Sciences* **2006,** *103* (39), 14331.
(40) Ando, N.; Kung, Y.; Can, M.; Bender, G.; Ragsdale, S. W.; Drennan, C. L. Transient B_{12}-Dependent Methyltransferase Complexes Revealed by Small-Angle X-ray Scattering. *Journal of the American Chemical Society* **2012,** *134* (43), 17945.
(41) Kung, Y.; Ando, N.; Doukov, T. I.; Blasiak, L. C.; Bender, G.; Seravalli, J.; Ragsdale, S. W.; Drennan, C. L. Visualizing molecular juggling within a B_{12}-dependent methyltransferase complex. *Nature* **2012,** *484* (7393), 265.
(42) Loke, H.-K.; Bennett, G. N.; Lindahl, P. A. Active acetyl-CoA synthase from *Clostridium thermoaceticum* obtained by cloning and heterologous expression of *acsAB* in *Escherichia coli*. *Proceedings of the National Academy of Sciences* **2000,** *97* (23), 12530.
(43) Shanmugasundaram, T.; Wood, H. G. Interaction of ferredoxin with carbon monoxide dehydrogenase from *Clostridium thermoaceticum*. *Journal of Biological Chemistry* **1992,** *267* (2), 3.
(44) Maynard, E. L.; Tan, X.; Lindahl, P. A. Autocatalytic activation of acetyl-CoA synthase. *JBIC Journal of Biological Inorganic Chemistry* **2004,** *9* (3), 316.
(45) Bender, G.; Stitch, T. A.; Yan, L.; Britt, R. D.; Cramer, S. P.; Ragsdale, S. W. Infrared and EPR Spectroscopic Characterization of a Ni(I) Species Formed by Photolysis of a Catalytically Competent Ni(I)-CO Intermediate in the Acetyl-CoA Synthase Reaction. *Biochemistry* **2010,** *49* (35), 7.

(46) Bramlett, M. R.; Stubna, A.; Tan, X.; Surovtsev, I. V.; Münck, E.; Lindahl, P. A. Mössbauer and EPR Study of Recombinant Acetyl-CoA Synthase from *Moorella thermoacetica*. *Biochemistry* **2006,** *45* (28), 8674.
(47) Ragsdale, S. W.; Ljungdahl, L. G.; DerVartanian, D. V. ^{13}C and ^{61}Ni isotope substitutions confirm the presence of a nickel(III)-carbon species in acetogenic CO dehydrogenases. *Biochemical and Biophysical Research Communications* **1983,** *115* (2), 7.
(48) Ragsdale, S. W.; Wood, H. G.; Antholine, W. E. Evidence that an iron-nickel-carbon complex is formed by reaction of CO with the CO dehydrogenase from *Clostridium thermoaceticum*. *Proceedings of the National Academy of Sciences* **1985,** *82* (20), 6811.
(49) Gorst, C. M.; Ragsdale, S. W. Characterization of the NiFeCO complex of carbon monoxide dehydrogenase as a catalytically competent intermediate in the pathway of acetyl-coenzyme A synthesis. *Journal of Biological Chemistry* **1991,** *266* (31), 20687.
(50) Shin, W.; Lindahl, P. A. Low spin quantitation of NiFeC EPR signal from carbon monoxide dehydrogenase is not due to damage incurred during protein purification. *Biochimica et Biophysica Acta (BBA) - Protein Structure and Molecular Enzymology* **1993,** *1161* (2), 317.
(51) Barondeau, D. P.; Lindahl, P. A. Methylation of Carbon Monoxide Dehydrogenase from *Clostridium thermoaceticum* and Mechanism of Acetyl Coenzyme A Synthesis. *Journal of the American Chemical Society* **1997,** *119* (17), 3959.
(52) Fee, J. A. In *Methods in Enzymology*; Academic Press, 1978; Vol. 49.
(53) Chen, J.; Huang, S.; Seravalli, J.; Gutzman, H.; Swartz, D. J.; Ragsdale, S. W.; Bagley, K. A. Infrared Studies of Carbon Monoxide Binding to Carbon Monoxide Dehydrogenase/Acetyl-CoA Synthase from *Moorella thermoacetica*. *Biochemistry* **2003,** *42* (50), 14822.
(54) Kumar, M.; Ragsdale, S. W. Characterization of the carbon monoxide binding site of carbon monoxide dehydrogenase from *Clostridium thermoaceticum* by infrared spectroscopy. *Journal of the American Chemical Society* **1992,** *114* (22), 8713.
(55) George, S. J.; Seravalli, J.; Ragsdale, S. W. EPR and Infrared Spectroscopic Evidence That a Kinetically Competent Paramagnetic Intermediate is Formed When Acetyl-Coenzyme A Synthase Reacts with CO. *Journal of the American Chemical Society* **2005,** *127* (39), 1.
(56) Seravalli, J.; Kumar, M.; Ragsdale, S. W. Rapid Kinetic Studies of Acetyl-CoA Synthesis: Evidence Supporting the Catalytic Intermediacy of a Paramagnetic NiFeC Species in the Autotrophic Wood−Ljungdahl Pathway. *Biochemistry* **2002,** *41* (6), 1807.
(57) Xia, J.; Hu, Z.; Popescu, C. V.; Lindahl, P. A.; Münck, E. Mössbauer and EPR Study of the Ni-Activated α-Subunit of Carbon Monoxide Dehydrogenase from *Clostridium thermoaceticum*. *Journal of the American Chemical Society* **1997,** *119* (35), 8301.
(58) Tan, X.; Sewell, C.; Lindahl, P. A. Stopped-Flow Kinetics of Methyl Group Transfer between the Corrinoid-Iron-Sulfur Protein and Acetyl-Coenzyme A Synthase from C*lostridium thermoaceticum*. *Journal of the American Chemical Society* **2002,** *124* (22), 7.
(59) Menon, S.; Ragsdale, S. W. Evidence That Carbon Monoxide Is an Obligatory Intermediate in Anaerobic Acetyl-CoA Synthesis. *Biochemistry* **1996,** *35* (37), 12119.
(60) James, C. D.; Wiley, S.; Ragsdale, S. W.; Hoffman, B. M. ^{13}C Electron Nuclear Double Resonance Spectroscopy Shows Acetyl-CoA Synthase Binds Two Substrate CO in Multiple Binding Modes and Reveals the Importance of a CO-Binding 'Alcove'. *bioRxiv* **2020**, 2020.06.23.165407.
(61) Menon, S.; Ragsdale, S. W. The Role of an Iron-Sulfur Cluster in an Enzymatic Methylation Reaction: METHYLATION OF CO DEHYDROGENASE/ACETYL-CoA SYNTHASE BY THE METHYLATED CORRINOID IRON-SULFUR PROTEIN. *Journal of Biological Chemistry* **1999,** *274* (17), 11513.
(62) Seravalli, J.; Brown, K. L.; Ragsdale, S. W. Acetyl Coenzyme A Synthesis from Unnatural Methylated Corrinoids: Requirement for "Base-Off" Coordination at Cobalt. *Journal of the American Chemical Society* **2001,** *123* (8), 1786.
(63) Gutiérrez-Sanz, O.; Rüdiger, O.; De Lacey, A. L. In *Metalloproteins: Methods and Protocols*; Humana Press: Totowa, NJ, 2014.
(64) Grahame, D. A.; Khangulov, S.; DeMoll, E. Reactivity of a Paramagnetic Enzyme−CO Adduct in Acetyl-CoA Synthesis and Cleavage. *Biochemistry* **1996,** *35* (2), 593.
(65) Eaton, S. S.; Eaton, G. R. The world as viewed by and with unpaired electrons. *Journal of magnetic resonance (San Diego, Calif. : 1997)* **2012,** *223*, 151.
(66) Telser, J.; Pardi, L. A.; Krzystek, J.; Brunel, L.-C. EPR Spectra from "EPR-Silent" Species: High-Field EPR Spectroscopy of Aqueous Chromium(II). *Inorganic Chemistry* **1998,** *37* (22), 5769.

(67) Horn, B.; Limberg, C.; Herwig, C.; Mebs, S. The conversion of nickel-bound CO into an acetyl thioester: organometallic chemistry relevant to the acetyl coenzyme A synthase active site. *Angewandte Chemie International Edition* **2011,** *50* (52), 4.
(68) Harrop, T. C.; Mascharak, P. K. Structural and spectroscopic models of the A-cluster of acetyl coenzyme a synthase/carbon monoxide dehydrogenase: Nature's Monsanto acetic acid catalyst. *Coordination Chemistry Reviews* **2005,** *249* (24), 3007.
(69) Thauer, R. K. Biochemistry of methanogenesis: a tribute to Marjory Stephenson:1998 Marjory Stephenson Prize Lecture. **1998,** *144* (9), 2377.
(70) Jaun, B. Coenzyme F430 from Methanogenic Bacteria: Oxidation of F430 Pentamethyl Ester to the Ni(III) Form. *Helvetica Chimica Acta* **1990,** *73* (8), 2209.
(71) Manesis, A. C.; Musselman, B. W.; Keegan, B. C.; Shearer, J.; Lehnert, N.; Shafaat, H. S. A Biochemical Nickel(I) State Supports Nucleophilic Alkyl Addition: A Roadmap for Methyl Reactivity in Acetyl Coenzyme A Synthase. *Inorganic Chemistry* **2019,** *58* (14), 8969.
(72) Manesis, A. C.; O'Connor, M. J.; Schneider, C. R.; Shafaat, H. S. Multielectron Chemistry within a Model Nickel Metalloprotein: Mechanistic Implications for Acetyl-CoA Synthase. *Journal of the American Chemical Society* **2017,** *139* (30), 10328.

Chapter 2
The Methylated State of ACS

2.1 Introduction

The Wood-Ljungdahl pathway (WLP) of acetogenesis, also known as the reductive acetyl-Coenzyme A (CoA) pathway, is an ancient, anaerobic, organometallic, and autotrophic pathway shared by both acetogenic bacteria and methanogenic archaea that allows the reversible conversion of inorganic gases (CO_2, CO, H_2) into biologically available carbon and energy to be used in the cell[1,2]. Within *Moorella thermoacetica*, the WLP reduces carbon dioxide through two geographically-labeled branches, the Western branch (Case-Western Universty) containing the carbon monoxide dehydrogenase/acetyl-CoA synthase (CODH/ACS) enzyme pair and the Eastern branch (University of Georgia) with formate dehydrogenase (FDR), 5,10-methylene-H_4folate cyclohydrolase/dehydrogenase, methyltransferase (MeTr), and corrinoid iron-sulfur protein (CFeSP)[2-6]. The Eastern and Western branches meet at acetyl-CoA synthase (ACS) where the two substrates are condensed into an acetyl group and transferred to form acetyl-CoA[6-9].

CODH/ACS functions as the key enzyme pair within the WLP, and since the identification of a nickel-, iron-, and carbon-dependent electron paramagnetic resonance (EPR) signal in 1985[9], the complex has been known to utilize organometallic chemistry in condensing CO and methyl into an acetyl group[10]. Because of its observed NiFeC EPR signal, ACS has been likened to nature's Monsanto process of acetic acid production[11]. Through crystallographic, spectroscopic, and kinetic experiments the CODH/ACS complex was determined to contain a total of 4 unique [Fe_4S_4] clusters, labeled A to D, in which the C- and A-clusters were identified as CODH and ACS active sites whereas the B- and D-clusters facilitate electron transfer between external redox mediators[12-15]. The C-cluster of CODH is a distorted, Ni-containing [Fe_4S_4][16], and the A-cluster found in ACS contains an [Fe_4S_4]-Ni_p-Ni_d architecture[15,17-19].

First, CODH reduces CO_2 to CO at the C-cluster, then the CO is shuttled along a 67 Å channel to the ACS A-cluster[12], where the CO and methyl group from CFeSP are condensed into an acetyl group and ultimately transferred to CoA[20]. The ACS mechanism is random, and after reduction,

ACS can bind either the CO or methyl first. Once the first substrate is bound to the A-cluster, the complimentary substrate is hypothesized to bind, where the CO and methyl rearrange to form the acetyl-nickel that is transferred to CoA.

Numerous spectroscopic experiments, including EPR[9,21,22], FTIR[23-25], and ENDOR[26], have confirmed the existence of a catalytically competent[27,28] organometallic Ni-CO bond at the ACS A-cluster. In 2017, XAS experiments indicated a transition from a square planar Ni(II) to a tetrahedral Ni(I)-CO at the Ni_p in the A-cluster after exposure to CO in the presence of reductant[10], but also importantly implied a chemically-coupled redox transition from the EPR-silent $[Fe_4S_4]$-Ni_p(II)-Ni_d(II) to the EPR-active CO bound A-cluster.

In contrast to the carbonylated ACS, the methylated state has been more difficult to spectroscopically resolve and much of what is known of the methylated ACS state is based on indirect experimental evidence[20,29-31]. ACS must be nickel-replete[17] and requires low-potential reductants to accept a methyl group from the "base-off" methyl-Co(III)alamin cofactor in partner CFeSP[30,32,33]. UV-visible kinetic data is consistent with an organometallic methyl transfer from CFeSP to ACS with a K_{eq} of ~ 2.3[31], strongly indicating the location of methylation on ACS must be a stronger nucleophile than the Cob(I)alamin in CFeSP, of which a reduced nickel could accomplish[34]. Based on crystallographic studies showing ACS's conformational flexibility, the open state is poised for the methyl group to bind to the solvent-exposed Ni_p without changing the resting square-planar geometry[15]. While the state of the methylated A-cluster is anticipated and implied to be an organometallic methyl-Ni, whether this organometallic intermediate exists has remained explicitly unresolved until this work. It is important to note that while the organometallic methyl-Ni intermediate is favored, an alternative EPR-silent mode of ACS methyl binding has been proposed to exist as a methyl-cysteine[35]. The methylated-cysteine hypothesis was first proposed in part from experiments suggesting ^{14}C-methyl bound to ACS which was able to convert to [2-^{14}C]-acetyl-CoA[35].

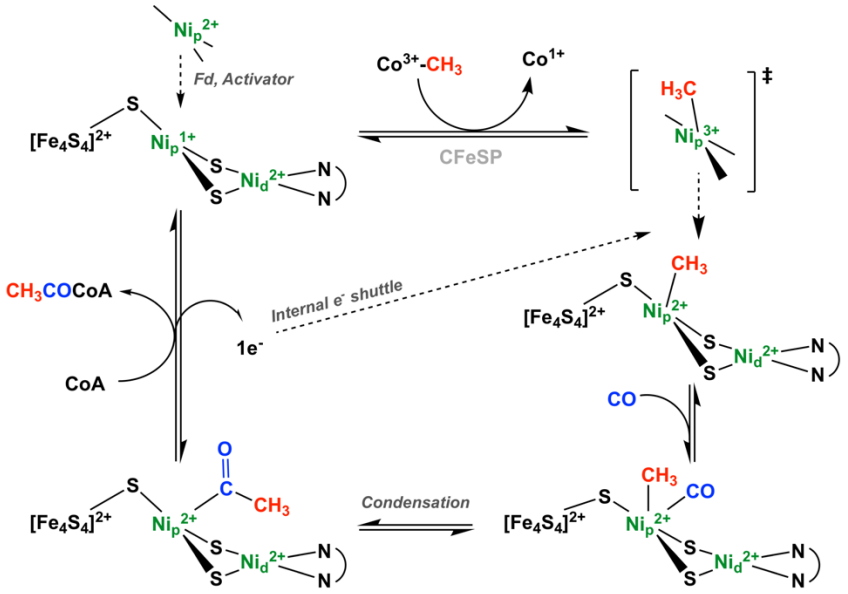

Figure 2.1 Schematic representation of the paramagnetic mechanism. Clockwise from top left; ACS is reduced by an external redox mediator such as ferredoxin, CFeSP transfers a methyl to the A-cluster via S_N2 nucleophilic transfer forming an oxidizing methyl-Ni(III). The methyl-Ni(III) is rapidly reduced to methyl-Ni(II), and once CO is bound, the two substrates condense to an acetyl-Ni(II), and transferred to coenzyme A. Scheme adapted from Can, 2014.

In addition to the likely organometallic methyl-Ni, earlier conclusions from EPR and Mössbauer experiments of the reduced and methylated recombinant ACS are in conflict with the more recent XAS data with respect to the participation of the A-cluster's $[Fe_4S_4]$[10,36]. Without sufficient nickel, the A-cluster decouples and the $[Fe_4S_4]$ becomes readily reducible to an observed $[Fe_4S_4]$(I)[17,36,37]. We aim to revisit and resolve the role of the $[Fe_4S_4]$ in the methylated state of ACS and confirm the putative organometallic methyl-Ni intermediate. We also want to know if changes in the $[Fe_4S_4]$ provide insight into the A-cluster's overall redox state, and whether the cluster acts as the putative "mystery" electron source[7] for the proposed highly-oxidizing methyl-Ni_p(III) intermediate[38,39] (Figure 2.1).

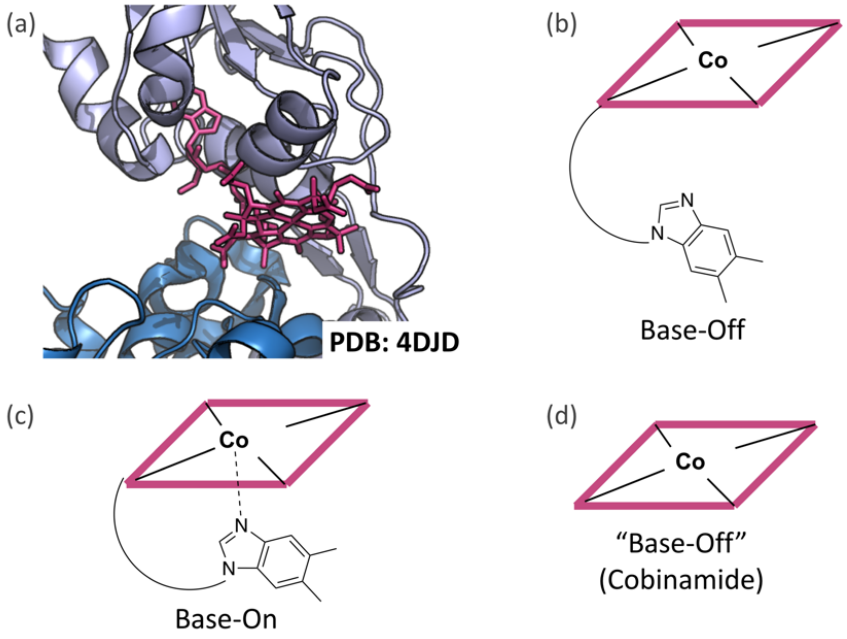

Figure 2.2 Cobinamide as an analog for CFeSP. (a) CFeSP binds its cobalamin cofactor with its dimethylbenzimidazole ring in the base-off form. (b) Schematic representation of a base-off cobalamin. (c) Schematic representation of a base-on cobalamin. (d) Schematic representation of cobinamide and its similarity to the base-off cobalamin.

In this work, we used EPR spectroscopy to probe the paramagnetic character associated with the state of the A-cluster after methylation by methyl-Co(III)binamide (MeCbi), a methyl donor analogous to partner CFeSP[30], as depicted in Figure 2.2. MeCbi was chosen due to its similarity to CFeSP's base-off cobalamin cofactor and to reduce any excess paramagnetic signal from the CFeSP iron-sulfur cluster. Additionally, we used monofunctional ACS in lieu of CODH/ACS in order to reduce any excess nickel or iron signal. The methylation rate of MeCbi is slightly slower (~100-fold) than CFeSP, but much faster (~1700-fold) than methyl-cobalamin, allowing for more reliable observation via hand-mixed UV-visible spectrophotometry[30]. Using the electron-nuclear spin interaction effect of non-integer nuclei ($I \neq 1, 2, 3\ldots$ etc.), isotopically labeled nickel and iron in ACS and methyl isotopes were used to resolve the identities of resultant paramagnetic spectra after methylation. Our EPR findings were confirmed and expanded with Mössbauer, XAS, and ENDOR spectroscopies.

2.2 Materials & Methods

2.2.1 Materials

All chemicals and reagents were procured from Sigma Aldrich unless otherwise noted. Labeled methyl iodide $^{13}CH_3I$ (99% ^{13}C), CD_3I (99.95% ^{12}C; 99.5% D_3), and $^{13}CD_3I$ (99% ^{13}C; 99% D_3) used to prepare methyl-cobinamide were purchased from Cambridge Isotope Laboratories (Tewksbury, MA). ^{61}Ni (Growth = 91%; Reconstitution = 99.42%) and ^{57}Fe (95.56%) were purchased form Isoflex USA (San Francisco, CA). Ultrapure gases of N_2 and CO were sourced from Cryogenic Gases (Detroit, MI). Fermentation done in an Eppendorf (Hamburg, Germany) 10 L double-jacket bioreactor fermenter using the New Brunswick™ BioFlo 110 system. TEV-cleavable His_6-tagged ACS expression plasmid is a kanamycin-resistant, *lac*-inducible pET29a harboring the *acsB* gene from *Moorella thermoacetica*. Iron-sulfur cluster assembly machinery co-expression plasmid is an ampicillin-resistant, *ara*-inducible pdb1282 harboring the *isc* operon from *Azotobacter vinelandii*. Ni-NTA resin used to purify ACS was from Qiagen (Valencia, CA). Bio-Gel P-2 resin from Bio-Rad Laboratories, Inc. (Hercules, CA) was used to purify methyl-cobinamide after synthesis. Red head lamp used for dark work was sourced from Black Diamond Equipment, Ltd. (Salt Lake City, UT). TEV protease was purified and provided by Dr. Angela Fleischhacker and Liu Liu.

2.2.2 General Methods

All experiments and preparations were performed under strictly anaerobic conditions (≤ 1.5 ppm O_2) unless otherwise noted. Unlabeled ACS was grown, expressed, purified, and reconstituted according to established methods[3]. Isotopically labeled ACS was produced as established, but 1 L starter culture cells were pelleted at 6000 rpm for 15 minutes and resuspended with bioreactor media instead of direct inoculation of 10 L bioreactor with 1 L starter. ^{61}Ni and ^{57}Fe powders were dissolved anaerobically in concentrated HNO_3 (~70%) and in concentrated HCl (~37%), respectively. Acid-dissolved solutions of ^{61}Ni and ^{57}Fe were directly added to the 10 L bioreactor media to final concentrations of 30 μM each. For ACS reconstitution, ^{61}Ni and ^{57}Fe are neutralized with anaerobically prepared 12 M sodium hydroxide before addition to ACS and 72-hour incubation at 45˚C. Metal content was assessed via ICP-OES by the Center for Applied Isotope Studies (CAIS) at the Univeristy of Georgia (Athens, GA). All reactions and syntheses

involving methyl-cobinamide were conducted in darkness with a red head lamp unless otherwise noted. Titanium (III) citrate was prepared as described in Seefeldt, 1994[40].

2.2.3 Preparation of Natural Abundance and Isotopically-Labeled Methyl-Cobinamide

Natural abundance (NA) and labeled methyl iodide (MeI) solutions were prepared in brown glass vials at 4˚C on ice to 40% MeI in methanol (MeOH), stoppered and crimped with butyl septa, and were made anoxic by exchanging the headspace with nitrogen for 5 minutes. In accordance with Wedemeyer-Exl, 2008[41] methyl-cobinamide and isotopomers were synthesized by initial mixture of 1 equivalent cobinamide and 5 equivalents of Ti(III) citrate in a brown glass vial, in which the mixture is then stoppered with a butyl septum and 200 equivalents of the labeled or unlabeled anoxic 40% MeI/MeOH solution is added via syringe. Once combined, the mixture was left to react anaerobically in a stoppered brown glass vial away from light for at least two hours. Upon completion, the mixture was passed through a 1.0 cm diameter column with 1.5 mL Biogel P-2 size-exclusion (100-1800 MW fractional range) resin equilibrated with 50 mM potassium phosphate, pH 7.5. Fractions were collected in half-milliliter volumes and assessed via UV-visible spectrophotometry. Fractions with pure methyl-cobinamide were pooled, where the final concentration and purity was calculated using ε_{470} = 10.8 mM^{-1} cm^{-1}.

2.2.4 UV-Visible Spectroscopy of ACS Methylation

UV-visible spectroscopic experiments were performed anoxically in a quartz cuvette using an Ocean Optics Mikropack (Ostfildern, Germany) DH-2000 deuterium tungsten-halogen light source. Figure 2.3 depicts the UV-visible absorption spectra of pure methyl-Cob(III)inamide and Cob(I)inamide. Prior to addition of methyl-cobinamide, 10 µM ACS was mixed with 0.5, 1.5, or 3 equivalents (5, 15, or 30 µM) of Ti(III) citrate in 50 mM potassium phosphate, pH 7.5 buffer and baselined. After the reduced ACS was baseline, methyl-cobinamide was added to a final concentration of 10 µM, where the absorbance changes indicative of methyl transfer from methyl-cobinamide, the increase at 390 nm and decrease at 470 nm, to ACS were monitored. The ACS methylation percentage was calculated in comparison to the extinction coefficient change at 390 nm of 17 mM^{-1} cm^{-1} ($\Delta\varepsilon_{390}$ = 17 mM^{-1} cm^{-1}) between pure Cob(I)inamide (ε_{390} = 25 mM^{-1} cm^{-1}) and pure methyl-Cob(III)inamide (ε_{390} = 8 mM^{-1} cm^{-1}).

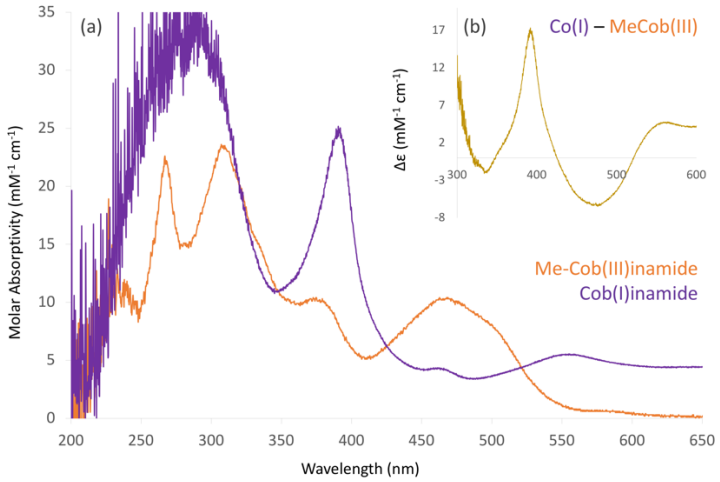

Figure 2.3 Spectral differences between methyl-Cob(III)inamide and Cob(I)inamide. (a) Absorption spectra corresponding to the methy-Cob(III)inamide (orange) and Cob(I)inamide (purple). Inset (b) depicts difference in absorption seen between (a). Increased intensity observed at lower wavelengths (250-300 nm) is from the addition of Ti(III) citrate.

2.2.5 EPR Spectroscopy of ACS

All continuous wave (CW) EPR spectra were collected at X-band (~9.3 GHz) on a Bruker (Billerica, MA) EMX spectrometer equipped with a Bruker/ColdEdge closed-cycle helium-compression cryostat and recirculating system and a MercuryiTC temperature and helium-flow controller. Table 2.1 lists the ACS samples used in EPR. All ACS EPR samples were prepared to a final concentration of either 100 or 200 µM and volume of 200 µL, unless otherwise noted. Methylated ACS EPR samples were prepared, stored, and their spectra collected all in darkness unless otherwise noted. All EPR spectra associated with the fast relaxing [Fe_4S_4] were at collected at 12-14K, and all spectra associated with the slower relaxing Ni and Co were noted in respective figures. EPR spectra were acquired and analyzed using WinEPR software from Bruker (Billerica, MA).

Sample	Isotope ($I = n/2$)	Ti(III) EQ	Expected Effect†	Used In…
CH_3-ACS	--	0.5x, 1.5x, 3x	--	Both
CH_3-^{57}Fe-ACS	^{57}Fe ($I = 1/2$)	0.5x, 1.5x	Broadening	Both
CH_3-^{61}Ni-ACS	^{61}Ni ($I = 3/2$)	0.5x	Broadening	Both
$^{13}CH_3$-ACS	^{13}C ($I = 1/2$)	0.5x	Broadening	ENDOR
CD_3-ACS	^{2}H ($I = 1$)	0.5x	Collapsing	Both
$^{13}CD_3$-ACS	^{13}C ($I = 1/2$), ^{2}H ($I = 1$)	0.5x	Broadening/Splitting	ENDOR

Table 2.1 Isotopic EPR and ENDOR samples of the methylated ACS.
†Expected effects are based on hyperfine interactions of nuclear effects.

2.2.6 Preparation of Mössbauer Spectroscopy Samples

^{57}Fe-labeled ACS samples were prepared to 250 μM (1 mM ^{57}Fe) for Mössbauer spectroscopy for the conditions listed in Table 2.2. All methylated samples use 1 equivalent of methyl-cobinamide relative to ACS. CO treatments were performed by purging headspace of the ACS sample in crimped and sealed brown glass vials for 25 minutes. Mössbauer cups were placed inside glass vials, stoppered and crimped, then flash frozen in liquid nitrogen. The samples were shipped to the Yisong "Alex" Guo lab at Carnegie Mellon University (Pittsburgh, PA).

Identifier	Condition	Ti(III) (eq)	[ACS] (μM)*	Notes
SRSW01	Untreated	--	263 (± 6)	
SRSW02	1.5x Reduced	1.5x	260 (± 10)	
SRSW03	CO-treated	1.5x	263 (± 8)	CO treatment; 20% spin
SRSW04	Methylated	1.5x	255 (± 6)	~ 74% converted
SRSW05	Acetylated	1.5x	251 (± 7)	SRSW04 + CO treatment
SRSW06	10x Reduced	10x	223 (± 4)	
SRSW07	Super Methylated	10x	240 (± 10)	~ 81% converted
SRSW08	Half Reduced	0.5x	105 (± 3)	*Unused*
SRSW09	Half Methylated	0.5x	262 (± 5)	*Unused*; ≤ 22% converted

Table 2.2 ^{57}Fe-ACS samples prepared for Mössbauer analysis.
*[ACS] calculated using Rose Bengal colorimetric assay[42]

2.2.7 Preparation of Samples for ENDOR Spectroscopy

Q-band (~35 GHz) ENDOR samples were prepared similar to EPR samples (Table 2.1), but in quartz Q-band tubes to a volume of 80 µL and ACS concentration of 300 µM. ACS samples were prepared by reducing labeled and unlabeled ACS to a final concentration of 300 µM with either 0.5 or 1.5 equivalents of Ti(III) citrate. Once reduced, ACS was methylated with 1 equivalent of labeled or unlabeled methyl-cobinamide. Q-band sample tubes were placed in X-band EPR tubes and capped with a rubber septum before they were flash frozen and stored in liquid nitrogen. Frozen samples were shipped to the Brian Hoffman lab at Northwestern University (Evanston, IL).

2.2.8 Preparation of Methylated X-ray Absorption Spectroscopy Samples

Methylated ACS samples were reduced with 3 molar equivalents of Ti(III) citrate and methylated for with 2.5 molar equivalents of methyl-cobinamide in 50 mM potassium phosphate pH 7.5 buffer with 30% glycerol. Immediately after the methylation reaction, the ACS samples were concentrated to 750 µM with 30 kDa-cutoff centrifugal filters, transferred to the XAS sample cell, and flash frozen in liquid nitrogen where stored at -80˚C until spectral acquisition. Samples were sent to Ritimukta Sarangi at the Stanford Linear Accelerator Center (SLAC) National Accelerator Laboratory (Menlo Park, CA).

2.2.9 Preparation of Methylated and Acetylated ACS for Mass Spectrometry

Reduced, methylated, and acetylated ACS samples were prepared for post-translational (PTM) mass spectrometry. The reduced ACS sample was 10 µM ACS reduced with 3 equivalents of Ti(III) citrate. The methylated ACS sample was reduced with 3 equivalents of Ti(III) citrate and methylated with 1 equivalent methyl-cobinamide. The acetylated ACS sample was prepared directly from the methylated sample and was subjected to CO treatment for 20 minutes in a stoppered and crimped vial. SDS-PAGE was performed on the ACS samples and resultant gel bands at 82 kDa associated with ACS were excised and submitted to the University of Michigan Proteomics Core. At the Core, the excised bands were reduced with DTT, alkylated with iodoacetamide, and trypsin digested at 37˚C overnight before peptides were extracted and analyzed using LC/MS/MS on an Orbitrap Velos mass spectrometer. Mass spectrometry data was analyzed using Scaffold4 from Proteome Software (Portland, OR).

2.3 Results and Discussion

2.3.1 Synthesis of Unlabeled and Labeled Methyl-Cob(III)inamide Reagents

Reacting Cob(II)inamide with Ti(III) citrate and MeI leads to complete conversion of the starting material to methyl-Cob(III)inamide. UV-visible analysis of the fractions collected during purification indicate excess Ti(III) citrate elutes quickly, populating a significant portion of the early fractions, with MeCbi eluting at the end of the Ti(III) citrate elution and well into the "middle" fraction, ~F7-F10 (Figure 2.4). An unknown contaminant, perhaps residual Ti(III) citrate, repeatedly emerged in later fractions manifesting as an absorbance increase ~ 210 nm.

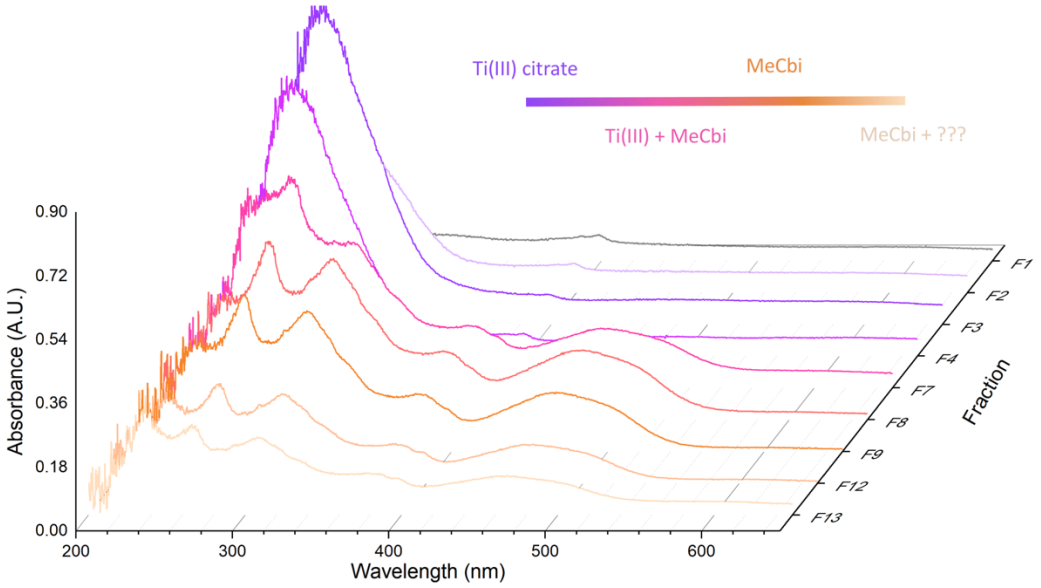

Figure 2.4 Representative figure of a typical purification of MeCbi reaction. Spectra are of diluted fractions to keep spectral absorbance below 1.0 (~1/40th to 1/160th). Fractions F5, F6, F10, and F11 were omitted for clarity and brevity. Excess Ti(III) citrate can be seen in early fractions and an unknown contaminant can be seen at ~210 nm accumulating in late fractions.

NA-MeCbi, $^{13}CH_3$-Cbi, CD_3-Cbi, and $^{13}CD_3$-Cbi were synthesized with their respectively labeled MeI, purified, and the resultant pooled MeCbi are listed in Figure 2.5. Final concentrations of the MeCbi reagents were calculated using ε_{470} = 10.8 mM^{-1} cm^{-1} and found to be 1.41 mM (MeCbi), 6.1 mM (^{13}C-MeCbi), 5.2 mM (D_3-MeCbi), and 5.8 mM ($^{13}CD_3$-MeCbi).

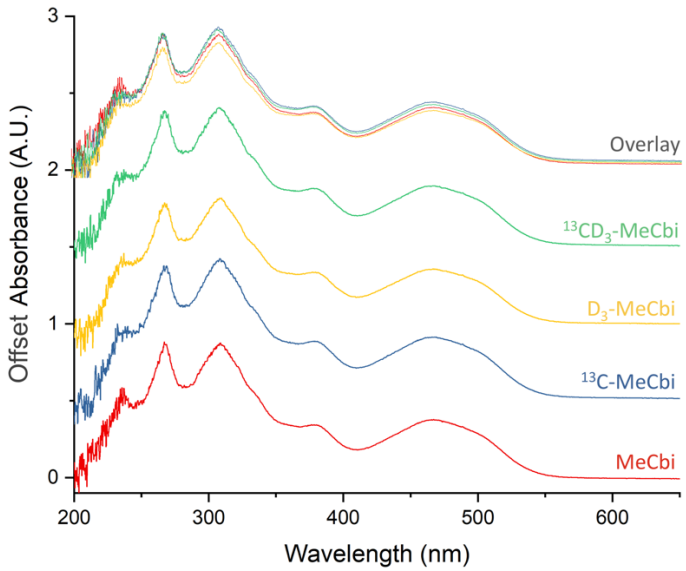

Figure 2.5 UV-visible spectra of the final pooled MeCbi isotopomers. Spectra are overlaid to show similarity, as well as shown individually for clarity. Unlabeled MeCbi pool is diluted by 1/40th, all other labeled pools were diluted by 1/160th.

2.3.2 Production of ^{57}Fe- and ^{61}Ni-Labeled ACS

Isotopically labeled Fe and Ni were sufficiently incorporated into ACS, with no obvious impact on metal loading or on carbonylation activity when compared to natural abundance (NA) ACS. Spectral broadening consistent with non-integer nuclear spin interactions seen previously[9] were observed via EPR for the NiFeC signal in both ^{57}Fe-ACS-CO and ^{61}Ni-ACS-CO (Figure 2.6). ICP-OES results on proper metal loading indicate replete A-clusters are present in the two labeled ACS proteins, and further validation of isotopically-homogenous ^{61}Ni incorporation, listed in Table 2.3.

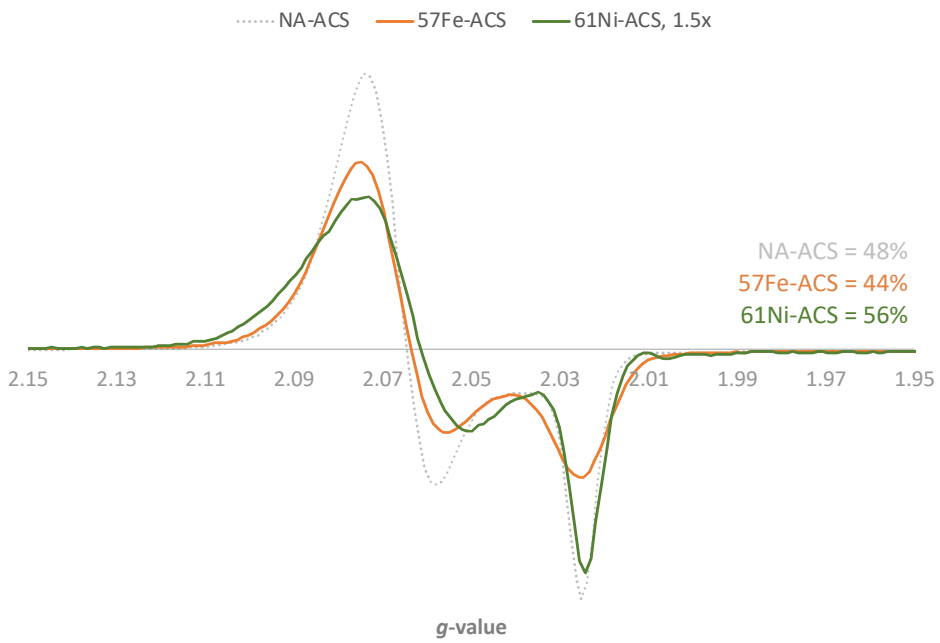

Figure 2.6 ^{57}Fe- and ^{61}Ni-ACS-CO EPR spectra at 100K compared to NA-ACS. Spin percentages for ^{57}Fe- and ^{61}Ni-ACS-CO are 44% and 56%, respectively. ^{61}Ni-ACS-CO intensity is magnified by 1.5x for better visual comparison. NA-ACS-CO parameters: power of 2.08 mW; modulation amplitude of 10G; gain of 5.023×10^3; frequency of 9.3844 GHz. ^{57}Fe-ACS-CO parameters: power of 2.08 mW; modulation amplitude of 10G; gain of 5.024×10^3; frequency of 9.3818 GHz. ^{61}Ni-ACS-CO parameters: power of 2.08 mW; modulation amplitude of 10G; gain of 5.023×10^3; frequency of 9.3805 GHz.

ICP-OES Metal Content (n = 3)	Fe (*of 4*)	Ni (*of 2*)	Zn (*of 0*)
^{57}Fe-ACS Pre-Reconstitution	2.9 (± 0.2)	0.11 (± 0.01)	0.22 (± 0.01)
^{57}Fe-ACS Reconstituted	3.2 (± 0.8)	1.62 (± 0.05)	0.14 (± 0.05)
^{61}Ni-ACS Pre-Reconstitution	2.3 (± 0.1)	0.07 (± 0.01)	0.34 (± 0.01)
^{61}Ni-ACS Reconstituted	2.69 (± 0.04)	2.84 (± 0.02)	0.21 (± 0.01)

Table 2.3 Pre- and post-reconstitution of isotopically labeled ACS. This table includes zinc as nonfunctioning nickel contaminant due to the observation of zinc in place of Ni_p[15,17].

2.3.3 UV-Visible Observation of ACS Methylation

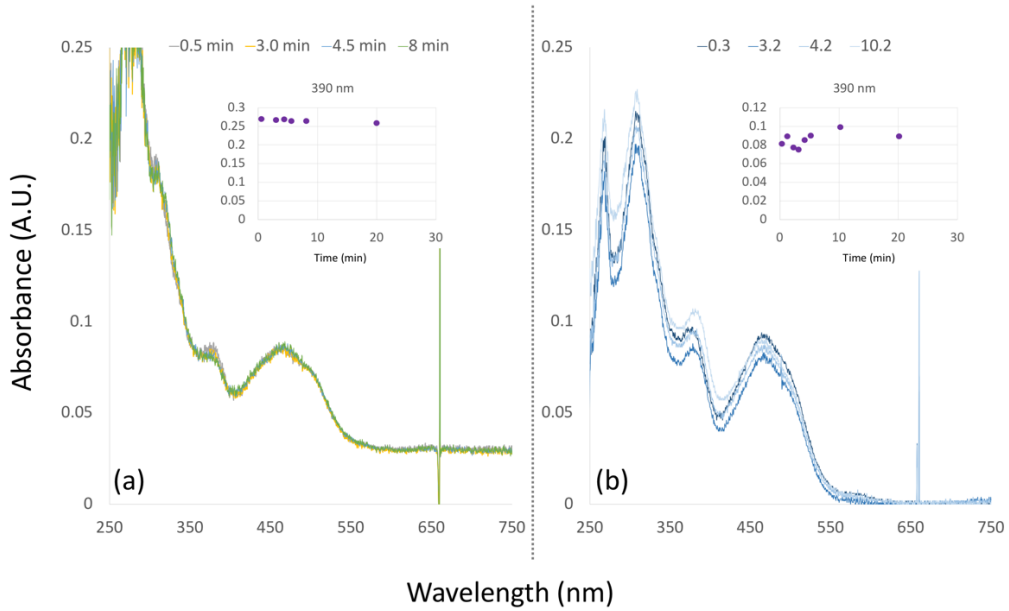

Figure 2.7 UV-visible data showing no reaction of unreduced ACS with MeCbi and MeCbi with 3x Ti(III) citrate. (a) Without Ti(III) citrate, ACS is unable to convert MeCbi over the course of 20 minutes (inset). (b) without ACS, no degradation of MeCbi by Ti(III) is observed over 20 minutes (inset). Additionally, no photodegradation is observed for either (a) or (b) during the reaction.

Without Ti(III) citrate, methyl transfer from MeCbi to ACS is not observed, nor is the conversion of MeCbi to Cob(I)inamide by Ti(III) citrate without ACS (Figure 2.7). Reacting ACS with MeCbi in slight excess of Ti(III) citrate results in a consistent, near-complete conversion (≥ 70% conversion) of MeCbi to Cob(I)inamide, and corroborates previous data indicating a 2-electron methylation-coupled oxidation of a nickel in the A-cluster[31-33]. Figure 2.8 shows the consistent conversion of MeCbi under various reducing conditions, and clearly depicts a reliance on the starting concentration Ti(III) citrate on the completion of the reaction. The use of substoichiometric (0.5 equivalent) of Ti(III) citrate showed a rapid jump in absorbance at 390 nm, indicating production of Cob(I)inamide, but quickly decayed to Cob(II)inamide and remained in the Cob(II)inamide state (Figure 2.8; (c)).

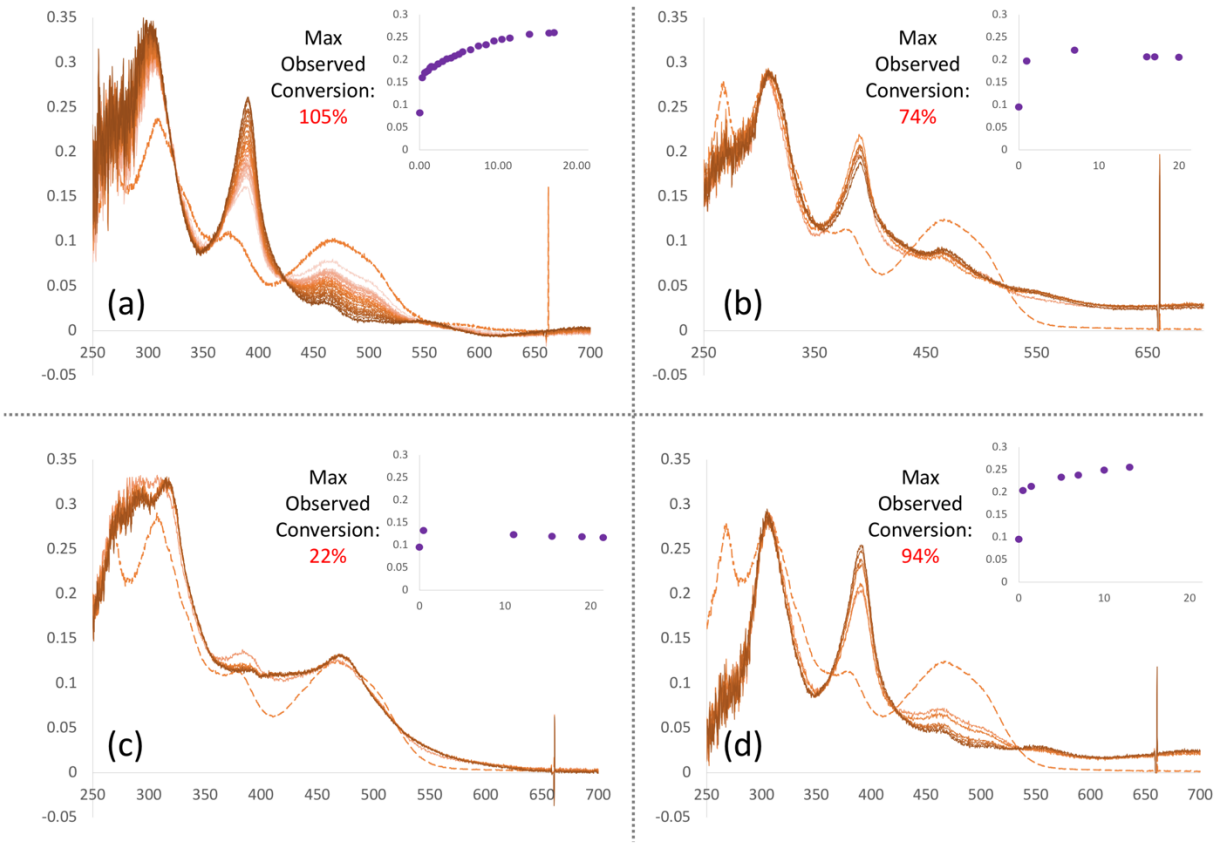

Figure 2.8 Representative UV-visible spectra of ACS methylation with 1 equivalent MeCbi under various reductant concentrations. Equivalents of Ti(III) citrate used in the above graphs depict (a) 3 equivalents, (b) 1.5 equivalent, (c) 0.5 equivalent, and (d) 10 equivalents. Spectra insets depict change at 390 nm over 20 minutes. Maximum methylation conversion values are listed in the respective section and are based on $\Delta\varepsilon_{390} = 17\ mM^{-1}\ cm^{-1}$. Spectra (b-d) are UV-visible data of samples prepared for Mössbauer spectroscopy.

2.3.4 EPR of the Superstoichiometrically Reduced (≥ 1:1 Ti(III):ACS) Methylated ACS

EPR was utilized to observe any potential paramagnetic species generated by the A-cluster [Fe_4S_4] after the methylation reaction observed with the conversion of MeCbi to Cob(I)inamide. Initial conditions were as used in UV-visible experiments but scaled to ~ 200 µM ACS and MeCbi with 3 equivalents of Ti(III) citrate. Spectra of the methylated ACS taken at 14K showed spectral broadening at g = 1.86 underneath the g = 1.92 feature assigned to residual Ti(III) citrate already seen in reduced ACS (Figure 2.9). The spin percentages of Ti(III) citrate, the reduced ACS, and the methylated ACS were 29%, 6%, and 42%, respectively, in comparison to a copper (II) perchlorate standard. The broad g = 1.86 feature appeared to increase the spin percentage by 15% relative to the Ti(III) citrate alone, and by 36% relative to the reduced ACS. Additionally, no EPR-

active Cob(II)inamide was observed, indicating methylation yields the EPR-silent Cob(I)inamide from the EPR-silent Cob(III)inamide, but the lack of observed Cob(II)inamide may also be due to excess equivalents of reductant re-establishing the Cob(I)inamide state from any Cob(II)inamide product. Assuming methylation occurs at the A-cluster Ni_p, it likely is oxidized from Ni_p(I) to Ni_p(III) and subsequently reduced with any remaining equivalents of Ti(III) citrate in solution.

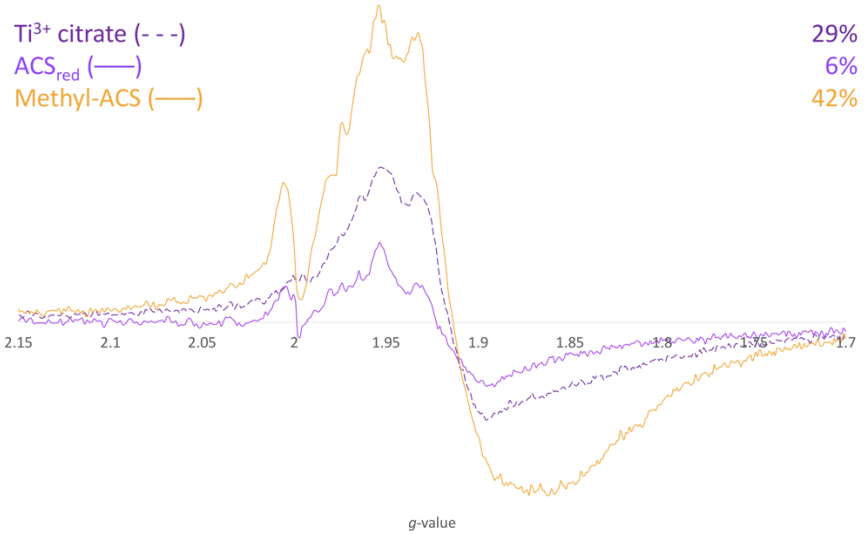

Figure 2.9 EPR spectra at 12K of Ti(III) citrate, reduced ACS, and methylated ACS. Unique g = 1.86 broadening can be seen for the methyl-ACS sample, but not for others. Spin percentages in comparison to a Cu(II) perchlorate standard are located at the top right corner. Ti(III) citrate parameters: power of 0.105 mW; modulation amplitude of 5G; gain of $4.048x10^3$; frequency of 9.3769 GHz. ACS_{red} parameters: power of 0.208 mW; modulation amplitude of 5G; gain of $4.48x10^3$; frequency of 9.3752 GHz. Methyl-ACS parameters: power of 0.208 mW; modulation amplitude of 5G; gain of $4.48x10^3$; frequency of 9.3795 GHz.

In taking EPR spectra of the Ti(III) citrate reduced ACS samples, an apparent light-sensitivity of Ti(III) citrate at liquid nitrogen temperatures by overhead fluorescent light-induced photooxidation was discovered (Figure 2.10). This photooxidation effect was used to remove the strongly overlapping Ti(III) citrate signal, all of the EPR samples were exposed to overhead light in liquid nitrogen for 5, 15, and 45 minutes to identify the potential spectral feature at ~1.85 for methylated ACS. Surprisingly, all of the samples showed a substantial decrease in signal intensity within 15 minutes, but unfortunately did not offer any further resolution to the identity of the methylated ACS's broad feature at g = 1.86. An interesting effect of light exposure showed a marked increase in spin percentage for the methylated and reduced ACS after 5 minutes (Figure

2.10; (a), (b)). The difference spectrum between the methylated and reduced ACS appears to have increased $g = 1.89$ character, although its shape is somewhat similar to Ti(III) citrate.

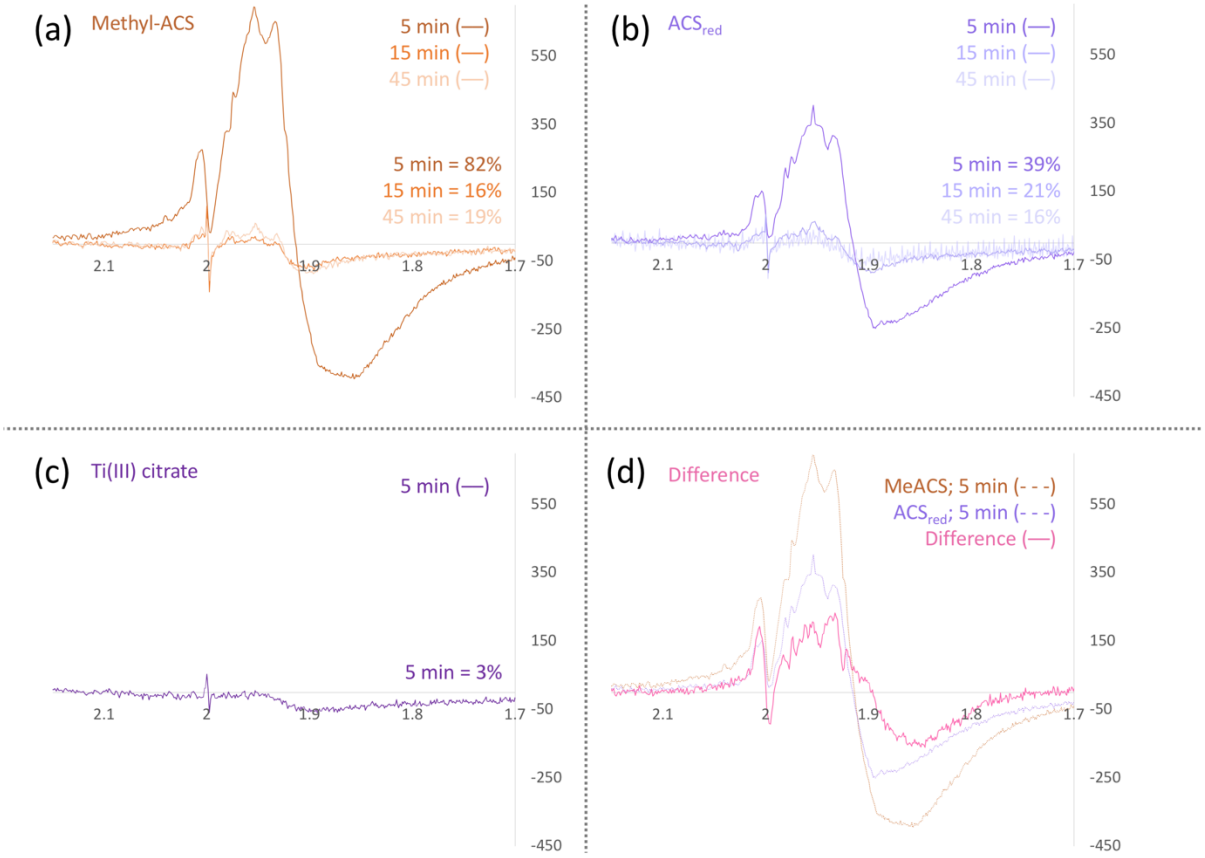

Figure 2.10 Effects of 5, 15, and 45 minutes of light on EPR samples seen in Figure 2.9 at 14K. (a) Methylated-ACS with light exposure. Signal appeared to increase at 5 minutes exposure but decreased substantially after 5 min. (b) Reduced ACS (ACS_{red}) with light exposure. Following the methylated ACS, ACS_{red} also appeared initially to increase in signal, decaying after 5 min. (c) Ti(III) citrate after 5 min of light exposure, but no signal is seen. (d) Difference spectrum between methylated and reduced ACS. Methyl-ACS, 5 min parameters: power of 0.208 mW; modulation amplitude of 5G; gain of 4.48×10^3; frequency of 9.3787 GHz. Methyl-ACS, 15 min parameters: power of 0.208 mW; modulation amplitude of 5G; gain of 4.48×10^3; frequency of 9.3728 GHz. Methyl-ACS, 45 min parameters: power of 0.208 mW; modulation amplitude of 5G; gain of 4.48×10^3; frequency of 9.3763 GHz. ACS_{red}, 5 min parameters: power of 0.208 mW; modulation amplitude of 5G; gain of 4.48×10^3; frequency of 9.3757 GHz. ACS_{red}, 15 min parameters: power of 0.208 mW; modulation amplitude of 5G; gain of 4.48×10^3; frequency of 9.3719 GHz. ACS_{red}, 45 min parameters: power of 0.191 mW; modulation amplitude of 5G; gain of 4.48×10^3; frequency of 9.3744 GHz. Ti(III) citrate parameters: power of 0.208 mW; modulation amplitude of 5G; gain of 4.048×10^3; frequency of 9.3728 GHz.

After illumination experiments did not resolve the $g = 1.86$ feature, PD10 desalting column (GE Healthcare; Chicago, IL) gel-filtration was performed on ACS to eliminate residual Ti(III) citrate reductant. UV-visible data showed a 96% conversion, and the resulting EPR spectrum revealed a strong and broad $g \sim 1.87$ feature with an overall spin percentage of 57% at 6K (Figure 2.11). At 95K, the broad signal diminished to 10% and appeared to downshift from 1.87 to $g \sim 1.9$, previously attributed to Ti(III) citrate. Compared to the methylated ACS under the superstoichiometric reducing conditions in Figure 2.9, these data offered the possibility of a paramagnetic fast-relaxing [Fe_4S_4] signal after methylation.

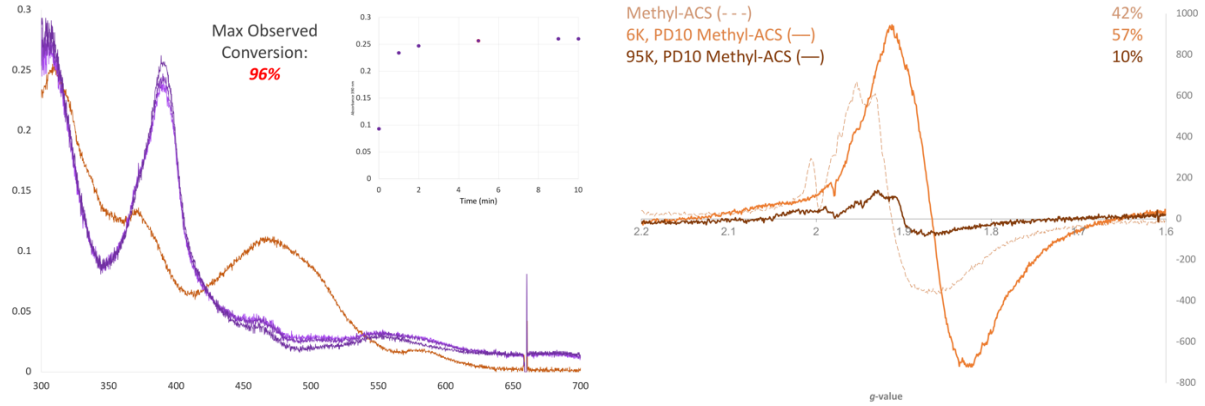

Figure 2.11 UV-visible monitoring and EPR spectra of PD10-filtered methylated ACS. (*Left*) UV-visible data showing near-complete methyl transfer to ACS. (*Right*) EPR data of PD10-filtered methyl-ACS compared to Figure 2.9. Strong, broad feature at $g \sim 1.87$ observed at 6K, but diminished and shifted to $g \sim 1.9$ at 95K. Methyl-ACS parameters: power of 0.208 mW; modulation amplitude of 5G; gain of 4.48×10^3; frequency of 9.3795 GHz. 6K, PD10 Methyl-ACS parameters: power of 20.51 mW; modulation amplitude of 5G; gain of 5.203×10^3; frequency of 9.2770 GHz. 95K, PD10 Methyl-ACS parameters: 20.51 mW; modulation amplitude of 5G; gain of 5.203×10^3; frequency of 9.2770 GHz.

In an attempt to unambiguously resolve the identity of the $g \sim 1.87$ feature observed in previous methyl-ACS spectra, ^{57}Fe-ACS was prepared for EPR spectroscopy. Interestingly, EPR data showed a downfield shift of roughly $\Delta g \approx 0.2$ apparent at the $g \sim 1.86$ to $g \sim 1.84$ while maintaining the upfield values at $g \sim 1.95$ and $g \sim 1.92$ (Figure 2.12). This shift is consistent with ^{57}Fe-coupling paramagnetic [Fe_4S_4] cluster in ACS after methylation but it does not offer enough resolution to be conclusive.

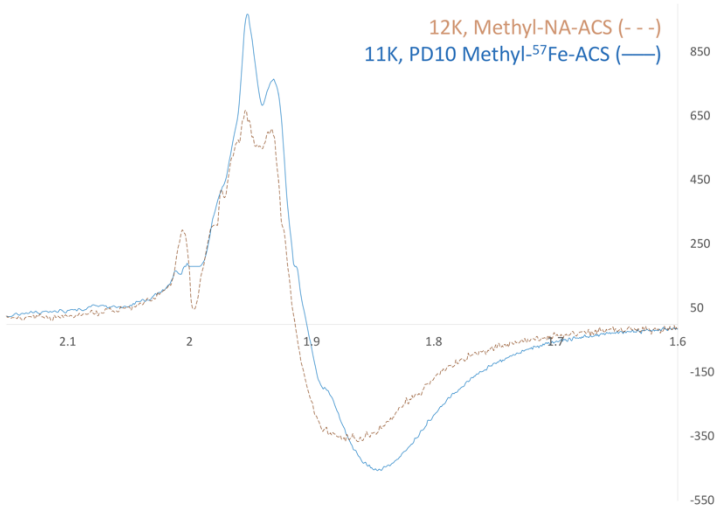

Figure 2.12 Comparison of methylated ^{57}Fe-ACS and NA-ACS EPR spectra. Methyl-^{57}Fe-ACS is at 0.5x intensity for spectral overlay of methyl-NA-ACS. Downfield shifts from $g \sim 1.86$ to $g \sim 1.84$ are seen in ^{57}Fe-ACS in comparison to NA-ACS. Methyl-ACS parameters: power of 0.208 mW; modulation amplitude of 5G; gain of 4.48×10^3; frequency of 9.3795 GHz. Methyl-^{57}Fe-ACS parameters: power of 0.207 mW; modulation amplitude of 10G; gain of 5.02×10^3; frequency of 9.3830 GHz.

2.3.5 EPR of the Substoichiometrically Reduced (50% Ti(III):ACS) Methylated ACS

In the event that the slight excess Ti(III) citrate reductant was rapidly reducing any oxidized A-cluster Ni(III) or $[Fe_4S_4]$(III) signal, we prepared "substoichiometric" reducing conditions where the starting Ti(III) citrate concentration was limited to 50% of the ACS concentration. Under substoichiometric conditions, EPR data indicated a complicated mixture of paramagnetic signals, with a decrease in residual Ti(III) citrate at $g = 1.92$ and the emergence of an EPR-active "base-on" Cob(II)inamide signal at $g = 2.24$[43] (Figure 2.13 (b-d)). The oxidation of the Cob(I)inamide to Cob(II)inamide was also observed via subtle UV-visible changes (Figure 2.8, (c)).

While the predominant signal at $g = 2.24$ was attributed to Cob(II)inamide, an interesting feature consistent with a square-planar Ni(III) reproducibly arose at $g = 2.55$ with methylated ACS samples. In order to confirm the identity of the $g = 2.55$ feature we prepared ^{61}Ni-ACS and labeled MeCbi isotopomers, since this feature may also reflect a base-off Cob(II)inamide, which we observe in UV-visible spectra[43]. Figure 2.13 shows the various EPR spectra of the labeled ACS and MeCbi, where the samples did not generate any significant isotopic shifts associated with an obvious paramagnetic A-cluster. Based on the lack of observed isotopic broadening in the methyl-

^{61}Ni-ACS sample and in comparison with the dithiothreitol-reduced Cob(II)inamide sample, the *g* = 2.55 was hypothesized to stem from residual base-off Cob(II)inamide produced after the methyl transfer reaction.

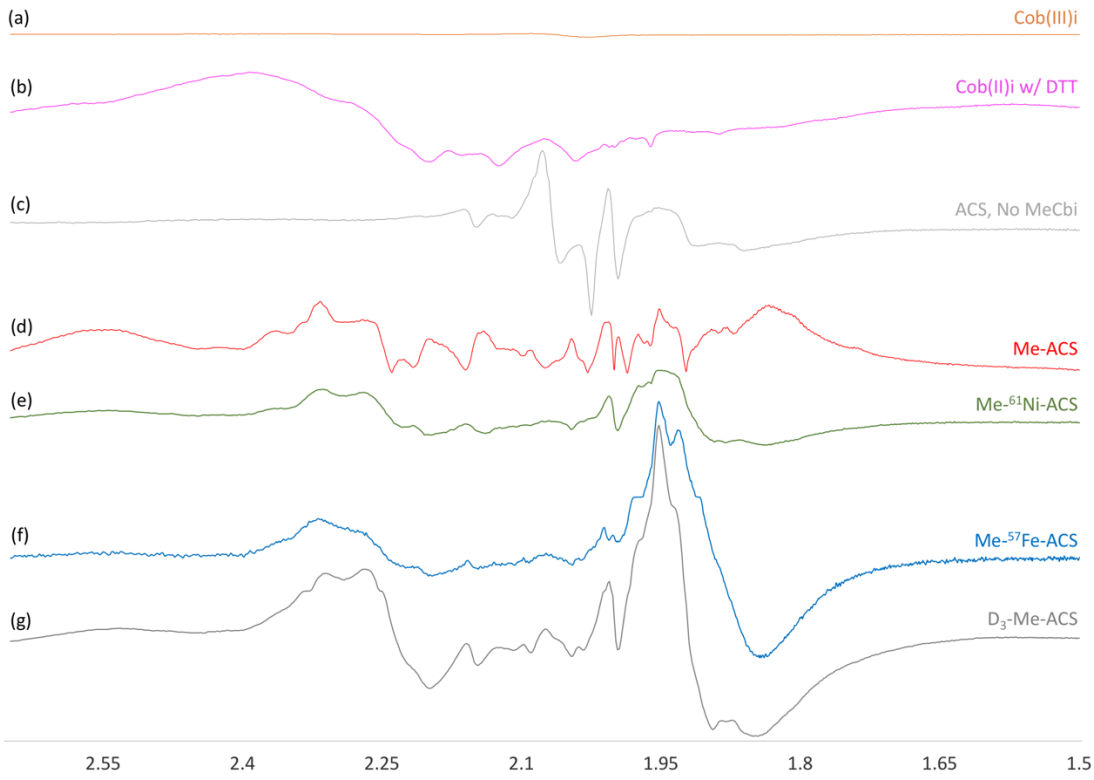

Figure 2.13 Isotopic effects on 12K methylated ACS EPR relative to NA-Me-ACS and cobinamide. (a,b) Spectra of EPR-silent Cob(III)inamide and EPR-active Cob(II)inamide, reduced with excess dithiothreitol (DTT). (c) Spectrum of unmethylated ACS. (d) Methylated ACS. (e,f) Isotopically-labeled ^{61}Ni- and ^{57}Fe-methyl-ACS. (g) Isotopically labeled D_3-Me-ACS. Cob(III)i parameters: power of 0.658 mW; modulation amplitude of 10G; gain of $4.48x10^3$; frequency of 9.3788 GHz. Cob(II)i w/ DTT parameters: power of 0.658 mW; modulation amplitude of 10G; gain of $4.48x10^3$; frequency of 9.3738 GHz. ACS, No MeCbi parameters: power of 0.651 mW; modulation amplitude of 10G; gain of $4.48x10^3$; frequency of 9.3816 GHz. MeACS parameters: power of 0.647 mW; modulation amplitude of 10G; gain of $4.48x10^3$; frequency of 9.3839 GHz. Me-^{61}Ni-ACS parameters: power of 0.651 mW; modulation amplitude of 10G; gain of $4.48x10^3$; frequency of 9.3832 GHz. Me-^{57}Fe-ACS parameters: power of 0.207 mW; modulation amplitude of 10G; gain of $5.023x10^3$; frequency of 9.3850 GHz. D_3-Me-ACS parameters: power of 0.658 mW; modulation amplitude of 10G; gain of $4.48x10^3$; frequency of 9.3836 GHz.

2.3.6 Confirming the Diamagnetic Methyl- and Acetyl-ACS by Mössbauer & ENDOR

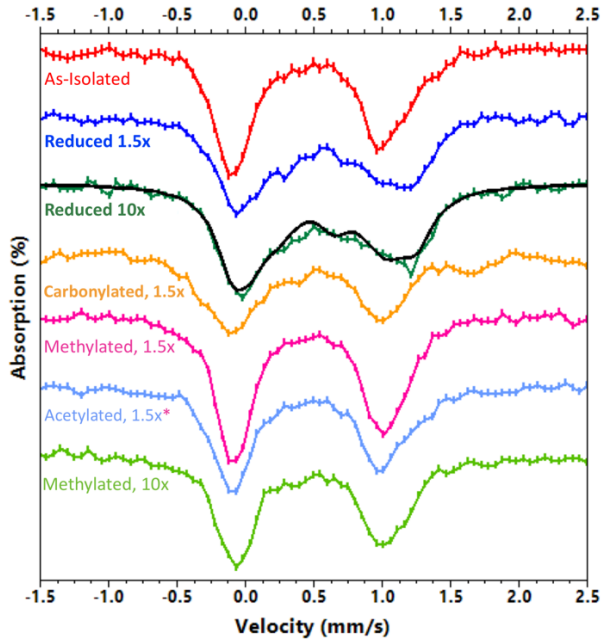

Figure 2.14 Mössbauer spectroscopy of substrate-bound ACS. Methylated (1.5x and 10x) and Acetylated samples appeared identical to the As-isolated sample. Reduced (1.5x and 10x) and Carbonylated ACS samples had changes indicative of [Fe_4S_4] reduction. *Acetylated ACS was prepared directly from the Methylated sample. Data acquired and figure provided by Dr. Jin Xiong.

To remove any doubt about the source of any underlying A-cluster signals, we employed Mössbauer and ENDOR spectroscopies to confirm the EPR silence of the A-cluster. Both Mössbauer and ENDOR failed to observe significant changes associated with the [Fe_4S_4] upon methylation. Mössbauer indicated the methylated and acetylated ACS samples were identical to the diamagnetic as-isolated ACS, with the only spectral differences seen in the reduced and carbonylated samples (Figure 2.14). For the carbonylated sample, spectral features flanking the prominent quadrupole doublets reduced samples indicate some slight [Fe_4S_4](I), but for the reduced samples, both achieved only 30% of a shift to [Fe_4S_4](I) for the total Fe. ENDOR data reinforces the lack of [Fe_4S_4](I) signal, proving no paramagnetic signal is associated with the ACS A-cluster [Fe_4S_4] after methylation (Figure 2.15). Additionally, ENDOR confirmed no underlying isotopic dependence on ^{61}Ni-ACS in the $g = 2.24$ region after methylation.

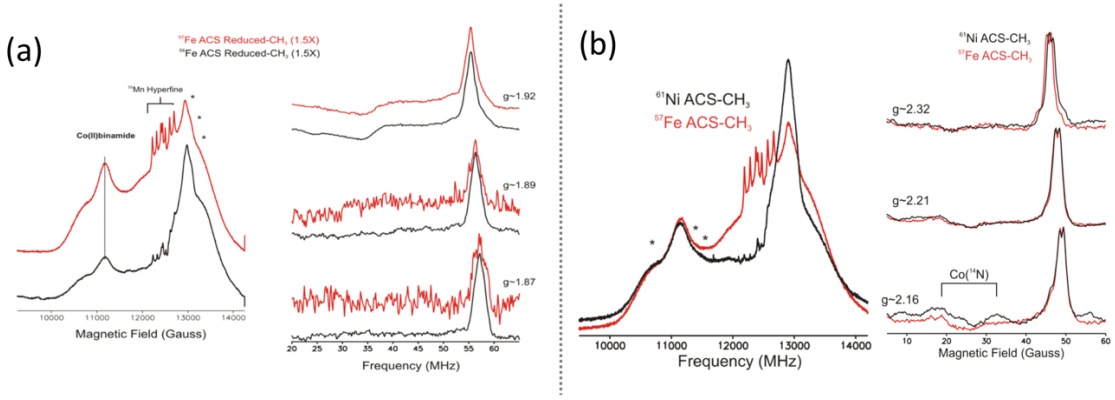

Figure 2.15 ENDOR spectroscopy of ^{57}Fe- and ^{61}Ni-ACS after methylation. Paramagnetic signals seen in the methylated-ACS did not reveal nor contain any underlying A-cluster signals. (a) ^{57}Fe-ACS did not show any underlying isotopic iron dependence in the expected $g = 1.90$ region for an [Fe_4S_4] cluster. (b) ^{61}Ni-ACS did not show any underlying isotopic dependence on the $g = 2.24$ region. Data acquired and figures provided by Dr. Chris D. James.

Further confirmation of the A-cluster's silence was provided by isotopically labeled methyl-isotopomers including $^{13}CH_3$-MeCbi, D_3-MeCbi, and $^{13}CD_3$-MeCbi. showing absolutely no coupling of the methyl group in any paramagnetic signal (Figure 2.16). ^{15}N hyperfine splitting was observed in all samples, and is likely associated with the effect of the corrin ring from the Co(II)binamide signal.

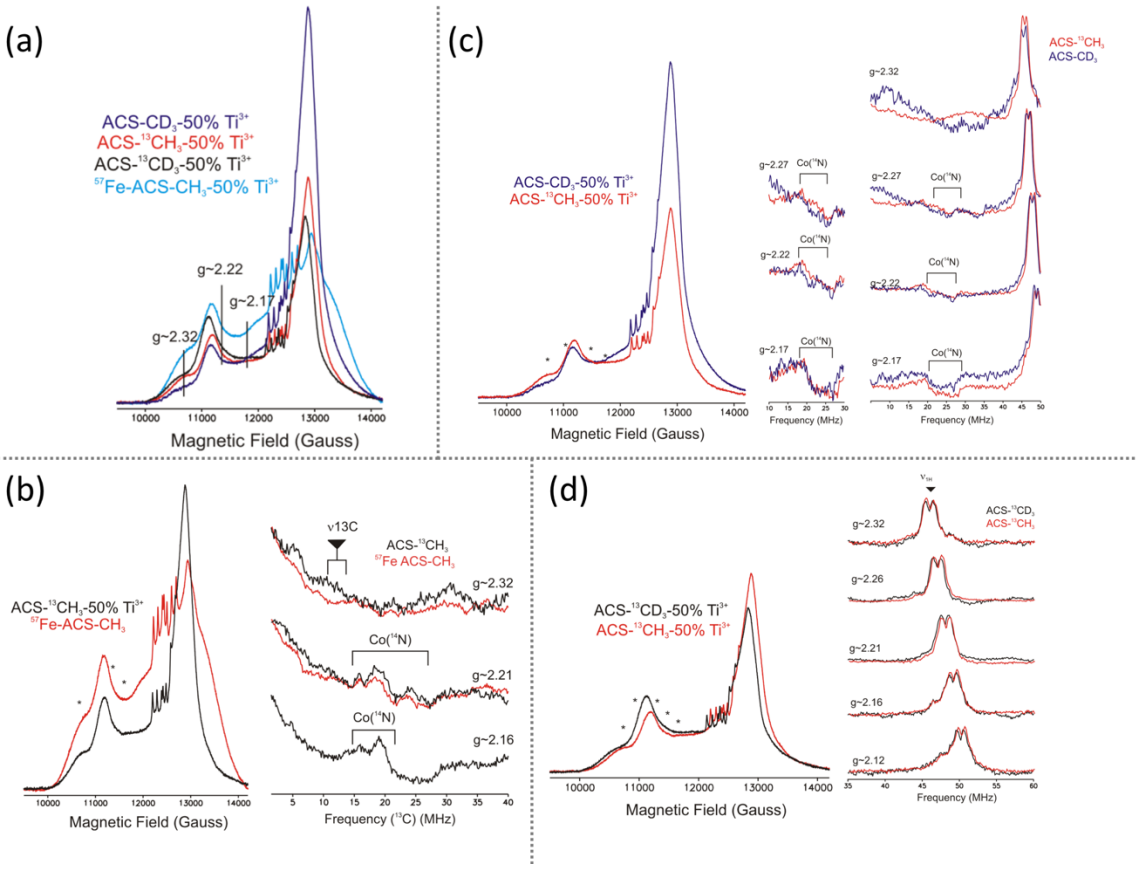

Figure 2.16 Labeled methyl isotopomers provide further confirmation a methyl group is not involved in any of the paramagnetic signals. (a) Overlap of absorption spectra for the various methyl-isotopomers under substoichiometric conditions in comparison to NA-MeCbi from ^{57}Fe-ACS. (b) Comparison of ^{13}C-methyl-ACS to NA-methyl-^{57}Fe-ACS. No significant ^{13}C coupling is seen between the samples. (c) Comparison of D_3-methyl-ACS to $^{13}CH_3$-methyl-ACS. No significant ^{1}H coupling is seen between the samples. (d) Comparison of $^{13}CD_3$-methyl-ACS to $^{13}CH_3$-methyl-ACS. No significant ^{1}H coupling is seen between samples. Data acquired and figures provided by Dr. Chris D. James.

2.3.7 XAS Confirmation of the Methyl-ACS

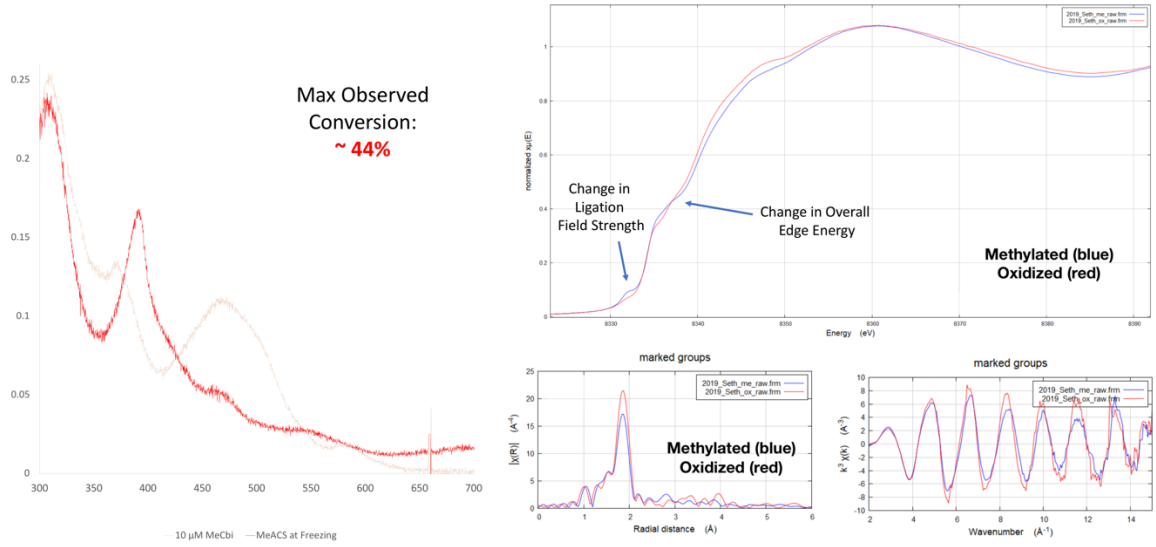

Figure 2.17 UV-visible observation and Ni K-edge analysis of methylated ACS. (*Left*) UV-visible observation of methylated ACS sample at freezing, at roughly 44% conversion. (*Right*) XAS data of the Ni K-edge showing changes at the pre-edge and rising edge. Data acquired and figure provided by Dr. Ritimukta Sarangi.

Since EPR was not able to unambiguously resolve the location of methyl binding in ACS, XAS was employed to resolve whether ligand field and redox changes occur for the ACS Ni_p upon methylation. For the XAS samples, reduced ACS methylated to a conversion of 44% (Figure 2.17; *left*). XAS data indicated subtle pre-edge and rising edge changes consistent with no change in nickel geometry, but rather with a ligand shift in one of the A-cluster nickels after methylation (Figure 2.17; *right*).

2.3.8 Methylated Cysteine Mass Spectrometry

In lieu of any evidence of an EPR-active A-cluster, we turned to mass spectrometry to resolve if any off-target methylation was occurring on any one of the 10 cysteines in ACS. Samples of unreacted, methylated, and acetylated ACS were compared in triplicate to understand if methylation was occurring in an off-target fashion, and if carbonylation could cause methyl migration from any of these methylated cysteines. Methylation was observed to a maximal conversion of ~72% via UV-visible spectrometry, and ACS-containing SDS-PAGE gel bands at ~80 kDa were excised (Figure 2.18).

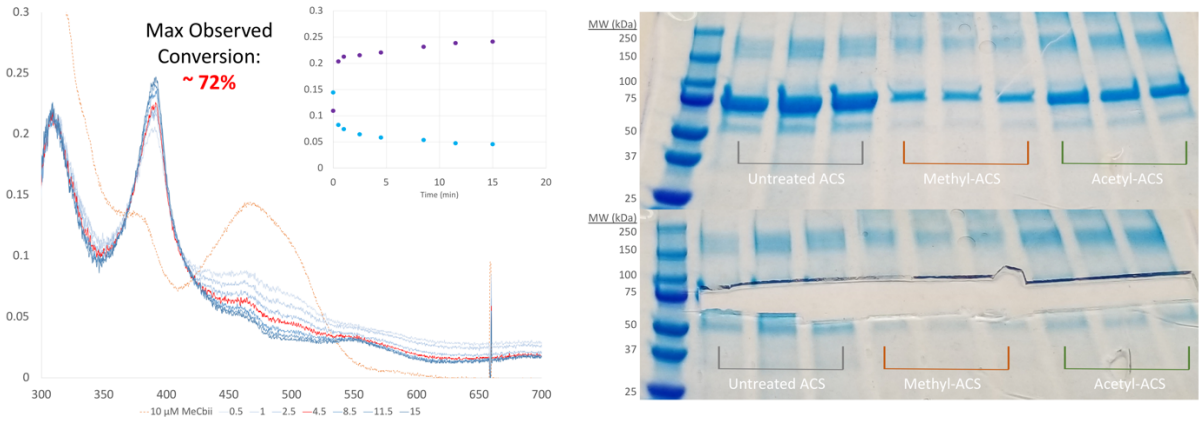

Figure 2.18 Validation of methylated and acetylated ACS for MS analysis. (*Left*) UV-visible observation of ACS methylation, showing an overall methylation conversion of 72%, with the red highlight representing the time of CO purge and sample denaturation. (*Right*) SDS-PAGE gel and excised bands submitted for MS analysis.

In conjunction with the 72% methylation observed in Figure 2.18, no cysteine in ACS appeared to play a mechanistic role in methylation or was converted to an acetyl-cysteine after 10 minutes of CO treatment as observed via mass spectrometry. Figure 2.19 depicts the methylation (*top*) and acetylation (*bottom*) profiles of the 10 cysteines present in ACS for each treatment, all fitting within error of one another, with exception of C67 in the methylation profile and C509 in the acetylation profile. C67 and C509 both show differences relative to other treatments. C67 appears to have a small increase in methylation relative to the acetylated and untreated samples. After both methylation and CO-treatment C509 appears to have a significant decrease in acetylation relative to the untreated sample. In total, the average percentage of modification was around 6% and varied among cysteine identity, with no single observed cysteine modification greater than 36%, indicating any cysteine modification represents a true minority species. Compared to the untreated sample, the methylated and acetylated ACS showed no trends after treatment and did not alter the cysteine profile, implying an ACS cysteine is not the primary methylation site, nor is there any significant off-target methylation occurring.

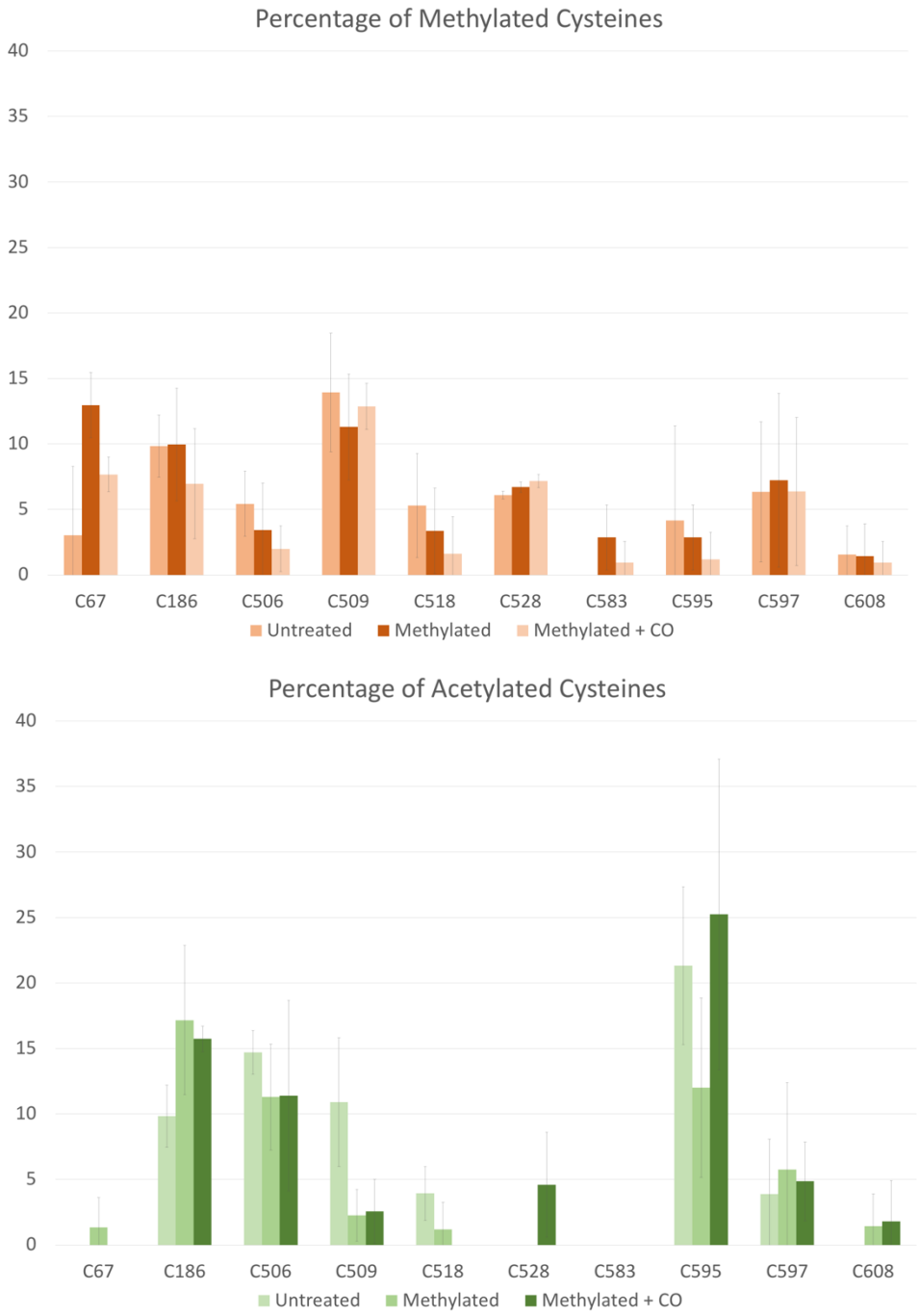

Figure 2.19 Mass spectrometry data showing methyl and acetyl cysteine modification percentages of the untreated, methylated, and acetylated ACS samples. (*Top*) Profile of methylated cysteines for all ACS conditions, showing no significant cysteine methylation for the MeCbi treated ACS relative to untreated with exception of C67. (*Bottom*) Profile of acetylated cysteines for all ACS conditions, showing no significant cysteine acetylation after methylation and CO treatment, with exception of C509. Error bars are based on standard deviation of triplicate samples. Darker colors represent the bar expected to increase assuming the cysteine played a mechanistic role in ACS.

2.4 Discussion

2.4.1 UV-Visible Spectrometry Monitors Methylation of ACS

UV-visible spectrophotometry has long been used to observe the decay of methyl-CFesP when transferring the methyl group to ACS[17,30,31]. The methylation reaction has been long hypothesized as an organometallic transfer methyl between Co(III) and Ni_p based on the reaction equilibrium favoring ACS by 2-fold[31] and the requirement for low-potential reductants such as Ti(III) citrate[17,29,32]. The dependence on such low-potentials implies the ACS must undergo a single-electron reduction, or perhaps as with CO binding, a chemically coupled reaction[10]. This lack of MeCbi conversion observed with ACS in the absence of Ti(III) strongly implies a reduced metal capable of accepting a methyl cation is necessary for the reaction to proceed.

Further support for the rapidly-decaying Ni_p(III) intermediate is evidenced by the emergence of Co(II)binamide after methylation in substoichiometric reducing conditions. This rapid, near concerted formation of Cob(II)inamide may indicate the presence of a strongly oxidizing species in the A-cluster taking an electron from the highly-reducing Co(I)binamide produced in methyl-transfer. Further experiments involving rapid-freeze quench are required to elucidate the exact nature of this phenomenon.

Alternatively, another possible EPR-silent mechanism may be explained by a methyl cation transfer to an ACS A-cluster cysteine but is unlikely due to the reductant requirement[35]. Pezacka in 1988 hypothesized ACS cysteine methylation as the catalytically relevant mechanism and showed retention of radiolabeled methyl groups on ACS after treatment with ^{14}C-methyl donors such as MeI and CFeSP. While a possibility, this hypothetical mechanism has not had much support over the years since, even with catalytically-relevant methylation by CFeSP[34,35].

2.4.2 The ACS A-Cluster State is Diamagnetic After Methylation

The A-cluster invariably appears EPR-silent after methylation, implying it remains diamagnetic in the methylated state. While the $g \sim 1.86$ feature seen at low-temperature was initially thought to stem from an oxidized [Fe_4S_4] cluster compensating for nickel oxidation during methylation, no isotopic effects were observed linking it to the A-cluster. The differences between Ti(III) citrate alone, Ti(III) citrate with ACS, and the methylated ACS appeared significant but the exact nature of why these differences are distinct is still unknown and unresolved.

The discovery of the Ti(III) citrate light sensitivity while fortunate, did little to resolve the paramagnetic signals seen in the ACS samples. While the $g \sim 1.86$ feature remained 5 minutes post-illumination, 15 minutes of illumination erased the paramagnetic signal. The increase in signal intensity at 5 minutes post-illumination of the methyl-ACS could be due to photoreduction of the A-cluster[44,45], but this remains to be confirmed, and other data in this work provides evidence to the contrary. Manesis et al. recently indicated a methyl-Ni(III) bond mimicking the ACS A-cluster was also sensitive to photolysis, which could explain the disappearance of the $g \sim 1.86$ feature[46]. Experiments probing the photolytic sensitivity of the methylated ACS have been planned. While EPR experiments of the methylated ^{57}Fe-ACS showed changes in the downfield *g*-values, any definite resolution likely stemmed from minor differences in temperature and/or Ti(III) concentration, especially when considering all other data within this work.

Mössbauer and ENDOR experiments conclusively disproved any [Fe_4S_4] changes after methylation, showing no paramagnetic state in ENDOR or a change from the as-isolated state in Mössbauer. Interestingly, Mössbauer spectroscopy indicated subtle [Fe_4S_4] changes upon exposure to ≥ 1.5x Ti(III) citrate reductant, as well as when ACS is exposed to CO, forming the carbonylated species. The 30% reduced Fe seen in reduced Mössbauer samples is the same for both the 1.5x and 10x Ti(III) citrate conditions, and indicates the change in iron may reflect an incomplete A-cluster, seen previously[17,31,36].

X-ray absorption spectroscopy revealed significant changes to the Ni K-edge upon methylation from the as-isolated state, supporting the hypothesis that ACS methylation occurs specifically on the Ni_p within the A-cluster. The XAS changes support a methyl-bound square planar Ni(II), as the changes in the pre-edge and rising edge are consistent with an increased ligand strength that is attributed to the methyl group[47].

Altogether, the spectroscopic evidence overwhelmingly supports a diamagnetic A-cluster after methyl transfer, which occurs on the Ni_p of the A-cluster. This methyl transfer creates a highly oxidizing methyl-Ni(III) intermediate2 that rapidly reduces to a diamagnetic methyl-Ni(II). The methyl-Ni(III) intermediate is considered to be very short-lived, converting to the methyl-Ni(II) well within the timeline of the experiments presented in this work. Future rapid freeze-quench experiments probing the possibility of the methyl-Ni(III) intermediate have been planned.

2.4.3 Mass Spectrometry of Methyl- and Acetyl-ACS Rebut Methyl-Cysteine Mechanism

MS experiments on ACS have shown no evidence of any mechanistically-relevant methyl-cysteines immediately near the ACS A-cluster capable of migrating in the presence of CO. While there is an overall baseline percentage of methylated and acetylated cysteines, the lack of any distinct pattern or trend with respect to methylation or acetylation contradicts the idea that the A-cluster cysteines are a viable mechanistic route for ACS[35]. The low percentage of cysteine modification observed may be due to a small amount of residual non-replete A-cluster, leading to modified cysteines in the A-cluster area, but do not fully account for the cysteines distant to the A-cluster. Ruling out cysteine methylation as a viable mechanistic route in ACS, the mass spectrometry results imply any methylation observed via UV-visible spectroscopy is occurring on the A-cluster Ni_p. The decrease in C509 acetylation is noteworthy considering it is the A-cluster's bridging cysteine, but as there are no changes in C509 methylation, this difference is unlikely to reflect a real phenomenon. The methylation of C67 is also unlikely to be mechanistically relevant, as it produces no detected acetyl-cysteine when CO-treated and is distant from the A-cluster (Figure 2.20).

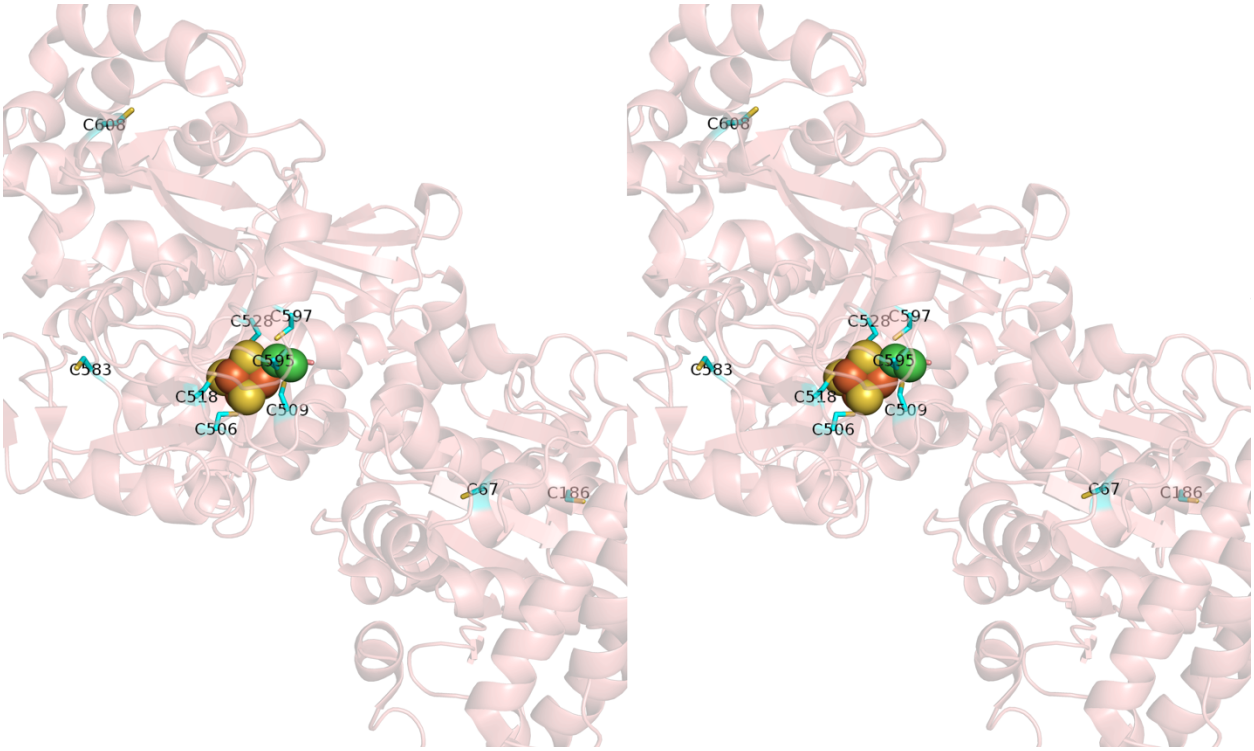

Figure 2.20 Cross-eye stereogram model of the open ACS A-cluster highlighting cysteine residues. All 10 cysteines present in ACS, highlighted in cyan. PDB 1OAO.

2.4.4 Conclusion

Based on the evidence in this work, we conclude the ACS A-cluster uses an organometallic reductant-mediated nucleophilic methyl transfer that rapidly oxidizes to a diamagnetic state. We utilized numerous spectroscopic methods under differing reducing conditions which have provided no evidence of a relevant paramagnetic A-cluster after methylation despite UV-visible observation indicating strong methyl transfer. The UV-visible data under substoichiometric equivalents of Ti(III) citrate reductant provide strong evidence of a highly oxidizing short-lived intermediate that oxidizes the Cob(I)inamide to Cob(II)inamide in the absence of excess Ti(III) equivalents. Mass spectrometry experiments have provided evidence countering a previously proposed alternative mechanism utilizing a cysteine near the A-cluster as the primary methylation site. The lack of any observed trends in cysteine methylation and acetylation strongly suggests a methyl-Ni_p is the catalytically relevant species in ACS after methylation.

2.5 References for Chapter 2

(1) Adam, P. S.; Borrel, G.; Gribaldo, S. Evolutionary history of carbon monoxide dehydrogenase/acetyl-CoA synthase, one of the oldest enzymatic complexes. *Proceedings of the National Academy of Sciences* **2018,** *115* (6), E1166.

(2) Ragsdale, S. W.; Pierce, E. Acetogenesis and the Wood-Ljungdahl pathway of CO(2) fixation. *Biochimica et Biophysica Acta* **2008,** *1784* (12), 25.

(3) Burton, R.; Can, M.; Esckilsen, D.; Wiley, S.; Ragsdale, S. W.; Armstrong, F. In *Methods in Enzymology*; Academic Press, 2018; Vol. 613.

(4) Zhuang, W.-Q.; Yi, S.; Bill, M.; Brisson, V. L.; Feng, X.; Men, Y.; Conrad, M. E.; Tang, Y. J.; Alvarez-Cohen, L. Incomplete Wood–Ljungdahl pathway facilitates one-carbon metabolism in organohalide-respiring *Dehalococcoides mccartyi*. *Proceedings of the National Academy of Sciences* **2014,** *111* (17), 6419.

(5) Shanmugasundaram, T.; Wood, H. G. Interaction of ferredoxin with carbon monoxide dehydrogenase from *Clostridium thermoaceticum*. *Journal of Biological Chemistry* **1992,** *267* (2), 3.

(6) Ragsdale, S. W.; Wood, H. G. Acetate Biosynthesis by Acetogenic Bacteria: Evidence that Carbon Monoxide Dehydrogenase is the Condensing Enzyme that Catalyzes the Final Steps of the Synthesis. *The Journal of Biological Chemistry* **1985,** *260* (7), 7.

(7) Can, M.; Armstrong, F. A.; Ragsdale, S. W. Structure, Function, and Mechanism of the Nickel Metalloenzymes, CO Dehydrogenase, and Acetyl-CoA Synthase. *Chemical Reviews* **2014,** *114* (8), 25.

(8) Hegg, E. L. Unraveling the Structure and Mechanism of Acetyl-Coenzyme A Synthase. *Accounts of Chemical Research* **2004,** *37* (10), 775.

(9) Ragsdale, S. W.; Wood, H. G.; Antholine, W. E. Evidence that an iron-nickel-carbon complex is formed by reaction of CO with the CO dehydrogenase from *Clostridium thermoaceticum*. *Proceedings of the National Academy of Sciences* **1985,** *82* (20), 6811.

(10) Can, M.; Giles, L. J.; Ragsdale, S. W.; Sarangi, R. X-ray Absorption Spectroscopy Reveals an Organometallic Ni–C Bond in the CO-Treated Form of Acetyl-CoA Synthase. *Biochemistry* **2017,** *56* (9), 12.

(11) Harrop, T. C.; Mascharak, P. K. Structural and spectroscopic models of the A-cluster of acetyl coenzyme a synthase/carbon monoxide dehydrogenase: Nature's Monsanto acetic acid catalyst. *Coordination Chemistry Reviews* **2005,** *249* (24), 3007.

(12) Doukov, T. I.; Blasiak, L. C.; Seravalli, J.; Ragsdale, S. W.; Drennan, C. L. Xenon in and at the End of the Tunnel of Bifunctional Carbon Monoxide Dehydrogenase/Acetyl-CoA Synthase. *Biochemistry* **2008,** *47* (11), 9.
(13) Doukov, T. I.; Iverson, T. M.; Seravalli, J.; Ragsdale, S. W.; Drennan, C. L. A Ni-Fe-Cu Center in a Bifunctional Carbon Monoxide Dehydrogenase/ Acetyl-CoA Synthase. *Science* **2002,** *298* (5593), 567.
(14) Volbeda, A.; Fontecilla-Camps, J. C. Crystallographic evidence for a CO/CO2 tunnel gating mechanism in the bifunctional carbon monoxide dehydrogenase/acetyl coenzyme A synthase from *Moorella thermoacetica*. *JBIC Journal of Biological Inorganic Chemistry* **2004,** *9* (5), 525.
(15) Darnault, C.; Volbeda, A.; Kim, E. J.; Legrand, P.; Vernède, X.; Lindahl, P. A.; Fontecilla-Camps, J. C. Ni-Zn-[Fe4-S4] and Ni-Ni-[Fe4-S4] clusters in closed and open α subunits of acetyl-CoA synthase/carbon monoxide dehydrogenase. *Nature Structural Biology* **2003,** *10*, 271.
(16) Drennan, C. L.; Heo, J.; Sintchak, M. D.; Schreiter, E.; Ludden, P. W. Life on carbon monoxide: X-ray structure of *Rhodospirillum rubrum* Ni-Fe-S carbon monoxide dehydrogenase. *Proceedings of the National Academy of Sciences* **2001,** *98* (21), 11973.
(17) Tan, X.; Bramlett, M. R.; Lindahl, P. A. Effect of Zn on Acetyl Coenzyme A Synthase: Evidence for a Conformational Change in the α Subunit during Catalysis. *Journal of the American Chemical Society* **2004,** *126* (19), 5954.
(18) Seravalli, J.; Xiao, Y.; Gu, W.; Cramer, S. P.; Antholine, W. E.; Krymov, V.; Gerfen, G. J.; Ragsdale, S. W. Evidence That NiNi Acetyl-CoA Synthase Is Active and That the CuNi Enzyme Is Not. *Biochemistry* **2004,** *43* (13), 11.
(19) Svetlitchnyi, V.; Dobbek, H.; Meyer-Klaucke, W.; Meins, T.; Thiele, B.; Römer, P.; Huber, R.; Meyer, O. A functional Ni-Ni-[4Fe-4S] cluster in the monomeric acetyl-CoA synthase from *Carboxydothermus hydrogenoformans*. *Proceedings of the National Academy of Sciences of the United States of America* **2004,** *101* (2), 446.
(20) Seravalli, J.; Ragsdale, S. W. Pulse-Chase Studies of the Synthesis of Acetyl-CoA by Carbon Monoxide Dehydrogenase/Acetyl-CoA Synthase: Evidence for a Random Mechanism of Methyl and Carbonyl Addition. *Journal of Biological Chemistry* **2007,** *283* (13), 10.
(21) Ragsdale, S. W.; Ljungdahl, L. G.; DerVartanian, D. V. ^{13}C and ^{61}Ni isotope substitutions confirm the presence of a nickel(III)-carbon species in acetogenic CO dehydrogenases. *Biochemical and Biophysical Research Communications* **1983,** *115* (2), 7.
(22) Ragsdale, S. W.; Ljungdahl, L. G.; DerVartanian, D. V. EPR evidence for nickel-substrate interaction in carbon monoxide dehydrogenase from *Clostridium thermoaceticum*. *Biochemical and Biophysical Research Communications* **1982,** *108* (2), 5.
(23) Bender, G.; Stitch, T. A.; Yan, L.; Britt, R. D.; Cramer, S. P.; Ragsdale, S. W. Infrared and EPR Spectroscopic Characterization of a Ni(I) Species Formed by Photolysis of a Catalytically Competent Ni(I)-CO Intermediate in the Acetyl-CoA Synthase Reaction. *Biochemistry* **2010,** *49* (35), 7.
(24) Chen, J.; Huang, S.; Seravalli, J.; Gutzman, H.; Swartz, D. J.; Ragsdale, S. W.; Bagley, K. A. Infrared Studies of Carbon Monoxide Binding to Carbon Monoxide Dehydrogenase/Acetyl-CoA Synthase from *Moorella thermoacetica*. *Biochemistry* **2003,** *42* (50), 14822.
(25) Kumar, M.; Ragsdale, S. W. Characterization of the carbon monoxide binding site of carbon monoxide dehydrogenase from *Clostridium thermoaceticum* by infrared spectroscopy. *Journal of the American Chemical Society* **1992,** *114* (22), 8713.
(26) Fan, C.; Gorst, C. M.; Ragsdale, S. W.; Hoffman, B. M. Characterization of the nickel-iron-carbon complex formed by reaction of carbon monoxide with the carbon monoxide dehydrogenase from *Clostridium thermoaceticum* by Q-band ENDOR. *Biochemistry* **1991,** *30* (2), 431.
(27) Gorst, C. M.; Ragsdale, S. W. Characterization of the NiFeCO complex of carbon monoxide dehydrogenase as a catalytically competent intermediate in the pathway of acetyl-coenzyme A synthesis. *Journal of Biological Chemistry* **1991,** *266* (31), 20687.
(28) George, S. J.; Seravalli, J.; Ragsdale, S. W. EPR and Infrared Spectroscopic Evidence That a Kinetically Competent Paramagnetic Intermediate is Formed When Acetyl-Coenzyme A Synthase Reacts with CO. *Journal of the American Chemical Society* **2005,** *127* (39), 1.
(29) Seravalli, J.; Kumar, M.; Ragsdale, S. W. Rapid Kinetic Studies of Acetyl-CoA Synthesis: Evidence Supporting the Catalytic Intermediacy of a Paramagnetic NiFeC Species in the Autotrophic Wood−Ljungdahl Pathway. *Biochemistry* **2002,** *41* (6), 1807.

(30) Seravalli, J.; Brown, K. L.; Ragsdale, S. W. Acetyl Coenzyme A Synthesis from Unnatural Methylated Corrinoids: Requirement for "Base-Off" Coordination at Cobalt. *Journal of the American Chemical Society* **2001,** *123* (8), 1786.
(31) Tan, X.; Sewell, C.; Lindahl, P. A. Stopped-Flow Kinetics of Methyl Group Transfer between the Corrinoid-Iron-Sulfur Protein and Acetyl-Coenzyme A Synthase from C*lostridium thermoaceticum*. *Journal of the American Chemical Society* **2002,** *124* (22), 7.
(32) Menon, S.; Ragsdale, S. W. The Role of an Iron-Sulfur Cluster in an Enzymatic Methylation Reaction: METHYLATION OF CO DEHYDROGENASE/ACETYL-CoA SYNTHASE BY THE METHYLATED CORRINOID IRON-SULFUR PROTEIN. *Journal of Biological Chemistry* **1999,** *274* (17), 11513.
(33) Menon, S.; Ragsdale, S. W. Role of the [4Fe-4S] Cluster in Reductive Activation of the Cobalt Center of the Corrinoid Iron−Sulfur Protein from *Clostridium thermoaceticum* during Acetate Biosynthesis. *Biochemistry* **1998,** *37* (16), 5689.
(34) Lindahl, P. A. Acetyl-coenzyme A synthase: the case for a Ni_p0-based mechanism of catalysis. *Journal of Biological Inorganic Chemistry* **2004,** *9*, 8.
(35) Pezacka, E.; Wood, H. G. Acetyl-CoA pathway of autotrophic growth. Identification of the methyl-binding site of the CO dehydrogenase. *Journal of Biological Chemistry* **1988,** *263* (31), 16000.
(36) Bramlett, M. R.; Stubna, A.; Tan, X.; Surovtsev, I. V.; Münck, E.; Lindahl, P. A. Mössbauer and EPR Study of Recombinant Acetyl-CoA Synthase from *Moorella thermoacetica*. *Biochemistry* **2006,** *45* (28), 8674.
(37) Xia, J.; Hu, Z.; Popescu, C. V.; Lindahl, P. A.; Münck, E. Mössbauer and EPR Study of the Ni-Activated α-Subunit of Carbon Monoxide Dehydrogenase from *Clostridium thermoaceticum*. *Journal of the American Chemical Society* **1997,** *119* (35), 8301.
(38) Thauer, R. K. Biochemistry of methanogenesis: a tribute to Marjory Stephenson:1998 Marjory Stephenson Prize Lecture. **1998,** *144* (9), 2377.
(39) Jaun, B. Coenzyme F430 from Methanogenic Bacteria: Oxidation of F430 Pentamethyl Ester to the Ni(III) Form. *Helvetica Chimica Acta* **1990,** *73* (8), 2209.
(40) Seefeldt, L. C.; Ensign, S. A. A Continuous, Spectrophotometric Activity Assay for Nitrogenase Using the Reductant Titanium(III) Citrate. *Analytical Biochemistry* **1994,** *221* (2), 379.
(41) Wedemeyer-Exl, C.; Darbre, T.; Keese, R. Preparation of Dicyano- and Methylcobinamide from Vitamin B12a. *Synthesis-stuttgart* **2008,** *2008*, 3429.
(42) Elliott, J. I.; Brewer, J. M. The inactivation of yeast enolase by 2,3-butanedione. *Archives of Biochemistry and Biophysics* **1978,** *190* (1), 351.
(43) Lawrence, A. D.; Taylor, S. L.; Scott, A.; Rowe, M. L.; Johnson, C. M.; Rigby, S. E. J.; Geeves, M. A.; Pickersgill, R. W.; Howard, M. J.; Warren, M. J. FAD binding, cobinamide binding and active site communication in the corrin reductase (CobR). *Bioscience reports* **2014,** *34* (4), e00120.
(44) Broderick, W. E.; Broderick, J. B. Radical SAM enzymes: surprises along the path to understanding mechanism. *JBIC Journal of Biological Inorganic Chemistry* **2019,** *24* (6), 769.
(45) Sétif, P.; Seo, D.; Sakurai, H. Photoreduction and Reoxidation of the Three Iron-Sulfur Clusters of Reaction Centers of Green Sulfur Bacteria. *Biophysical Journal* **2001,** *81* (3), 1208.
(46) Manesis, A. C.; Musselman, B. W.; Keegan, B. C.; Shearer, J.; Lehnert, N.; Shafaat, H. S. A Biochemical Nickel(I) State Supports Nucleophilic Alkyl Addition: A Roadmap for Methyl Reactivity in Acetyl Coenzyme A Synthase. *Inorganic Chemistry* **2019,** *58* (14), 8969.
(47) Thomson, J.; Baird, M. C. Trends in the Spectrochemical Series and ^{31}P Chemical Shifts of Five-coordinated Cyclopentadienylnickel(II) Complexes. *Canadian Journal of Chemistry* **1973,** *51* (8), 1179.

Chapter 3

A Molecular Backboard Required for Anaerobic CO_2 Fixation in Acetyl-CoA Synthase[1]

3.1 Abstract

Acetyl-CoA synthase (ACS) is the key enzyme in the Wood-Ljungdahl pathway of anaerobic carbon dioxide and carbon monoxide fixation. ACS catalyzes carbon-carbon and carbon-sulfur bond formation in the final steps in acetyl-CoA synthesis by condensing carbon monoxide with coenzyme A and the methyl group of a methylated corrinoid substrate. Significant evidence implicates nickel-carbonyl, methyl-nickel and acetyl-nickel intermediates in the ACS mechanism. There also is convincing evidence for a molecular tunnel between the site of CO synthesis at the C-cluster of carbon monoxide dehydrogenase (CODH) and the dinickel-iron-sulfur-containing A-cluster of ACS. Finally, structural and kinetic studies have revealed that ACS contains an alcove near the key proximal nickel center in the A-cluster that is implicated in binding the CO, methyl, and CoA groups. As described here, an alanine substitution for a phenylalanine residue (F229A), which appears to form a wall of the alcove, disables CO binding to the nickel center. Kinetic, spectroscopic and structural studies demonstrate that all reactions of ACS involving interactions with CO are severely disrupted. On the other hand, the A-cluster metallocenter properly assembles and methylation of ACS occurs in the F229A variant with the same rate and to the same extent as the wild type protein. These studies indicate that the alcove and specifically F229A acts as a molecular backboard to productively bind substrate CO and form the key nickel-carbonyl intermediate in the WLP.

[1] The contents of this chapter were adapted and reproduced from a manuscript in preparation: Wiley, S.A., Sarangi, R., Eckert, P., Meuller, A.P., Nogle, R., Simpson, S., Köpke, M., Can, M., Kubarych, K., Ragsdale, S.W. "A Molecular Backboard Required for Anaerobic CO_2 Fixation in Acetyl-CoA Synthase."

3.2 Introduction

One of the largest threats facing humanity is the increasing global concentration of carbon dioxide in the atmosphere, affecting wide-reaching aspects such as rising sea levels, ocean acidification, and more severe weather[1,2]. There is a need to understand the mechanism of carbon fixation and how it can be applied to enhance CO_2 uptake from the atmosphere, e.g., by developing cost-effective and environmentally-friendly ways to produce fuels and valuable chemicals[3,4]. There are six known CO_2 fixation pathways and among these, the Wood-Ljungdahl (or reductive acetyl-CoA) Pathway (WLP) is of particular interest due to its high energy efficiency as the only CO_2 fixation pathway that generates net ATP. The WLP is responsible for annual production of 10 billion tons of acetate in the US alone[5,6]. Found in strictly anaerobic bacteria, this is an ancient pathway that was present in the last universal common ancestor[7]. This pathway also fixes carbon monoxide and is unique among biochemical pathways in utilizing a series of nickel-based organometallic intermediates[6], (Figure 3.1). Here we demonstrate that the key enzyme in this pathway, acetyl-CoA synthase (ACS) unexpectedly requires a molecular backboard to productively bind carbon monoxide and form the key nickel-carbonyl intermediate in the WLP.

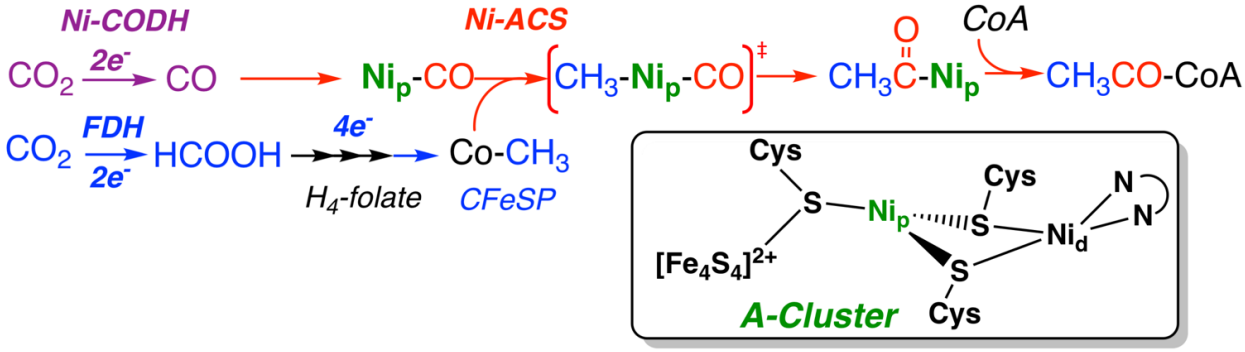

Figure 3.1 Wood Ljungdahl Pathway. CO_2 enters the WLP at the Eastern (Methyl) branch, where it undergoes 6 electron reduction to Co-CH_3, and the Western (Carbonyl) branch where CODH catalyzes reduction of a second CO_2 to CO followed by conversion of CO, methyl and CoA to acetyl-CoA at the A-cluster of ACS (shown to the bottom right). CFeSP, the Corrinoid Iron-Sulfur Protein.

The key enzymes in the WLP are Carbon Monoxide Dehydrogenase (CODH) and ACS, which form a complex. CODH/ACS assembles into a heterotetrameric enzyme complex with 4 [Fe_4S_4] clusters, two of which are unique, nickel-containing active site clusters, the C-cluster in CODH and the A-cluster in ACS[8,9]. The CODH C-cluster catalyzes CO_2 reduction to CO, while the A-cluster of ACS binds nascent CO, a methyl group donated by the methylated state of the Corrinoid Iron-Sulfur Protein (CFeSP) and coenzyme A (Figure 3.1). Although Figure 3.1 shows an ordered reaction sequence, ACS can productively and randomly bind either CO or methyl as the first substrate[10]. ACS then catalyzes C-C bond formation between bound CO and methyl to form an acetyl intermediate, then C-S bond formation by reacting the acetyl group with CoA to generate acetyl-CoA, which serves as an energy source and metabolic building block for the cell[11]. During this process, the CO generated at the CODH C-cluster migrates 70 Å through an interprotein gas channel to the ACS A-Cluster[12].

Earlier kinetic, spectroscopic and structural studies suggested that hydrophobic residues near the proximal nickel center in the A-cluster form the walls of an alcove that facilitates binding the CO, methyl, and CoA groups. As described here, we tested the functional role of this alcove by replacing a bulky phenylalanine residue (F229A), which appeared to form a wall of the alcove, with alanine and found that all reactions of ACS involving interactions with CO are severely disrupted. On the other hand, the A-cluster in the variant F229A properly assembles; furthermore, methylation of ACS occurs with the same rate and to the same extent as the wild type protein. The F229W substitution does not seem to adversely affect A-cluster assembly, substrate binding or catalysis. These studies indicate that the alcove and specifically F229A acts as a molecular backboard to productively bind substrate CO and form the key nickel-carbonyl intermediate in the WLP.

3.3 Materials and Methods

3.3.1 Generation of Monofunctional ACS Alcove Variants

A pET29 vector (Kan^R, His6-tagged, *lac*-inducible) harboring the *Moorella thermoacetica acsB* gene containing the Acetyl-CoA Synthase subunit of CODH/ACS, known as $pET29ACSMT_{HT}$ was used as a basis for generation of ACS phenylalanine-229 variants. ACS variants F229A and F229W were generated with a QuikChange II site-directed mutagenesis kit

from Agilent Technologies using primers (Integrated DNA Technologies) containing the sequences for F229W and F229A respectively: F229W – *sense* 5'- C CTG CGG GCT GGT ATG ATG TGG GGT -3' *antisense* 5'- GT AAC GCC ACC CCA CAT CAT ACC AGC -3'; F229A – *sense* 5'- G CGG GCT GGT ATG ATG GCC GGT GGC -3' *antisense* 5'- GGT AAC GCC ACC GGC CAT CAT ACC A -3'. Wild-type ACS was left unadulterated. The ACS variant plasmids were respectively transformed into competent BL21(DE3) *E. coli* cells along with the pBD1282 plasmid (Amp^R, *ara*-inducible) containing the genes *iscS-iscU-iscA-hscB-hscA-fdx* from *A. vinlandii* for proper [Fe_4S_4] construction[10].

3.3.2 Growth of *Clostridium autoethanogenum*

Growth of *C. autoethanogenum* was carried out under strictly anaerobic conditions as described earlier using a modified version of PETC-MES media and a derivative strain of *C. autoethanogenum* type strain DSM10061 obtained from DSMZ (Deutsche Sammlung von Mikroorganismen und Zellkulturen)[13,14]. When noted, 10 g L^{-1} of fructose was added to the medium. For plasmid maintenance, Thiamphenicol was added to a concentration of 15 mg L^{-1}. Tests for autotrophic and heterotrophic growth were performed in 12-well round-well plates with each well containing 2 mL of growth medium. Wells were inoculated in a glovebox (Inert®) with a N_2 atmosphere, then plates were placed in custom pressure-rated stainless-steel jars. For each genotype, we tested 3 biological replicates. The headspace of the jar was replaced with 170 kPa (gauge) of a synthetic $CO/CO_2/H_2/N_2$ (50%/30%/10%/10%) gas blend (Airgas) for autotrophic growth conditions and left with ambient pressure of N_2 (Airgas) for heterotrophic growth on fructose. Jars were shaken at 90 rpm with a 2.5cm throw and incubated at 37°C for growth.

3.3.3 Genetic modification of *C. autoethanogenum*

Homologous recombination, with Cas9-mediated counter selection, facilitated deletion of *acsB* in *C. autoethanogenum* with target-specific modifications from the method previously described[15]. Namely, we amplified homology arms from genomic DNA with the oligonucleotides listed in Table 3.1 and used TCACCAAATGTCATTCCAAG as the recognition sequence for the guide RNA. The vector was assembled with the GeneArt® Seamless Cloning kit (Thermo, USA). We included fructose in the medium during deletion of

acsB since we anticipated the essentiality of the gene for autotrophic growth. For expression of *acsB*, we amplified the gene from genomic DNA and cloned it into pMTL83151-P_{acsA} using oligonucleotides listed in Table 3.1[16]. We created the F209A substitution using the KLD kit (New England Biolabs) with oligonucleotides listed in Table 3.1.

Table 3.1 Oligonucleotides used for *C. autoethanogenum* genetic modification

Oligo name	Sequence
Gene deletion (binding sequences in bold)	
Left homology arm F	CTTCTTATTTTTATGGCGCGCC**ATTTTCCACAGGACCCACTTCC**
Left homology arm R	AAGATAACTAATG**CTTGCATCTATGACAGGTGGTGG**
Right homology arm F	GATGCAAG**CATTAGTTATCTTTTTTCCTGTAGCTGC**
Right homology arm R	TTGTTCAAAAAAATAATGGC**TGAACATGGATAAATTTATGATCATAGGCG**
acsB cloning (binding sequences in bold)	
acsB F	GGAGGGAATTATTCATATGAATTTATTTCAAACTGTATTCACTGG
acsB R	CAGTCACGACGCTACATTATTGGATCCATCTTTAATGCAG
Vector F	CCAATAATGTAGCGTCGTGACTGGGAAAACC
Vector R	GAAATAAATTCATATGAATAATTCCCTCCTTAAAGAAATAACTTC
acsB mutagenesis (altered codon in bold)	
F209A F	GGAGGAATTAAGGGTGGTCAG
F209A R	**CGC**TATAAGTGCAGCTCTTATAGC

**Table provided by Alex Mueller, Robert Nogle, Dr. Séan Simpnson, and Dr. Michael Köpke at Lanzatech (Skokie, IL)*

3.3.4 Growth, Expression, Lysis, and Purification of His6-tagged Monofunctional ACS variants from *E. coli* cells

Growth of *E. coli* cells harboring the ACS variant plasmids was conducted as previously described[10]. Lysis and purification of ACS and variants was performed as previously described with protein concentrations verified by the Rose Bengal Assay[10,17]. All buffers and reagents were prepared under strict anaerobic conditions ($\leq$ 2.5 ppm O_2), and all glassware used in purification was acid washed for no less than one hour to remove any metal contaminants.

3.3.5 Metal Reconstitution of Monofunctional ACS Variants

Reconstitution of pure ACS was performed as described previously[18]. ACS metal content (Table 3.2) post reconstitution is quantified by ICP-OES through the Center for Applied Isotope

Studies (CAIS) at the University of Georgia (Athens, GA) in comparison to the protein concentration verification by the Rose Bengal assay[17].

Table 3.2 Variant Metal Content Determined by ICP-OES.

ACS Variant	Iron per ACS	Nickel per ACS
Expected	*4.0*	*2.0*
Wildtype	3.3 ± 0.4	1.8 ± 0.4
F229W	3.0 ± 0.7	1.7 ± 0.4
F229A*	3.8 ± 0.3	2.4 ± 0.2

**Concentration methods were improved between purifications. Variants were initially concentrated using centrifugal concentrators but were changed from centrifugation to pressure concentration. Pressure concentration appeared to increase metal retention in ACS protein.*

3.3.6 EPR Analysis of Natural Abundance and Isotopically Labeled ACS-CO Variants

Continuous-wave X-band EPR data were collected on a Bruker EMX equipped using a variable-temperature Cold-Edge liquid helium condensing unit with a Mercury iTC cryostat by Oxford Instruments. All spectra were collected using WinEPR Acquisition software. EPR samples were prepared as previously described[19-21] by anaerobic mixing of ACS in 50 mM potassium phosphate pH 7.5 with 2 mM sodium dithionite, transferred to an EPR tube capped with a rubber septum, and purged with 100% carbon monoxide gas (UHP; Cryogenic Gases, Detroit, MI) for 25 minutes before being flash frozen in liquid nitrogen. Protein concentration was assessed in parallel by the Rose Bengal assay[17]. Isotopically labeled ACS variants were treated as previous CO samples, but purge time was reduced to 10 minutes to minimize wasted ^{13}CO gas. All samples were stored at -80˚C prior to spectrum acquisition. Natural-Abundance (NA) WT and F229W EPR spectra were collected at 40 K with a power of 20.8 mW, a modulation frequency of 100 kHz, a modulation amplitude of 10 G, gain of 2000, conversion time of 81.92 ms, and a time constant of 40.96 ms. NA F229A EPR spectrum was collected at 100 K with a power of 20.8 mW, a modulation frequency of 100 kHz, a modulation amplitude of 10 G, gain of 4480, conversion time of 40.96 ms, and a time constant of 20.48 ms. ^{13}CO WT EPR spectrum was collected at 100 K with a power of 2.08 mW, with a modulation frequency of 100 kHz, a modulation amplitude of 10 G, gain of 4480, conversion time of 163.84 ms, and a time constant of 40.96 ms. ^{13}CO F229W and F229A spectra were collected at 100 K with a power of 20.8 mW, modulation frequency of 100 kHz, a modulation amplitude of 10 G, gain of

4480, conversion time of 40.96 ms, and a time constant of 20.48 ms. Analysis of EPR spectra was conducted using WinEPR Processing software, and and resultant ACS spectra were quantitatively measured by comparison to a 1 mM Cu(II) perchlorate standard using the equation from Fee, 1978[22].

3.3.7 Copper (II) Perchlorate Standard

An initial 10 mM Cu(II) perchlorate standard stock is prepared for spin quantitation by mixing together 12.24 g sodium perchlorate (Sigma), 0.125 gram Cu(II) sulfate pentahydrate (99.999% purity; Sigma), and 42 µL saturated (12 M) HCl with ultrapure water to a final volume of 50 mL. 10 mM Cu(II) perchlorate stock is diluted by 10 to 1 mM standard with high purity water, where a 200 µL aliquot is transferred to an EPR tube and frozen with liquid N_2.

3.3.8 Radiolabeled CO-Exchange Assay

Radiolabeled [1-^{14}C]-acetyl-CoA exchange assay was prepared in 300 mM MES buffer, pH 6.1 with a headspace of 100% CO with Ti(III) used in lieu of DTT and 0.05 µCi of [1-^{14}C]-acetyl-CoA, but was performed as previously described[23]. Analysis of [1-^{14}C]-acetyl-CoA exchange data was based on previous studies on CODH/ACS acetyl-CoA exchangeability[23,24], and had been adapted for monofunctional ACS and its variants[18].

3.3.9 Preparation of Titanium (III) Citrate Reductant

83 mM titanium (III) citrate reductant was prepared anaerobically as previously described[25]. Ti(III) citrate solutions were stored anaerobically at RT away from light in a brown glass vial.

3.3.10 FTIR Sample Preparation

Fourier Transform Infrared (FTIR) ACS variant samples were prepared by buffer exchange of variants into 50 mM potassium phosphate in D_2O, pH 7.7, then concentration of the variants to an expected 1 mM using ultracentrifugal filters with a 30 kDa cutoff membrane, spun in a tabletop centrifuge at 10,000 rpm for 4 minutes. Concentrated ACS samples were purged with pure CO gas for 10 minutes in stoppered and crimped 2 mL vials, where the final ACS concentration was assessed by the Rose Bengal assay[17]. After CO purging, the samples were

transported in airtight containers to a collaborator's anaerobic chamber, where the samples were transferred to a CaF_2 FTIR sample window. Once in the FTIR window, the sample was removed from the chamber and the IR spectrum taken immediately on a JASCO FT/IR-4600 compared to a D_2O buffer blank.

3.3.11 XAS Sample Preparation

X-ray Absorption Spectroscopy (XAS) ACS-F229W and -F229A samples were prepared as previously described[26]. Three protein states were prepared for F229W and F229A; ACS_{ox}, ACS_{red}, ACS_{red}-CO. ACS_{ox} was unreduced, as-isolated protein; ACS_{red} was protein reduced with 2 mM sodium dithionite; ACS_{red}-CO was reduced protein purged with pure CO for 10 minutes in a sealed and crimped vial. Final variant concentration was 1 mM after addition of 30% glycerol as a glassing agent in 50 mM potassium phosphate, pH 7.5, and protein concentration was verified by the Rose Bengal assay[17]. Variant samples were quickly placed in XAS sample cells, removed from the anaerobic chamber, flash frozen in liquid nitrogen, and shipped overnight to the SSRL for data acquisition and analysis.

3.3.12 Methylation of ACS Variants

Methylation of ACS variants was performed in darkness with red light by Stopped-Flow UV-Visible spectrophotometry (Applied Photophysics SX20; single-wavelength monochromator), using methyl-cobinamide (MeCbi) as a methyl donor, and Ti(III) citrate as a reducing agent. A reaction solution consisting of 10 µM ACS and 30 µM Ti(III) citrate was prepared in 50 mM potassium phosphate, pH 7.5. Reaction solutions containing ACS were blanked, and the experiment began with addition of 10 µM MeCbi. Resultant spectral changes associated with cobinamide ligand changes and redox shift from 3+ to 1+ state and were quantified using the change absorption of 17 mM^{-1} cm^{-1} at 390 nm ($\Delta\varepsilon_{390}$ = 17 mM^{-1} cm^{-1}), or the difference between methyl-Cob(III)inamide ($\varepsilon_{390,MeCbi}$ = 8 mM^{-1} cm^{-1}) and Cob(I)inamide ($\varepsilon_{390,Co(I)bi}$ = 25 mM^{-1} cm^{-1}). The change spectral changes were also quantified at 470 nm ($\varepsilon_{470,MeCbi}$ = 11 mM^{-1} cm^{-1}; $\varepsilon_{470,Co(I)bi}$ = 3 mM^{-1} cm^{-1}; $\Delta\varepsilon_{470}$ = 8 mM^{-1} cm^{-1}).

3.3.13 Preparation of Methyl-Cob(III)inamide

Methyl-Cob(III)inamide was prepared as described by Wedemeyer-Exl, 2008[27] and an anaerobic 40% methyl iodide/60% methanol solution is prepared on ice by blowing high purity nitrogen over the mixture for 5 minutes. Once the 40% MeI/methanol solution is prepared, the methyl-Cob(III)inamide is made anaerobically by mixing 1x (mol/mol) dicyano-cobinamide (≥93%; Sigma Aldrich) with 6x (mol/mol) Ti(III) citrate in a brown glass vial. The vial is then stoppered with rubber septum, and 240x (mol/mol) of the previously prepared 40% MeI/methanol solution is added and left to react at room temperature for ≥ 2 hours. After reacting, the solution is then purified via size-exclusion with 50 mM potassium phosphate buffer, pH 7.5 under green light by an anaerobic Biogel P2 (Bio-Rad; 100-1800 MW cutoff) and collected in 0.5 mL aliquots and checked for purity via UV-Visible spectroscopy using ε_{390} = 8 mM^{-1} cm^{-1} and ε_{470} = 10.8 mM^{-1} cm^{-1}. Pure and concentrated MeCbi aliquots are pooled, quantified, and stored at -20˚C.

3.4 Results & Discussion

To examine the importance of the alcove in ACS activity, we compared the properties of the F229W and F229A variants with those of the wild-type protein (Table 3.3). The variants exhibit a metal content (Table 3.2) that is very similar to that of wild-type protein, consistent with near compete occupancy of the A-cluster. This is consistent with the results of X-ray absorption and Mossbauer studies, described below.

3.4.1 An Intact Alcove is Required for Productive Carbonylation of ACS

The carbonylation activity of ACS is routinely measured by isotopic dilution of a [1-^{14}C]-acetyl-CoA substrate in the presence of an unlabeled CO headspace, where the labeled carbonyl group of acetyl-CoA exchanges with unlabeled CO[28,29]; While the wildtype and the F229W variants exhibit high specific activities (2.1 and 1.68 μmol_{AcCoA} min^{-1} mg^{-1}, respectively), the specific activity of the F229A variant was less than half, but quickly plateaued at a third of the wild-type exchange percentage indicating a stalling of carbonyl exchange (Figure 3.2, (A)).

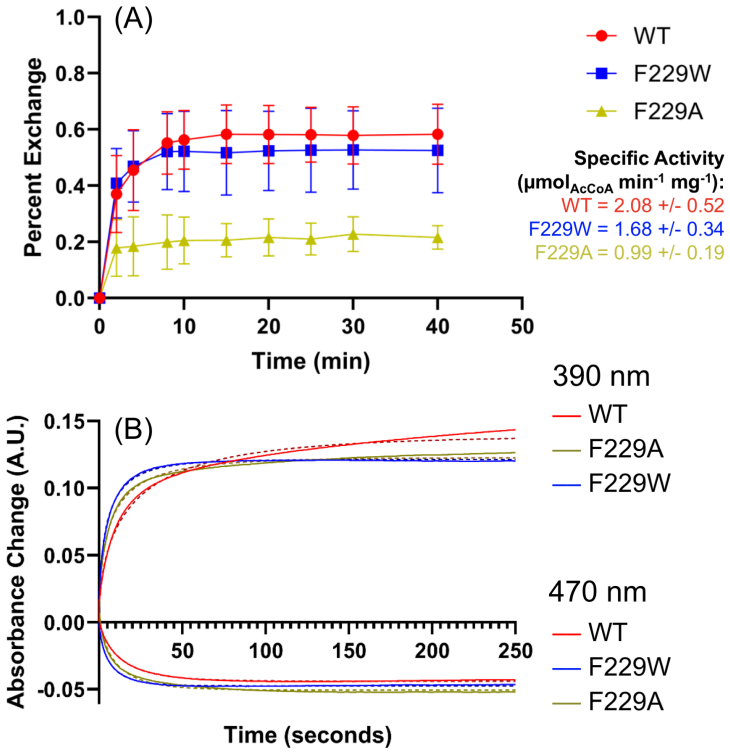

Figure 3.2 Comparison of the acetyl-CoA exchange activities and methylation rates of wild-type ACS to those of F229A and F229W variants. (**A**) [1-^{14}C]-acetyl-CoA Exchange Assay of ACS. 50 nM ACS was prepared in 300 mM MES, pH 6.1, 2 mM Ti(III) citrate, 200 μM methyl viologen, 20 mM KCl, and 200 μM acetyl-CoA, incubated with a headspace of 100% carbon monoxide gas before the assay was started by the addition of 0.05 μCi [1-^{14}C]-acetyl-CoA. The total percent change versus time for the radiolabeled exchange of the ACS variants. The exchange data indicate F229A's activity is decreased relative to the WT and F229W. (**B**) Methylation of ACS by methyl-Cob(III)inamide (MeCbi). Stopped Flow traces of 10 μM ACS reduced with 3x Ti(III) citrate and methylated with 10μM MeCbi measured by monitoring the time-dependent decrease in absorbance at 470 nm of MeCbi and the increase at 390 nm of Cob(I)inamide. The rates and percentages of methylation are shown in Table 1.

Incubation of the F229W variant with CO leads to an intense 1995 cm^{-1} Fourier Transform Infrared (FTIR) signal similar to that of the wild-type protein (Figure 3.3, (A)). This signal has been assigned to the stretching frequency of the nickel-carbonyl of the A-cluster[30]. Stopped Flow-Fourier Transform Infrared (SF-FTIR) and rapid freeze-quench (RFQ) EPR experiments have validated the catalytic competence of this species by demonstrating that the 1995 cm^{-1} IR band appears coincident with the NiFeC EPR signal[31] and that these species disappear upon RFQ reaction with the methylated CFeSP at a rate constant of 6 s^{-1} [32]. Both formation and decay of the IR and EPR signals occurred at rates faster than the steady-state activity of CODH/ACS.

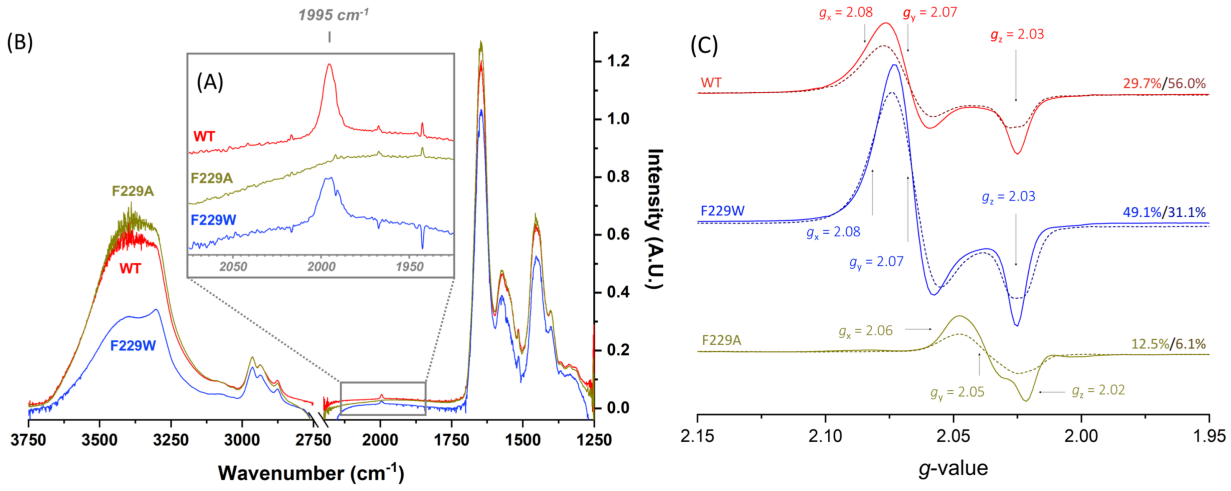

Figure 3.3 FTIR and EPR spectra of ACS variants. The protein concentrations were: WT, 580 ± 12 µM; F229W, 590 ± 26 µM, and F229A, 580 ± 16 µM. (**A**) Infrared spectra highlight of the characteristic Ni-CO stretch at 1995 cm^{-1} between the region 1970 to 2020 cm^{-1}. The Ni-CO stretch is noticeably absent in F229A, while the WT and F229W have strong Ni-CO signals. The integrated area of the F229W Ni-CO peak is 83% of the WT area. (**B**) The full IR spectra of the ACS variants showing global folding similarity. Bands belonging to ACS include the various amide bands over the 1250 to 1750 cm^{-1}, the C-H bonds from 2800 to 3000 cm^{-1}, and the N-H and O-H stretches from 3200 to 3750 cm^{-1}. The region between 2200 to 2750 cm^{-1} was omitted due to strong D_2O signals obscuring the spectra. (**C**) EPR spectra of the ACS variants. EPR samples were prepared with naturally abundant ^{12}CO (—) in comparison with isotopically labeled ^{13}CO (---). Quantified spin percentages are listed on the right as NA%/^{13}CO%. The ^{13}C splitting is most prominent at g = 2.028. Less intense broadening can be seen at 2.08 for WT and F229W, and at 2.062, 2.057, and 2.024 for the F229A variant.

However, even at protein concentrations as high as 2 mM, 4-fold higher than that used for wild-type protein, the F229A variant was devoid of any obvious FTIR signal in the IR range from 1980 to 2150 cm^{-1} (Figure 3.4). To ensure that the relative inactivity of the F229A variant was not due to global protein misfolding, we compared the full-spectra FTIR analysis of the three variants (Figure 3.3, (B)). The overall similarity of the amide and C-H regions at 1250 to 1750 cm^{-1} and 2800 to 3000 cm^{-1} indicates that the F229 substitution did not noticeably affect the overall fold of ACS.

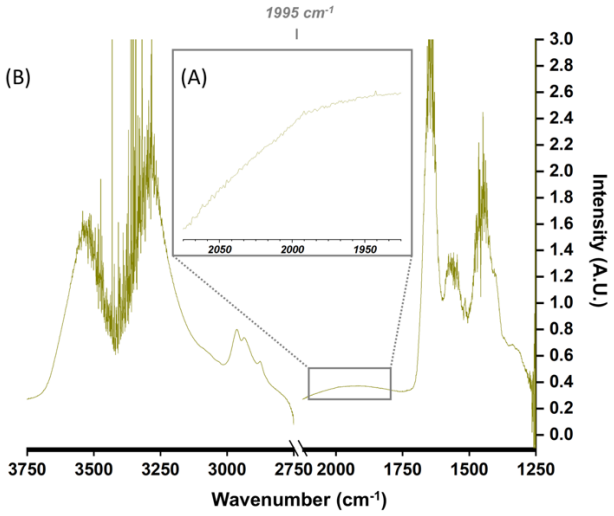

Figure 3.4 FTIR spectrum of CO-reacted F229A at the higher concentration of 2.3 mM. (A) The region of the Ni-CO stretching frequency, showing no obvious characteristic Ni-CO at 1995 cm^{-1}. (B) The full IR spectrum of the 2.28 mM F229A. Despite the relatively high concentration, there was no characteristic Ni-CO peak at 1995 cm^{-1} observed for the F229A variant.

When the F229W variant of ACS reacts with CO, a paramagnetic intermediate called the NiFeC species was observed by electron paramagnetic resonance (EPR) spectroscopy (Figure 3.3, (C)). Its intensity and *g*-values (at 2.074 and 2.028) were characteristic of the wild-type protein[19,33]. In agreement with the markedly altered kinetic and FTIR spectroscopic properties described above, the CO-incubated F229A variant showed only 20% intensity of the wild-type and F229W and a marked shift in the *g*-values to 2.062, 2.046, and 2.028 (Figure 3.3, (C) *bottom*), resembling a minority species sometimes observed in wild-type ACS[28]. Based on a detailed study by electron nuclear double resonance (ENDOR), the EPR spectrum of F229A can be deconvoluted into three components including a Ni(I) species that lacks CO[34]. The NiFeC signals of F229A, like that of wild-type and F229W, form during mixing (ca. 30 sec) and do not increase with incubation time for up to one hour. By performing the EPR experiment with ^{13}CO, line broadening was observed for all variants, unambiguously demonstrating that CO binds to their A-clusters, as shown for the wild-type protein (Figure 3.3, (C) *dotted lines*)[19,20].

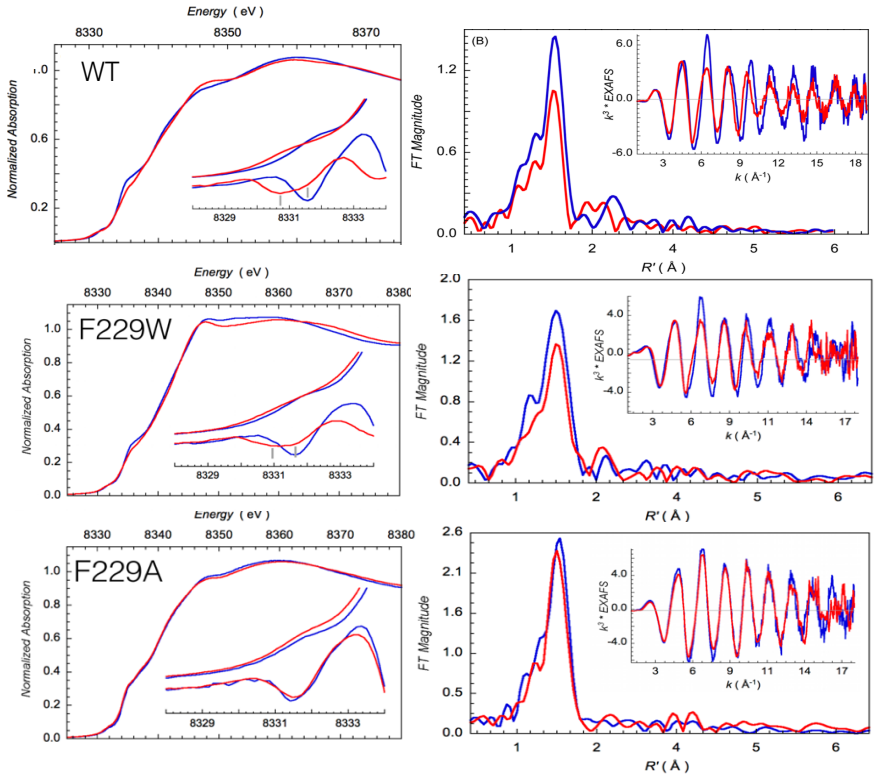

Figure 3.5 Ni K-edge XAS data showing pre-edge changes and EXAFS. (*Left half*) Ni K-edge absorption spectra of CO-exposed (red) and CO-unexposed (blue) reduced ACS. Insets show shifts in the Ni pre-edge of CO-exposed ACS relative to unexposed, where the first derivative shows distinct shifts corresponding to one of the two A-cluster Ni. Ni K-edge data for F229A does not show a pre-edge change seen in the WT and F229W. Consistent with the changes are the EXAFS (*Right half*), which show little to no changes for CO-exposed F229A relative to unexposed. WT data sourced from Can, 2017[26]. Data and figures provided by Dr. Ritimukta Sarangi.

In an effort to understand how mutation of a second-sphere aromatic residue near Ni_p could so thoroughly disrupt formation of the organometallic Ni_p-CO bond, we performed high resolution (out to a *k* value of 18) XAS experiments to compare the pre-, near-, and extended regions of the Ni and Fe absorption edges for the three variants in the presence and absence of CO. Before exposure to CO, the wild type, F229W and F229A variants display nearly identical Ni-XAS spectra, strongly indicating that the structure of the A-cluster is unchanged by the F229 substitutions (Figure 3.5, *left*). Addition of CO to the F229W variant caused the same changes in the Ni K-edge (oxidation state) and in the pre-edge and EXAFS (coordination geometry and environment) spectra as seen for the wild-type protein (Figure 3.5). Thus, as observed for the EPR

studies, substitution of Trp at this wall of the proposed alcove seems to retain all features of Phe in the wild-type protein.

However, we observed no significant differences in the pre- and K-edge or in the EXAFS region between the reduced and CO-exposed F229A variant, strongly suggesting that F229, one of the residues of the alcove, is required for formation of the Ni-CO intermediate in acetyl-CoA synthesis by ACS (Figure 3.5, *bottom*). The lack of a Ni-pre-edge shift or changes in the -XAS or -EXAFS of the F229A variant on CO exposure is likely due to the averaged population of Ni states. The small NiFeC EPR signal (< 0.1 spin/mol protein) would translate to a < 5% total conversion of planar Ni_p(II) to tetrahedral Ni_p(I), while 95% of the sample would remain in the resting Ni(II) state.

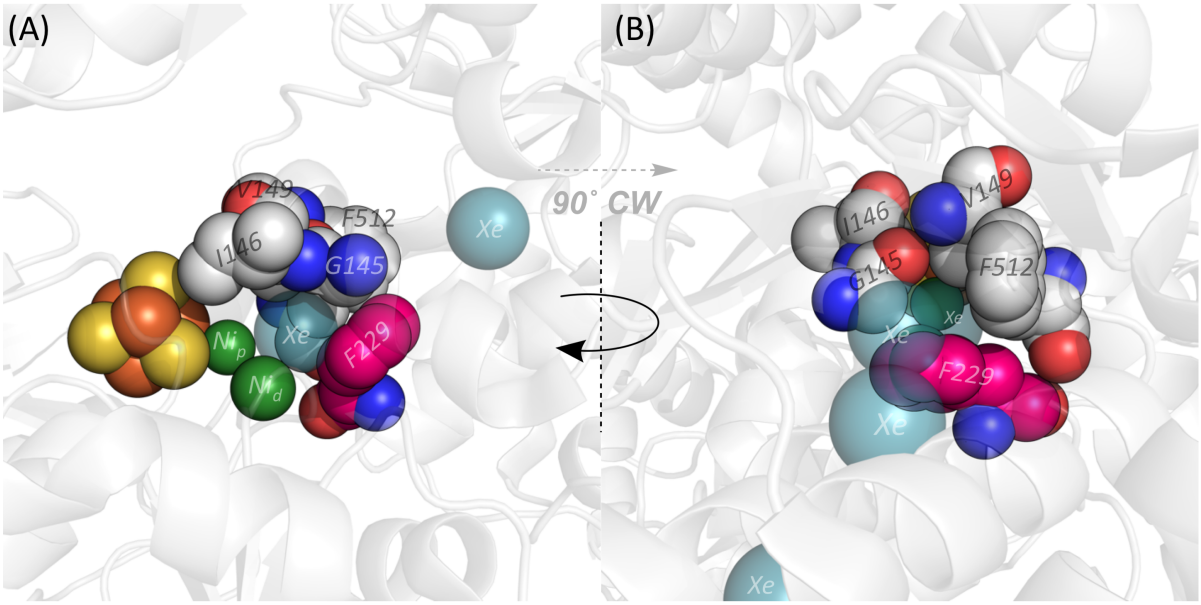

Figure 3.6 Model depicting the ACS alcove. High-pressure Xenon (teal spheres) crystal structure of ACS, highlighting the CO channel spanning from the CODH C-cluster (not shown) to the ACS A-cluster, with nearby residues as spheres. (**A**) Side-on perspective of the A-cluster, showing the alcove's role in maintaining CO near the proximal nickel, with F229 shown in magenta. (**B**) Down-channel perspective, 90˚ CW towards viewer (relative to (**A**)), showing how F229 and nearby residues form an opening for CO to reach the A-cluster. Stereoscopic versions of (**A**) and (**B**) may be found in the supplemental. PBD 2Z8Y.

The kinetic and spectroscopic results described here provide strong evidence that the alcove is required for productive CO binding. The X-ray crystallographic structure of CODH/ACS,

obtained under high-pressures of xenon, places F512, I146, V149 and F229 in a hydrophobic box surrounding a xenon atom near Ni_p in the A-cluster (Figure 3.6). The Xe atom has a center-to-center distance of ~ 3.5 Å from the Ni_p active site atom. The term "alcove" was first used to describe this structural feature when Bender, et al.[35] showed that low-temperature photolysis of CO-treated ACS converts the NiFeC species into a Ni_p(I) EPR state lacking the characteristic 1995 cm^{-1} Ni-C≡O IR signal. By studying the temperature-dependent rates of photolysis and rebinding, the activation energy barrier for CO rebinding to the A-cluster was calculated to be only 1 kJ/mol, leading to the hypothesis that the hydrophobic box near Ni_p forms an alcove that is integral in maintaining CO near the nickel active site.

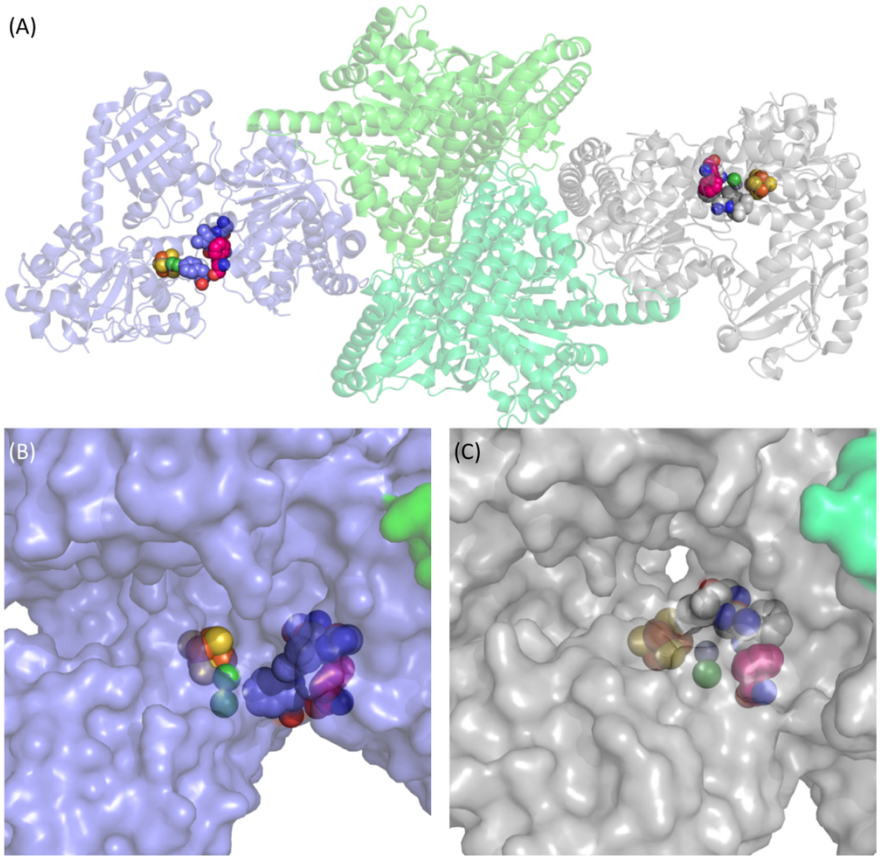

Figure 3.7 A-cluster changes associated with Open and Closed ACS. (A) Global view of the CODH/ACS heterotetramer, with both open (blue) and closed (grey) conformations of ACS, and the residues mentioned in this work modeled as spheres (CODH in shades of green). CODH/ACS crystal structure is different than the Xenon structure referenced previously. (B) Close-up surface model of the open (blue) conformation showing the exposed A-cluster primed for methylation, with F512 completely shifted from the closed conformation. (C) Close-up surface model of the closed (grey) conformation showing the open CO channel as seen **in Figure 3.6.** PDB 1OAO.

The role of F229 and the alcove may be to increase the local CO concentration near the A-cluster to facilitate CO binding. This implies that the inherent affinity of Ni_p for CO is rather low, resulting in loss of CO from the reaction. This would be devastating for the CODH/ACS complex, which catalyzes the -540 mV reduction of CO_2 to CO, and should lead to inability of acetogens to grow autotrophically. The F229 residue may also play an important role in facilitating formation of the tetrahedral Ni_p state, characteristic of the Ni_p(I)-CO state[26]. Crystallographic data[12,36] have demonstrated that ACS exhibits an open conformation poised for binding the CFeSP and a closed conformation that facilitates CO transport through the channel connecting the C-cluster of CODH to the A-cluster of ACS (Figure 3.7). Besides stabilizing the Ni-CO bond, it appears that F229 is linked to this structural transition between the open and closed states of ACS, provoking the question: is F229 (or the alcove) required for ACS methylation?

3.4.2 F229 is not required for methylation of ACS

Methylation and carbonylation of ACS occur by a random mechanism, with strictly ordered binding of CoA[10]. As shown in Figure 3.1, the mechanism of methyl transfer to ACS occurs by the nucleophilic reaction of Ni(I) with methyl-Co(III) to generate methyl-Ni(III) and Co(I). Recent spectroscopic studies revealed the methylated ACS product as a methyl-Ni bond (in preparation). We performed our experiments with methyl-cobinamide instead of the methylated CFeSP, because methyl-cobinamide is an effective, but slow methyl donor to ACS, with a reaction rate 100-fold slower than with the methylated CFeSP[37]. On the other hand, ACS reacts 1700-fold faster with methyl-cobinamide, which like the CFeSP lacks the coordinating benzimidazole group of methylcobalamin[38], suggesting the importance of this feature in methylation of ACS. On the other hand, the Fe_4S_4 cluster on the CFeSP is not required for methyl transfer, but is involved in reductive reactivation of the CFeSP[39].

Table 3.3 Spectroscopic and Kinetic Values Associated with ACS Variant Carbonylation and ¤Methylation.

	WT	F229W	F229A
IR Intensity (A.U.)	0.014; 100%	0.008; 83%	Absent; 0%
NA-NiFeC Spin (%)	29.7%	49.1%	12.5%
^{13}CO-NiFeC Spin (%)	56.0%	31.1%	6.1%
^{14}C-Exchange (μmol_{AcCoA} min^{-1} mg^{-1})	2.1 (± 0.5)	1.7 (± 0.3)	1.0 (± 0.2)
Methylation at 390 nm			
k_{obs} (s^{-1})	0.0464 (± 0.0006)	0.180 (± 0.002)	0.124 (± 0.001)
Relaxation Factor, β	0.575 (± 0.005)	0.573 (± 0.004)	0.533 (± 0.005)
Max Conversion Percent*	84.5 (± 0.2)%	71 (± 1)%	74.4 (± 0.6)%
Methylation at 470 nm			
k_{obs} (s^{-1})	0.0781 (± 0.0009)	0.164 (± 0.002)	0.105 (± 0.002)
Relaxation Factor, β	0.783 (± 0.009)	0.709 (± 0.008)	0.72 (± 0.01)
Max Conversion Percent◊	57.8 (± 0.6)%	60 (± 2)%	74 (± 2)%

¤Equation for the stretched exponential fits are $y = c + Ae^{(-(kt)^\beta)}$, where $0 < \beta \leq 1$.
**◊Max conversion percent calculated amount of Co(I)binamide formed from MeCo(III)binamide and their associated extinction coefficients. At 390 nm, $\varepsilon_{390,MeCbi} = 8\ mM^{-1}\ cm^{-1}$ and $\varepsilon_{390,Co(I)bi} = 25\ mM^{-1}\ cm^{-1}$: $\Delta\varepsilon_{470} = 17\ mM^{-1}$. At 470 nm, $\varepsilon_{470,MeCbi} = 11\ mM^{-1}\ cm^{-1}$ and $\varepsilon_{470,Co(I)bi} = 3\ mM^{-1}\ cm^{-1}$: $\Delta\varepsilon_{470} = 8\ mM^{-1}$*

The methylation activity of the F229A variant was compared to those of wild-type and F229W ACS by observing UV-Visible changes associated with the reaction of methyl-Cob(III)inamide (MeCbi), with a distinct absorption peak at 470 nm, to Cob(I)inamide, which has a maximum absorption at 390 nm (Figure 3.2, (B)). All three variants underwent methylation to similar extents and with similar rates, indicating that the alcove does not play a major role in methylation of ACS (Table 3.3). The extent of methylation varied between wavelengths, with maximal methylation percentages at 390 nm of 85, 71, and 74% and of 58, 60, and 74% at 470 nm for wildtype, F229W, and F229A (Table 3.3), with 470 nm having less spectral overlap from the ACS background and residual Ti(III) citrate. However, the observed rates of methylation measured

at both 470 nm (methyl-Cob(III) decay) and 390 nm (Cob(I) formation) show F229A is at no disadvantage for methylation, with observed rate constants for WT, F229W, and F229A of 0.046 s^{-1}, 0.180 s^{-1}, and 0.123 s^{-1} at 390 nm, and 0.078 s^{-1}, 0.164 s^{-1}, and 0.105 s^{-1} at 470 nm, respectively (Figure 3.2, (B); Table 3.3). The methylation data are best fit by a stretched exponential, which includes a "relaxation" factor, β, allowing a distribution of rate constants. This is in line with recent EM studies (Cohen, et al., in revision) showing significant conformational flexibility in ACS among limiting open and closed states, with only the open conformation able to undergo methylation (Figure 3.7). The ability of F229A to methylate at capacities similar to the wildtype and F229W variant implies the role of the F229 residue is predominantly steric, creating a local high-pressure CO environment and increasing the effective CO concentration at the ACS A-cluster.

3.4.3 F229A is unable to grow on $CO/H_2/CO_2$

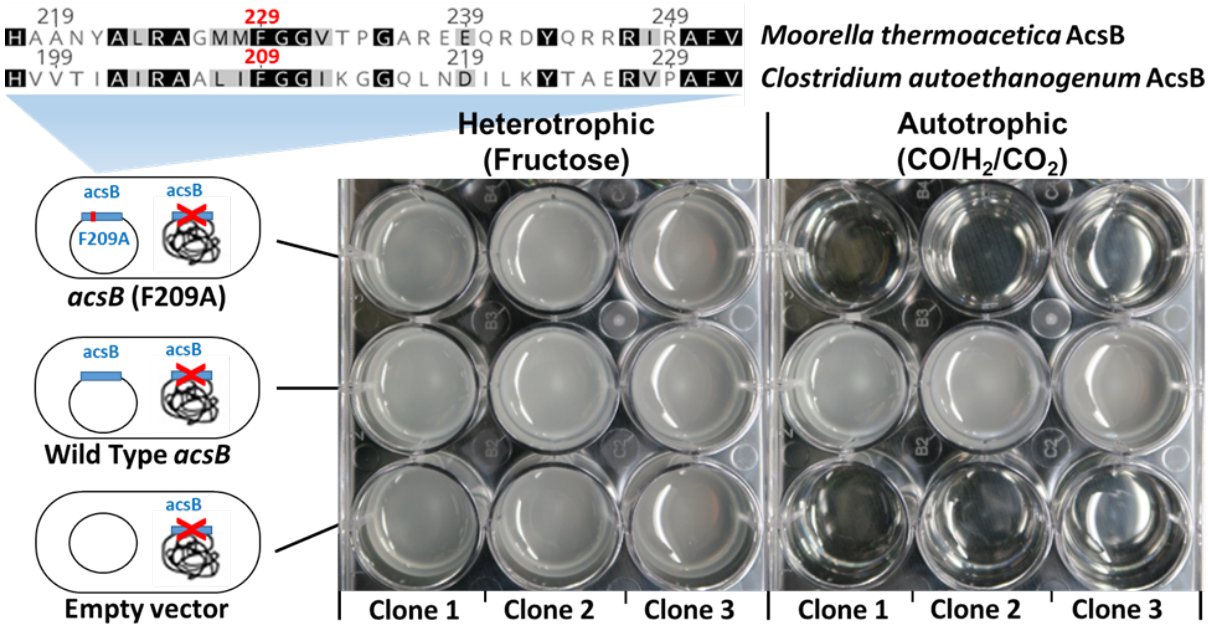

Figure 3.8 *In vivo* effect of F229A on autotrophic growth. (*top*) Alignment of AcsB showing highly conserved region around AA position 229 in *Moorella thermoacetica* and corresponding position 209 in *Clostridium autoethanogenum* (*bottom*) Complementation of *C. autoethanogenum ΔacsB*. Only wild type wild-type *acsB* but not *acsB*(F209A) is able to restore growth under $CO/H_2/CO_2$ autotrophic conditions. Data, figures, and images provided by Alex Mueller, Robert Nogle, Dr. Séan Simpnson, and Dr. Michael Köpke at Lanzatech (Skokie, IL).

To test the *in vivo* effects of the F229A substitution in the ACS enzyme, we chose *Clostridium autoethanogenum* as the host, due to the robust genetic tools available for this acetogen and previous demonstration that the ACS can be successfully knocked-out[4,16]. We pursued the corresponding substitution in the *C. autoethanogenum* enzyme, rather than the *M. thermoacetica* enzyme, since the ACS requires interaction with several other proteins to support function *in vivo*. The *C. autoethanogenum* enzyme shares 43% AA identity with the *Moorella AcsB* and lacks the first 20 AA and, but the region around the F229 position of the *M. thermoacetica* enzyme is highly conserved (as also found in other acetogens) and was identified to correspond to the F209 of the *C. autoethanogenum* enzyme (Fig 3.8, *top*; Table 3.2). We deleted the native genomic *acsB* using CRISPR-Cas9[15], and complemented the resulting strain, *C. autoethanogenum* Δ*acsB*, with plasmids to express *acsB* (F209A), in addition to wild type *acsB* and an empty plasmid as controls. The Δ*acsB* strains carrying plasmids were tested, in biological triplicate, for their ability to grow heterotrophically on fructose and autotrophically on a blend of CO, CO_2, and H_2. All three strains were able to grow heterotrophically, but in the absence of wild type *acsB*, strains did not grow autotrophically (Figure 3.8). While the wild-type *acsB* was able to complement the genomic deletion in autotrophic growth, the F209A variant was not able to rescue the knock-out. These results indicate that the CO alcove comprising phenylalanine in the ACS is critical to supporting autotrophic growth.

3.5 Conclusions

The results shown in this work reveal the significance of a CO alcove near the ACS A-cluster involved facilitating CO binding to the A-cluster Ni_p and its subsequent incorporation into acetyl-CoA. Multiple spectroscopic methods including EPR, infrared, and XAS showed significant shifts in CO binding for the alcove-disrupted F229A variant relative to the wildtype, but left methylation unaltered. While the IR and XAS data of F229A did not show any indication of CO binding to the A-cluster, EPR data showed distinct isotopic shifts in the characteristic NiFeC *g*-values when exposed to ^{13}CO, where a CO-dependent signal was identified via recent ENDOR experiments[34]. *In vivo*, an incomplete alcove translated to a large impact in autotrophic carbon fixation, preventing cellular growth on $CO/H_2/CO_2$ while leaving heterotrophic growth on fructose unaffected. The alcove's role in CO binding is hypothesized to act as a local high CO concentration for the A-cluster in order to drive the reaction towards acetyl production, and further enhancement

of the alcove's function in generating acetyl-CoA could offer more efficient means to produce custom renewable biofuels and industrial precursor chemicals from autotrophic CO_2 growth.

3.6 References for Chapter 3

(1) Rabiu, K. O.; Han, L.; Bhusan Das, D.; Abraham, M. A. In *Encyclopedia of Sustainable Technologies*; Elsevier: Oxford, 2017.

(2) Metz, B.; Davidson, O.; de Coninck, H.; Loos, M.; Meyer, L. IPCC special report on carbon dioxide capture and storage. **2005**.

(3) Cueto-Rojas, H. F.; van Maris, A. J. A.; Wahl, S. A.; Heijnen, J. J. Thermodynamics-based design of microbial cell factories for anaerobic product formation. *Trends in Biotechnology* **2015,** *33* (9), 534.

(4) Köpke, M.; Simpson, S. D. Pollution to products: recycling of 'above ground' carbon by gas fermentation. *Current Opinion in Biotechnology* **2020,** *65*, 180.

(5) Adam, P. S.; Borrel, G.; Gribaldo, S. Evolutionary history of carbon monoxide dehydrogenase/acetyl-CoA synthase, one of the oldest enzymatic complexes. *Proceedings of the National Academy of Sciences* **2018,** *115* (6), E1166.

(6) Ragsdale, S. W.; Pierce, E. Acetogenesis and the Wood-Ljungdahl pathway of CO(2) fixation. *Biochimica et Biophysica Acta* **2008,** *1784* (12), 25.

(7) Weiss, M. C.; Preiner, M.; Xavier, J. C.; Zimorski, V.; Martin, W. F. The last universal common ancestor between ancient Earth chemistry and the onset of genetics. *PLOS Genetics* **2018,** *14* (8), e1007518.

(8) Seravalli, J.; Xiao, Y.; Gu, W.; Cramer, S. P.; Antholine, W. E.; Krymov, V.; Gerfen, G. J.; Ragsdale, S. W. Evidence That NiNi Acetyl-CoA Synthase Is Active and That the CuNi Enzyme Is Not. *Biochemistry* **2004,** *43* (13), 11.

(9) Seravalli, J.; Gu, W.; Tam, A.; Strauss, E.; Begley, T. P.; Cramer, S. P.; Ragsdale, S. W. Functional copper at the acetyl-CoA synthase active site. *Proceedings of the National Academy of Sciences* **2003,** *100* (7), 5.

(10) Seravalli, J.; Ragsdale, S. W. Pulse-Chase Studies of the Synthesis of Acetyl-CoA by Carbon Monoxide Dehydrogenase/Acetyl-CoA Synthase: Evidence for a Random Mechanism of Methyl and Carbonyl Addition. *Journal of Biological Chemistry* **2007,** *283* (13), 10.

(11) Can, M.; Armstrong, F. A.; Ragsdale, S. W. Structure, Function, and Mechanism of the Nickel Metalloenzymes, CO Dehydrogenase, and Acetyl-CoA Synthase. *Chemical Reviews* **2014,** *114* (8), 25.

(12) Doukov, T. I.; Blasiak, L. C.; Seravalli, J.; Ragsdale, S. W.; Drennan, C. L. Xenon in and at the End of the Tunnel of Bifunctional Carbon Monoxide Dehydrogenase/Acetyl-CoA Synthase. *Biochemistry* **2008,** *47* (11), 9.

(13) Köpke, M.; Mihalcea, C.; Liew, F.; Tizard, J. H.; Ali, M. S.; Conolly, J. J.; Al-Sinawi, B.; Simpson, S. D. 2,3-Butanediol Production by Acetogenic Bacteria, an Alternative Route to Chemical Synthesis, Using Industrial Waste Gas. *Applied and Environmental Microbiology* **2011,** *77* (15), 5467.

(14) Heijstra, B. D.; Kern, E.; Koepke, M.; Segovia, S.; Liew, F., 2015.

(15) Nagaraju, S.; Davies, N. K.; Walker, D. J. F.; Köpke, M.; Simpson, S. D. Genome editing of *Clostridium autoethanogenum* using CRISPR/Cas9. *Biotechnology for Biofuels* **2016,** *9* (1), 219.

(16) Liew, F.; Henstra, A. M.; Winzer, K.; Köpke, M.; Simpson, S. D.; Minton, N. P. Insights into CO_2 Fixation Pathway of *Clostridium autoethanogenum* by Targeted Mutagenesis. *mBio* **2016,** *7* (3), e00427.

(17) Elliott, J. I.; Brewer, J. M. The inactivation of yeast enolase by 2,3-butanedione. *Archives of Biochemistry and Biophysics* **1978,** *190* (1), 351.

(18) Burton, R.; Can, M.; Esckilsen, D.; Wiley, S.; Ragsdale, S. W.; Armstrong, F. In *Methods in Enzymology*; Academic Press, 2018; Vol. 613.

(19) Ragsdale, S. W.; Ljungdahl, L. G.; DerVartanian, D. V. ^{13}C and ^{61}Ni isotope substitutions confirm the presence of a nickel(III)-carbon species in acetogenic CO dehydrogenases. *Biochemical and Biophysical Research Communications* **1983,** *115* (2), 7.

(20) Ragsdale, S. W.; Wood, H. G.; Antholine, W. E. Evidence that an iron-nickel-carbon complex is formed by reaction of CO with the CO dehydrogenase from *Clostridium thermoaceticum*. *Proceedings of the National Academy of Sciences* **1985,** *82* (20), 6811.

(21) Ragsdale, S. W.; Kumar, M. Nickel-Containing Carbon Monoxide Dehydrogenase/Acetyl-CoA Synthase. *Chemical Reviews* **1996,** *96* (7), 25.

(22) Fee, J. A. In *Methods in Enzymology*; Academic Press, 1978; Vol. 49.
(23) Raybuck, S. A.; Bastian, N. R.; Orme-Johnson, W. H.; Walsh, C. T. Kinetic characterization of the carbon monoxide-acetyl-CoA (carbonyl group) exchange activity of the acetyl-CoA synthesizing carbon monoxide dehydrogenase from *Clostridium thermoaceticum*. *Biochemistry* **1988,** *27* (20), 4.
(24) Grahame, D. A. In *Methods in enzymology*; Elsevier, 2011; Vol. 494.
(25) Seefeldt, L. C.; Ensign, S. A. A Continuous, Spectrophotometric Activity Assay for Nitrogenase Using the Reductant Titanium(III) Citrate. *Analytical Biochemistry* **1994,** *221* (2), 379.
(26) Can, M.; Giles, L. J.; Ragsdale, S. W.; Sarangi, R. X-ray Absorption Spectroscopy Reveals an Organometallic Ni–C Bond in the CO-Treated Form of Acetyl-CoA Synthase. *Biochemistry* **2017,** *56* (9), 12.
(27) Wedemeyer-Exl, C.; Darbre, T.; Keese, R. Preparation of Dicyano- and Methylcobinamide from Vitamin B12a. *Synthesis-stuttgart* **2008,** *2008*, 3429.
(28) Ragsdale, S. W.; Wood, H. G. Acetate Biosynthesis by Acetogenic Bacteria: Evidence that Carbon Monoxide Dehydrogenase is the Condensing Enzyme that Catalyzes the Final Steps of the Synthesis. *The Journal of Biological Chemistry* **1985,** *260* (7), 7.
(29) Hu, S. I.; Drake, H. L.; Wood, H. G. Synthesis of acetyl coenzyme A from carbon monoxide, methyltetrahydrofolate, and coenzyme A by enzymes from *Clostridium thermoaceticum*. *Journal of Bacteriology* **1982,** *149* (2), 440.
(30) Kumar, M.; Ragsdale, S. W. Characterization of the carbon monoxide binding site of carbon monoxide dehydrogenase from *Clostridium thermoaceticum* by infrared spectroscopy. *Journal of the American Chemical Society* **1992,** *114* (22), 8713.
(31) George, S. J.; Seravalli, J.; Ragsdale, S. W. EPR and Infrared Spectroscopic Evidence That a Kinetically Competent Paramagnetic Intermediate is Formed When Acetyl-Coenzyme A Synthase Reacts with CO. *Journal of the American Chemical Society* **2005,** *127* (39), 1.
(32) Seravalli, J.; Kumar, M.; Ragsdale, S. W. Rapid Kinetic Studies of Acetyl-CoA Synthesis: Evidence Supporting the Catalytic Intermediacy of a Paramagnetic NiFeC Species in the Autotrophic Wood−Ljungdahl Pathway. *Biochemistry* **2002,** *41* (6), 1807.
(33) Ragsdale, S. W.; Ljungdahl, L. G.; DerVartanian, D. V. EPR evidence for nickel-substrate interaction in carbon monoxide dehydrogenase from *Clostridium thermoaceticum*. *Biochemical and Biophysical Research Communications* **1982,** *108* (2), 5.
(34) James, C. D.; Wiley, S.; Ragsdale, S. W.; Hoffman, B. M. ^{13}C Electron Nuclear Double Resonance Spectroscopy Shows Acetyl-CoA Synthase Binds Two Substrate CO in Multiple Binding Modes and Reveals the Importance of a CO-Binding 'Alcove'. *bioRxiv* **2020**, 2020.06.23.165407.
(35) Bender, G.; Stitch, T. A.; Yan, L.; Britt, R. D.; Cramer, S. P.; Ragsdale, S. W. Infrared and EPR Spectroscopic Characterization of a Ni(I) Species Formed by Photolysis of a Catalytically Competent Ni(I)-CO Intermediate in the Acetyl-CoA Synthase Reaction. *Biochemistry* **2010,** *49* (35), 7.
(36) Darnault, C.; Volbeda, A.; Kim, E. J.; Legrand, P.; Vernède, X.; Lindahl, P. A.; Fontecilla-Camps, J. C. Ni-Zn-[Fe4-S4] and Ni-Ni-[Fe4-S4] clusters in closed and open α subunits of acetyl-CoA synthase/carbon monoxide dehydrogenase. *Nature Structural Biology* **2003,** *10*, 271.
(37) Seravalli, J.; Brown, K. L.; Ragsdale, S. W. Acetyl Coenzyme A Synthesis from Unnatural Methylated Corrinoids: Requirement for "Base-Off" Coordination at Cobalt. *Journal of the American Chemical Society* **2001,** *123* (8), 1786.
(38) Seravalli, J.; Zhao, S.; Ragsdale, S. W. Mechanism of Transfer of the Methyl Group from (6S)-Methyltetrahydrofolate to the Corrinoid/Iron−Sulfur Protein Catalyzed by the Methyltransferase from *Clostridium thermoaceticum*: A Key Step in the Wood−Ljungdahl Pathway of Acetyl-CoA Synthesis. *Biochemistry* **1999,** *38* (18), 5728.
(39) Menon, S.; Ragsdale, S. W. Role of the [4Fe-4S] Cluster in Reductive Activation of the Cobalt Center of the Corrinoid Iron−Sulfur Protein from *Clostridium thermoaceticum* during Acetate Biosynthesis. *Biochemistry* **1998,** *37* (16), 5689.

Chapter 4
Conclusions, Gaps, and Future Directions

4.1 Conclusions

The complicated nature of the ACS A-cluster has proven challenging in pinning down the exact nature of the substrate-bound intermediate states. In this work we have provided definitive evidence supporting the proposed intermediacy of organometallic methyl-nickel and acetyl-nickel bonds during anaerobic CO_2 fixation by the Wood-Ljungdahl pathway. We also have observed the methylated state of ACS as an EPR-silent diamagnetic Me-Ni_p(II) state. We demonstrated an ACS residue, F229, is part of a hydrophobic CO alcove required for CO binding to the Ni center in ACS and for anaerobic CO_2 fixation by the Wood Ljungdahl pathway. Finally, we showed that F229, and likely the alcove itself, does not play a role in methylation of ACS.

4.1.1 State of the Methylated ACS

The spectroscopic data presented in Chapter 2 revealed limited changes in the A-cluster while in the methylated state and strongly support formation of a Ni-C bond. While the data presented support a diamagnetic Ni(II)-methyl species with no redox contribution from the [Fe_4S_4], these findings does not exclude rapid redox changes that occur on either the Ni or the [Fe_4S_4] during the methylation reaction. For example, upon methylation, a catalytic Me-Ni(III) intermediate in equilibrium with an off-pathway Me-Ni(II) could be generated, or perhaps the [Fe_4S_4] could oxidize to an [Fe_4S_4](III) and re-reduce to [Fe_4S_4](II) with excess reductant. In conjunction with ENDOR and Mössbauer studies, our conclusions maintain that while there is an EPR-silent, diamagnetic Ni-C remains consistent with both of the established paramagnetic and diamagnetic mechanisms, UV-visible data showing a Cob(I) product indicates an S_N2-type mechanism, which would generate a corresponding Me-Ni(III), and supports the paramagnetic mechanism as the more likely of the two (Figure 4.1). Further support for the paramagnetic mechanism was seen when the reductant concentration was reduced to substoichiometric levels.

The substoichiometic UV-visible methylation data exhibited an absorbance jump at 390 nm with rapid decay to a Cob(II)inamide, indicating a powerful oxidant is generated during the methylation reaction, the identity of which could arise from a Ni(III)[1].

In contrast to the complicated observed changes *in vitro*, the methylation reaction *in vivo* is unlikely to be inundated with excess low-potential reductants like the Ti(III) citrate present in this work. With the current understanding of the methylation reaction, ACS *in vivo* is likely to be activated by an external redox activator such as ferredoxin, but leaves the A-cluster EPR-silent as seen in this work[2], until Me-CFeSP transfers its methyl group to the activated ACS, generating both the Co(I)FeSP and Me-Ni(III)-ACS[3]. After methyl transfer, Me-Ni(III)-ACS is reduced by an unidentified electron-donor to Me-Ni(II)-ACS and Co(I)FeSP remains in its reduced state[3]. The *in vivo* source of electron for ACS could come from various sources, such as the A-cluster $[Fe_4S_4]$(II), CODH when in the CODH/ACS complex, or even from a different ferredoxin. The most likely *in vivo* candidate for a rapid reduction would be the internal $[Fe_4S_4]$(II) donor due to its proximity to the methylation site, but the prevalence of $[Fe_4S_4]$ found in partner proteins and the electronically-coupled nature of the A-cluster has proven difficult for definitive spectroscopic identification of any catalytically-relevant $[Fe_4S_4]$(I) or $[Fe_4S_4]$(III) for ACS.

While we favor the rapidly-decaying paramagnetic Me-Ni_p(III) intermediate outlined in Figure 4.1, a radical mechanism with homolytic cleavage of the methyl group offers an additional explanation for the formation of the Cob(II)inamide. Instead of an S_N2 methyl transfer, the methyl group may transfer radically from Me-Cob(III)inamide to the activated ACS, producing both the Co(II)binamide and Me-Ni(II), although previous studies on CODH/ACS methyl transfer have not supported homolytic cleavage, favoring the S_N2 mechanism of methyl transfer mentioned previously[3,4].

Mass spectrometry data presented in Chapter 2 also supports methylation at the A-cluster Ni_p, as there are no obvious trends in methylation or acetylation on the ACS cysteines despite UV-visible observation of ACS methylation with MeCbi and subsequent acetylation by CO treatment. While not the initial focus of the experiments, the triplicate mass spectrometry data revealed a broad number of methylated and acetylated cysteine residues in the as-isolated, methylated, and acetylated states. The broad cysteine methylation does not account for the observed UV-visible changes, and in relation to the untreated sample, the ACS cysteines are discredited as the primary location of methylation. The small differences seen in the methylation profile for C67 and

acetylation profile for C509 are unlikely to play important mechanistic roles, since C67 is distant to the A-cluster, and C509 acetylation appears independent of C509 methylation. The methylation and acetylation on the A-cluster cysteines contacting the Ni_p, C509, C528, and C597, may arise from a very small subpopulation of nickel-deficient ACS, since without the nickel-replete A-cluster methylation at the residual unstructured cysteines may be possible and could account for the low baseline level of cysteine methylation.

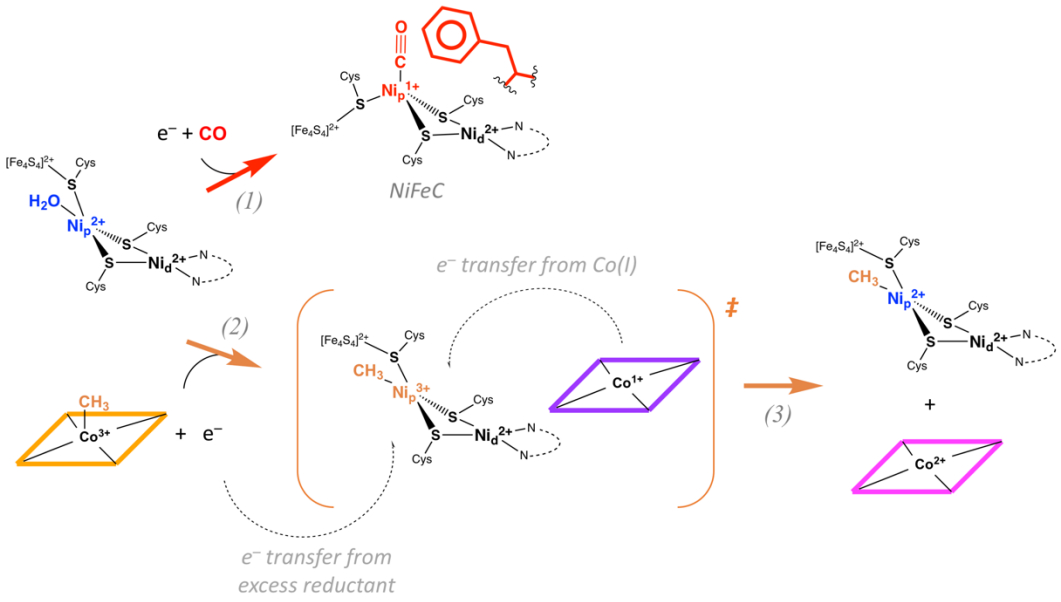

Figure 4.1 Proposed ACS mechanism based on findings within this work. When resting state ACS is reduced with low-potential reductants ("e⁻") and (*1*) exposed to CO, it produces the catalytically competent and characteristic NiFeC with significant participation by nearby F229 residue forming the CO alcove. When the resting state ACS is reduced with low-potential reductants ("e⁻") and (*2*) reacted with Me-Cob(III)inamide, it forms a highly oxidizing Me-Ni(III) species that is rapidly reduced to (*3*) reform the diamagnetic A-cluster.

4.1.2 The Alcove's Role in CO-bound ACS

The data presented in Chapter 3 unambiguously show the importance of the hydrophobic alcove in facilitating the wildtype NiFeC EPR signal at the A-cluster, while leaving ACS competent for methylation. Despite FTIR experiments indicating no CO was bound to the F229A variant, isotopically labeled CO proved the presence of a Ni-CO bond via EPR. With EPR and ENDOR confirmation, the F229A did bind CO (~10%), but to much less capacity with no geometric changes occurring at the Ni as observed in the wildtype. While we know the alcove-deficient ACS cannot bind CO as completely as the WT, the physical reason why the hydrophobic

alcove poises the A-cluster to bind CO is not yet well understood. The significant *in vivo* effects of alcove disruption were a surprising revelation of how finely-tuned the ACS A-cluster is for autotrophic growth, with the complete lack of viable growth of *Clostridium autoethanogenum* on $CO_2/CO/H_2$.

Recent CODH/ACS Cryo-EM data from the Drennan lab (Cohen, *et al.* in revision) have shown much more conformational flexibility for ACS than previously thought and may reflect a more flexible geometric environment present within A-cluster. These large conformational changes could influence the distinct square planar and tetrahedral Ni_p geometries associated with the methylated and carbonylated states of ACS and affect the electronic character of the A-cluster, poising it for catalysis. Taking the recent Cryo-EM data with the F229A EPR spectrum (*g*-values of 2.06, 2.05, and 2.02), previous CODH/ACS EPR experiments have shown the same EPR spectrum under the following conditions – CoA treatment[5-7], protease treatment[8], and detergent[8,9]. It is important to note that this work has identified F229 as the source of the altered-NiFeC, shedding light on the underlying effect this hydrophobic residue has on the catalytically relevant NiFeC.

Recent ENDOR data on the CO-bound ACS and alcove variants have shown two very interesting results on the nature of CO bound to the A-cluster[10]. In direct conflict with the FTIR data depicting a single CO stretch at 1995 cm^{-1}, the ENDOR data shows the wildtype ACS having two COs bound to its A-cluster (Figure 4.2, (a)) revealed by mapping the ^{13}C ENDOR signal over the entire characteristic ACS NiFeC[10]. The two CO-bound nickel is seen even with stoichiometric addition of CO, implying the ACS NiFeC itself reflects a 2 CO-bound species. While these results are significant, ENDOR data is acquired at very low temperatures of 2K, and might bind two CO as a low-temperature artifact not be seen at temperatures for IR. Additionally, ENDOR also revealed the F229A variant has two CO binding modes, consisting of both the "wildtype" mode and an "A" mode unique to F229A (Figure 4.2, (b)), as well as a CO-independent paramagnetic signal[10].

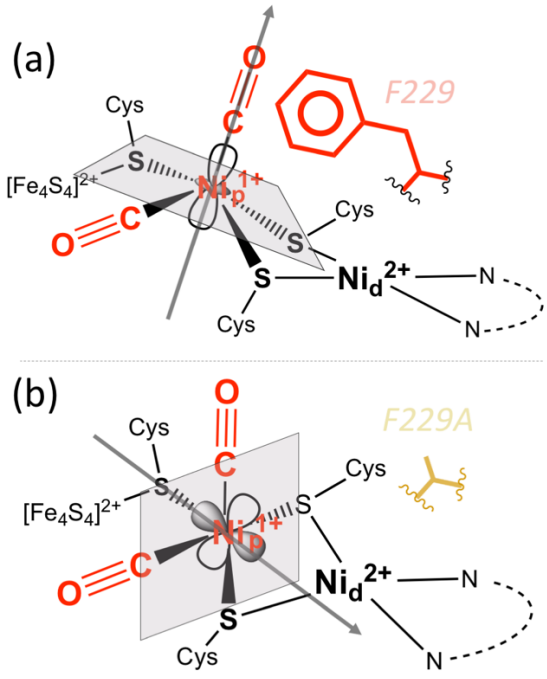

Figure 4.2 CO-binding modes at the ACS A-cluster seen by ENDOR Spectroscopy. Lack of an alcove causes the CO-binding plane to reorient. (a) The CO-binding mode of the wildtype ACS as determined by ENDOR spectroscopy. One CO binds along the d_z^2 axis is shown in parallel to the arrow, whereas the other binds "out-of-plane" in the d_x^2-$_y^2$ plane. (b) The unique CO-binding mode of the F229A variant as determined by ENDOR spectroscopy. Both COs bind "in-plane" along the xy-plane, with the z-axis represented by the arrow. Figure adapted from James, 2020[10].

These data together indicate the alcove facilitates a specific square pyramidal geometry seen in the wildtype A-cluster, forcing the CO into a particular binding position poising it for acetyl condensation upon methylation. In the alcove-deplete F229A, the less sterically constrained A-cluster may offer additional space for different CO binding modes, or perhaps it may reflect an intermediate NiFeC signal that is functionally relevant between conformational transitions not observed in the alcove-replete enzyme. Assuming the ENDOR data are an accurate reflection of the catalytically active ACS NiFeC, then the ACS mechanism cannot be truly random as previously proposed[11,12], since the 2 CO-bound A-cluster would slow the rate of methylation ACS.

4.2 Known Gaps

Many gaps exist in the understanding of the ACS mechanism, and the experiments presented in this work naturally raise more questions than they answer, and as such we have listed

some gaps in our understanding of how ACS binds its substrates. The gaps mentioned below represent a list of the most glaring holes in our understanding of ACS, but by no means are they limited to the following.

4.2.1 Gaps in the Understanding of the Methylated State of ACS

While much of this work has examined the states of substrate-bound ACS, much still needs to be discovered regarding how the states are reached and stabilized. The EPR silence of the A-cluster after methylation has proven tricky to study, but the possibility of a short-lived EPR-active intermediate constitutes a significant gap in the understanding of ACS. Despite the well-studied methylation by Me-Co(III)FeSP and observation of the 2-electron transfer producing the Co(I)FeSP and methylated ACS, the proposed paramagnetic Me-Ni(III) species has remained elusive[4,11]. Rapid freeze quench EPR experiments have shown no paramagnetic Ni(III) species in ACS, and while these studies were conducted using CODH/ACS, they did not observe any indication of a paramagnetic methyl intermediate, supporting the EPR-silent $Ni_p(0)$ to Me-$Ni_p(II)$ mechanism[13,14]. All of the aforementioned studies have only investigated ACS within the CODH/ACS complex, and the experiments performed in this work did not focus on any short-lived Me-$Ni_p(III)$ or $[Fe_4S_4](I/III)$ intermediate states produced within 5 minutes of the methylation reaction. The rapid formation and decay at ~400 nm when ACS is methylated with limited titanium citrate (0.5x) is of additional interest, considering a decrease in absorbance ~420 nm is typical in $[Fe_4S_4]$ reduction[15]. The proximity of the $[Fe_4S_4]$ to the two nickels in the A-cluster may have an effect on the specific wavelength observed during reduction but requires further experimental evidence to resolve its exact nature.

4.2.2 Implication of ACS Cysteine Modifications

We are interested in understanding the significance of the methyl- and acetyl-cysteine modifications and their impact to the ACS mechanism, considering mass spectrometry data indicated a reproducible background amount of cysteine modification is present on most, if not all of the 10 cysteines in ACS. Although data in this work does not support any cysteine as a significant catalytic location of methylation or acetylation, whether these modifications are seen at the same level in the natively-grown ACS or CODH/ACS from *M. thermoaceticum* are of

interest since catalytic cysteine methylation has been proposed previously[14,16], and *E. coli* may alter cysteines in a differential capacity to the native organism.

4.2.3 Implications of F229 in the CO Alcove

We are interested in understanding why the typical NiFeC observed in the CO-bound wildtype ACS changes so significantly in an alcove-deficient ACS, and why the same g = 2.06, 2.05, and 2.02 EPR spectrum has been observed in disruptive proteolytic and gel separation conditions in previous studies[6-9]. Some questions stand out in particular regarding the function of the alcove in ACS: Can the alcove's efficiency be improved? Does the alcove provide local high concentration of CO to the A-cluster, and can we bind more CO to F229A with higher CO concentrations? Does the F229A NiFeC represent a non-functioning subpopulation state, or does it hold some structural relevance to the CO-bound Ni_p intermediate within the A-cluster? What is the identity of the CO-independent signal seen in F229A via ENDOR experiments, and does it represent a reduced A-cluster? These questions arose as the significance of the alcove emerged and stand as the obvious direction for studying carbonylation of ACS in the future.

4.2.4 Gaps in the Understanding of the Carbonylated State of ACS

The gaps in our knowledge regarding ACS carbonylation are less extensive than with methylation but remain just as important in understanding the mechanism as a whole. While carbonylation is known to produce a Ni-C bond at the A-cluster, exactly in what capacity and to what extent is still not well known at this time. As observed in Tan, 2002, CO became inhibitory at higher concentrations (≥ 100 μM CO) and was proposed to form a 2 CO-bound A-cluster ACS[11,17]. This inhibitory 2 CO-bound A-cluster mirrors the data observed via ENDOR, but the dependence of the NiFeC on both COs reflects a significant gap in our understanding the role and place of this species in the ACS mechanism. We want to know if the 2 CO-bound ACS species, truly reflects an inhibited form of ACS as previously proposed[11], and assuming ACS does bind two COs to the A-cluster Ni_p, can we find the other CO stretch signal via FTIR? We are also interested in knowing if the 2 CO-bound to ACS is a catalytically relevant species and whether it is reflected in the CODH/ACS complex, or only seen in ACS alone.

4.2.5 Further Gaps

While there are still gaps in understanding methylation and carbonylation in ACS, the nature of acetyl group formation is equally as important in understanding how the substrates bind, how the A-cluster facilitates the combination of the methyl and carbonyl substrates to form the acetyl group, and how the A-cluster transfers the acetyl group to its subsequent CoA cofactor[18]. Like the reduced ACS state, the acetylated ACS has never been observed via EPR and is likely diamagnetic[18], and recent XAS data mentioned in Chapter 2 has confirmed an acetyl-Ni intermediate in the A-cluster. Based on steady-state experiments, ACS does not need any external reductant to condense the methyl and carbonyl substrates as well as the transfer of the acetyl group from the A-cluster to CoA[6,12,19]. While this work touched only on a few acetylated-ACS samples in contrast to the methyl-ACS, we are still very interested in gaining a deeper understanding of what poises the A-cluster for acetyl condensation and transfer to CoA.

4.3 Future Directions

4.3.1 Future Methylation Experiments

While numerous experiments are necessary to fully understand how the methylated CFeSP transfers its methyl group to ACS, some key experiments can bridge the emergent gaps described above in understanding the state of the methylated A-cluster. In order to provide additional evidence of a Ni-C bond, the gamma-induced radiolysis below 77K, or cryoreduction, of methylated ACS has been planned in an attempt to generate an unnatural Me-Ni(I) from the hypothesized Me-Ni(II) to unequivocally confirm the methylated A-cluster organometallic bond[20]. Rapid Freeze Quench (RFQ) EPR of reductant-limited ACS could reveal or refute the existence of short-lived paramagnetic species resulting from A-cluster methylation. More comprehensive mass spectrometry studies should be performed to include concentration titrations with methyl-cobinamide and limiting titanium citrate reductant to observe any correlation in cysteine methylation, as well as a CO titration against methylated ACS to determine how relevant the cysteine methylation is in producing the acetylated intermediate.

In an attempt to mirror the alcove studies for methylation, we have targeted other residues in the secondary coordination sphere surrounding the A-cluster that are thought to play a role during methylation; F512 and I146. These residues will be targeted for site-specific replacement

and their respective alanine variants are anticipated to affect the ability of ACS to methylate but leave carbonylation unaffected.

A long-term experimental direction is to use methylation-coupled electrochemistry as well as photo-inducible quantum dot reductants with mediator dyes to produce the methylated ACS intermediate for EPR, eliminating the necessary and broadly-contaminating titanium citrate reductant used in this work[21]. The use of photoinducible reductants allows for greater control of the methylation reaction and subsequent EPR, as the sample can be photoactivated to a specific concentration of reducing equivalents *in situ*, where emergent unique EPR spectra can be correlated.

4.3.2 Future Alcove Experiments

Based on the data in Chapter 3, it is necessary to determine exactly what the alcove's role is in binding CO, and whether it involves facilitating a local high-pressure CO zone for the A-cluster. If the F229 residue acts as a critical wall for the alcove and allows for a locally high CO concentration, then titrating the F229A variant with increasing CO concentrations should lead to an increase in the F229A NiFeC intensity observed via EPR. Longer-term, we are hoping to produce other alcove-disrupting mutations also targeting F512 or I146 in order to determine if these site-specific substitutions would replicate the CO binding deficiencies seen in F229A, or if they enhance or disrupt methylation. We are also planning ENDOR experiments to determine the exact nuclear location of the paramagnet for the CO-independent portion of the F229A EPR signal, considering the typical NiFeC is largely delocalized over the entire A-cluster. Since the paramagnetic signal in F229A has been seen previously, this unique EPR signal may be the "reduced" ACS EPR signal, a signal not stable in the wildtype ACS for unknown reasons.

4.3.3 Future Experiments into the Carbonylated State of ACS

In light of the recent ENDOR findings[10], we are significantly interested in resolving why the wildtype ACS binds two COs at the Ni_p in the A-cluster. Previous studies have shown[22] the catalytic competence of the NiFeC and the characteristic IR band at 1995 cm^{-1} and that they appear in parallel, but the recent evidence of two CO conflicts with the understanding that only one CO binds to the A-cluster. Stoichiometric ACS-CO ENDOR experiments at a lower concentration of CO closer to the K_M for ACS-CO (~100-300 μM CO)[17] have recently replicated the results seen

in the solution-saturated ~1 mM CO[10]. Since ENDOR has affirmed this doubly-bound A-cluster at a lower CO concentration, the search for the other Ni-C IR signal has begun. Assuming the two CO-bound A-cluster is not a low-temperature artifact, it is a surprising notion that one of two nearly identical terminal Ni-CO signals would be spectroscopically absent via FTIR. In any case, the two CO-bound A-cluster would require additional high resolution infrared techniques such as 2D-IR, since previous high resolution stopped-flow infrared has indicated only one Ni-CO peak[22]. Any future infrared experiments performed are planned to be under more rigorous conditions, controlling for various CO pressures and assessing other solvents in order to reduce any Ni-CO stretch signal quenched by H_2O or D_2O.

4.3.4 Additional Future Experiments of Interest

While the following experiments may be outside of the direct research scope presented in this work, there are a number of future directions in studying the ACS mechanism of carbon-carbon bond formation.

A series of comprehensive experiments investigating near-IR changes associated with the methylated and carbonylated states of ACS may reveal rapid electronic changes at the A-cluster via charge transfer transitions when exposed to the carbonyl and methyl substrates[23]. Near-IR experiments have proven useful in elucidating the numerous redox states of another nickel-containing enzyme, methyl-CoM reductase, and are expected to provide crucial insight for the A-cluster changes upon substrate binding at the metal centers.

The open and closed conformational flexibility of ACS observed via crystallographic and Cryo-EM could indicate the importance of the F229 residue in directing CO to the A-cluster after methylation by CFeSP. Considering the alcove plays a surprising role in forming the characteristic NiFeC, we hypothesize the large changes in the ACS conformation may lead to small, but significant geometric changes within the A-cluster[24,25]. Since coenzyme A (CoA) is the final step in the ACS mechanism and likely to interact directly with the A-cluster and cause some conformational shifts upon binding, high concentrations of CoA might conformationally "lock" ACS into a certain A-cluster geometry[6,12]. A locked A-cluster geometry could have significant impacts on the ability of ACS to bind its substrates or participate in redox reactions, and experiments probing the conformational effects of CoA binding are in the preliminary stages.

4.4 Perspectives

The evidence presented in this work affirms ACS is a crucial component of the broader global carbon cycle, and elucidating its complex mechanism and chemistry is gaining in importance as the atmospheric carbon dioxide concentration continues to exponentially increase. While much remains to be understood regarding the ACS mechanism, altogether the evidence put forth in this work shows the complicated relationship of the A-cluster to carbon-carbon bond formation and catabolism. Every study that expands the understanding of how ACS is able to perform its reaction furthers the potential for adaptation to inorganic models and mimics in order to productively convert waste carbon such as CO and CO_2 into economically-relevant chemical precursors for industrial use[26]. The ability of ACS to perform such a difficult chemical reaction at ambient temperature and pressure is quite remarkable, and the unique $[Fe_4S_4]$-Ni_p-Ni_d architecture does not alone account for the reactivity of the A-cluster, as many inorganic models and artificial metalloenzymes require much lower potentials, secondary sphere interactions, and specific geometries to be catalytically productive[18,27-29].

Despite the numerous questions that arise from this work, they will be resolved in time, as ACS is only one of the numerous complex catalytic centers in biology that compose anaerobic carbon fixation. The key to understanding the ACS mechanism depends on interdisciplinary collaborative work focusing on other metalloenzymatic mechanisms, bio-inspired model complex chemistry, and bioinorganic spectroscopy.

4.5 References for Chapter 4

(1) Thauer, R. K. Biochemistry of methanogenesis: a tribute to Marjory Stephenson:1998 Marjory Stephenson Prize Lecture. **1998,** *144* (9), 2377.

(2) Bender, G.; Ragsdale, S. W. Evidence That Ferredoxin Interfaces with an Internal Redox Shuttle in Acetyl-CoA Synthase during Reductive Activation and Catalysis. *Biochemistry* **2011,** *50* (2), 276.

(3) Menon, S.; Ragsdale, S. W. Role of the [4Fe-4S] Cluster in Reductive Activation of the Cobalt Center of the Corrinoid Iron−Sulfur Protein from *Clostridium thermoaceticum* during Acetate Biosynthesis. *Biochemistry* **1998,** *37* (16), 5689.

(4) Seravalli, J.; Brown, K. L.; Ragsdale, S. W. Acetyl Coenzyme A Synthesis from Unnatural Methylated Corrinoids: Requirement for "Base-Off" Coordination at Cobalt. *Journal of the American Chemical Society* **2001,** *123* (8), 1786.

(5) Ragsdale, S. W.; Ljungdahl, L. G.; DerVartanian, D. V. ^{13}C and ^{61}Ni isotope substitutions confirm the presence of a nickel(III)-carbon species in acetogenic CO dehydrogenases. *Biochemical and Biophysical Research Communications* **1983,** *115* (2), 7.

(6) Ragsdale, S. W.; Wood, H. G. Acetate Biosynthesis by Acetogenic Bacteria: Evidence that Carbon Monoxide Dehydrogenase is the Condensing Enzyme that Catalyzes the Final Steps of the Synthesis. *The Journal of Biological Chemistry* **1985,** *260* (7), 7.

(7) Ragsdale, S. W.; Wood, H. G.; Antholine, W. E. Evidence that an iron-nickel-carbon complex is formed by reaction of CO with the CO dehydrogenase from *Clostridium thermoaceticum*. *Proceedings of the National Academy of Sciences* **1985,** *82* (20), 6811.
(8) Murakami, E.; Ragsdale, S. W. Evidence for Intersubunit Communication during Acetyl-CoA Cleavage by the Multienzyme CO Dehydrogenase/Acetyl-CoA Synthase Complex from *Methanosarcina thermophila*: EVIDENCE THAT THE β SUBUNIT CATALYZES C–C AND C–S BOND CLEAVAGE. *Journal of Biological Chemistry* **2000,** *275* (7), 4699.
(9) Xia, J.; Hu, Z.; Popescu, C. V.; Lindahl, P. A.; Münck, E. Mössbauer and EPR Study of the Ni-Activated α-Subunit of Carbon Monoxide Dehydrogenase from *Clostridium thermoaceticum. Journal of the American Chemical Society* **1997,** *119* (35), 8301.
(10) James, C. D.; Wiley, S.; Ragsdale, S. W.; Hoffman, B. M. ^{13}C Electron Nuclear Double Resonance Spectroscopy Shows Acetyl-CoA Synthase Binds Two Substrate CO in Multiple Binding Modes and Reveals the Importance of a CO-Binding 'Alcove'. *bioRxiv* **2020**, 2020.06.23.165407.
(11) Tan, X.; Sewell, C.; Lindahl, P. A. Stopped-Flow Kinetics of Methyl Group Transfer between the Corrinoid-Iron-Sulfur Protein and Acetyl-Coenzyme A Synthase from C*lostridium thermoaceticum*. *Journal of the American Chemical Society* **2002,** *124* (22), 7.
(12) Seravalli, J.; Ragsdale, S. W. Pulse-Chase Studies of the Synthesis of Acetyl-CoA by Carbon Monoxide Dehydrogenase/Acetyl-CoA Synthase: Evidence for a Random Mechanism of Methyl and Carbonyl Addition. *Journal of Biological Chemistry* **2007,** *283* (13), 10.
(13) Seravalli, J.; Kumar, M.; Ragsdale, S. W. Rapid Kinetic Studies of Acetyl-CoA Synthesis: Evidence Supporting the Catalytic Intermediacy of a Paramagnetic NiFeC Species in the Autotrophic Wood−Ljungdahl Pathway. *Biochemistry* **2002,** *41* (6), 1807.
(14) Lindahl, P. A. Acetyl-coenzyme A synthase: the case for a Ni_p0-based mechanism of catalysis. *Journal of Biological Inorganic Chemistry* **2004,** *9*, 8.
(15) Hoppe, A.; Pandelia, M.-E.; Gärtner, W.; Lubitz, W. [Fe4S4]- and [Fe3S4]-cluster formation in synthetic peptides. *Biochimica et Biophysica Acta (BBA) - Bioenergetics* **2011,** *1807* (11), 1414.
(16) Pezacka, E.; Wood, H. G. Acetyl-CoA pathway of autotrophic growth. Identification of the methyl-binding site of the CO dehydrogenase. *Journal of Biological Chemistry* **1988,** *263* (31), 16000.
(17) Tan, X.; Surovtsev, I. V.; Lindahl, P. A. Kinetics of CO Insertion and Acetyl Group Transfer Steps, and a Model of the Acetyl-CoA Synthase Catalytic Mechanism. *Journal of the American Chemical Society* **2006,** *128* (37), 12331.
(18) Can, M.; Armstrong, F. A.; Ragsdale, S. W. Structure, Function, and Mechanism of the Nickel Metalloenzymes, CO Dehydrogenase, and Acetyl-CoA Synthase. *Chemical Reviews* **2014,** *114* (8), 25.
(19) Kumar, M.; Lu, W. P.; Liu, L.; Ragsdale, S. W. Kinetic evidence that carbon monoxide dehydrogenase catalyzes the oxidation of carbon monoxide and the synthesis of acetyl-CoA at separate metal clusters. *Journal of the American Chemical Society* **1993,** *115* (24), 11646.
(20) Van Stappen, C.; Thorhallsson, A. T.; Decamps, L.; Bjornsson, R.; DeBeer, S. Resolving the structure of the E1 state of Mo nitrogenase through Mo and Fe K-edge EXAFS and QM/MM calculations. *Chemical Science* **2019,** *10* (42), 9807.
(21) Sanchez, M. L. K.; Wu, C.-H.; Adams, M. W. W.; Dyer, R. B. Optimizing electron transfer from CdSe QDs to hydrogenase for photocatalytic H_2 production. *Chemical Communications* **2019,** *55* (39), 5579.
(22) George, S. J.; Seravalli, J.; Ragsdale, S. W. EPR and Infrared Spectroscopic Evidence That a Kinetically Competent Paramagnetic Intermediate is Formed When Acetyl-Coenzyme A Synthase Reacts with CO. *Journal of the American Chemical Society* **2005,** *127* (39), 1.
(23) Schugar, H. J.; Krogh-Jespersen, K.; Potenza, J. A.; Lalancette, R. A. Charge-transfer spectra of model Cu(II) chromophores. *Inorganica Chimica Acta* **1983,** *79*, 50.
(24) Darnault, C.; Volbeda, A.; Kim, E. J.; Legrand, P.; Vernède, X.; Lindahl, P. A.; Fontecilla-Camps, J. C. Ni-Zn-[Fe4-S4] and Ni-Ni-[Fe4-S4] clusters in closed and open α subunits of acetyl-CoA synthase/carbon monoxide dehydrogenase. *Nature Structural Biology* **2003,** *10*, 271.
(25) Leguto, A. J.; Smith, M. A.; Morgada, M. N.; Zitare, U. A.; Murgida, D. H.; Lancaster, K. M.; Vila, A. J. Dramatic Electronic Perturbations of CuA Centers via Subtle Geometric Changes. *Journal of the American Chemical Society* **2019,** *141* (3), 1373.
(26) Liew, F.; Martin, M. E.; Tappel, R. C.; Heijstra, B. D.; Mihalcea, C.; Köpke, M. Gas Fermentation—A Flexible Platform for Commercial Scale Production of Low-Carbon-Fuels and Chemicals from Waste and Renewable Feedstocks. *Frontiers in Microbiology* **2016,** *7*, 694.

(27) Manesis, A. C.; Musselman, B. W.; Keegan, B. C.; Shearer, J.; Lehnert, N.; Shafaat, H. S. A Biochemical Nickel(I) State Supports Nucleophilic Alkyl Addition: A Roadmap for Methyl Reactivity in Acetyl Coenzyme A Synthase. *Inorganic Chemistry* **2019,** *58* (14), 8969.
(28) Manesis, A. C.; O'Connor, M. J.; Schneider, C. R.; Shafaat, H. S. Multielectron Chemistry within a Model Nickel Metalloprotein: Mechanistic Implications for Acetyl-CoA Synthase. *Journal of the American Chemical Society* **2017,** *139* (30), 10328.
(29) Harrop, T. C.; Mascharak, P. K. Structural and spectroscopic models of the A-cluster of acetyl coenzyme a synthase/carbon monoxide dehydrogenase: Nature's Monsanto acetic acid catalyst. *Coordination Chemistry Reviews* **2005,** *249* (24), 3007.